Chapter 4

Results and Discussion

This chapter focuses on the analysis of fabricated A572 gr. 50 and 316L SS welded joints under premixed shielding gas of Ar and CO_2 for variable current, weld speed and gas flow rate using Design of experiments. Taguchi's experimental design was used for optimization, and the effect of input variables were analyzed, followed by validation. The welded joints were analyzed through Minitab17 and ANOVA analysis to find the optimized parameters and their trends. The performance of joints were addressed in terms of macrostructure, microstructural features, and mechanical behaviour for maximum strength. Heat affected zone of joints were thoroughly analyzed for its contribution. Keeping these points in mind chapter has been divided into three sections, i.e.

I) Optimization, II) Microstructural analysis, III) Mechanical properties.

4. Results and Discussion

4.1 Optimization of Process Parameters for A572 gr. 50

Design of experiment (DOE) is a systematically structured and well organized method to conceptualize the relationship between various factors. The primary objective of the DOE technique includes minimization of the number of experiments (which makes it cost-effective) along with predicting the most influential parameters that need to be carefully examined while experimentation for desired output. It also predicts the optimum parameters and the response for the given output [145]. Taguchi's approach using Minitab 17 was utilized to predict the relationship between input and output variables. Through preliminary experiments, the levels of welding parameters for A572 gr. 50 steel have been finalized for full penetration welded joints. It was observed from preliminary results that lower current values caused low penetration for even the lowest weld speeds. It caused excessive piling of weld metal, causing greater transfer of heat to base material hence creating wider HAZ. If weld speeds were too high, then again lack of penetration and humping beads were observed, as shown in Figure 3.5 for both materials. Lower shielding gas below 6 l/min proved insufficient to protect the weld bead, causing severe oxidation and defects. So the range of experiments were chosen for defect-free joints for a smooth appearance and absence of any surface defects (like surface porosity, undercut etc.) with full penetration for most of the joint in a single pass.

Taguchi's robust design approach was used to generate the L_{16} orthogonal array for 3-factors and 4-levels has been chosen as shown in Tables 3.4 and 3.5. Input variable/factors and their corresponding levels according to L_{16} orthogonal array have been tabulated in Table 4.1. Joints were welded, and their Ultimate Tensile strength (UTS) and Yield stress (YS) were tabulated. Heat input values for Samples S01 to S16 prepared under different conditions have been calculated using Equation 4.1 (where HI=

Heat Input (kJ/cm), *V*= Welding voltage (Volts), *I*= Welding current (Ampere), *S*= Weld speed (mm/s) and μ= Welding efficiency. A welding efficiency of 0.84 for GMAW process has been used [146]. HI varied from a maximum of 25.54 kJ/mm (in sample no. 16) to a minimum of 3.11 kJ/cm (sample no. 04) which is well within the recommended HI to restore the impact properties [79].

$$\boldsymbol{Heat\ Input(HI)} = \mu \frac{V\ x\ I}{S\ x\ 100} (kJ/cm) \quad \text{… Equation 4.1}$$

Table 4.1: L_{16} orthogonal array and corresponding levels and obtained Ultimate Tensile strength (UTS), Yield Stress(YS) and heat inputs(HI)

Sample No. (Exp. No.)	**Current** (Amp)	**Gas flow rate** (l/min)	**Weld Speed** (mm/sec)	**Heat Input** (kJ/cm)	**Yield Stress** (MPa)	**Ultimate Tensile Strength** (MPa)
01	100	10	1.25	12.1	305	375
02	100	13	2.50	6.05	325	389
03	100	16	3.75	3.99	328	405
04	100	19	5.00	3.11	320	399
05	135	10	2.50	7.64	334	404
06	135	13	1.25	16.07	310	392
07	135	16	5.00	3.82	327	405
08	135	19	3.75	5.39	328	410
09	**170**	**10**	**3.75**	**6.63**	**350**	**435**
10	170	13	5.00	4.84	342	428
11	170	16	1.25	19.89	327	408
12	170	19	2.50	10.21	338	418
13	205	10	5.00	6.22	330	399
14	205	13	3.75	8.3	326	387
15	205	16	2.50	12.77	322	382
16	205	19	1.25	25.54	317	378

In the design of experiments, factor is an independent variable/attribute which affects or is suspected to affect the characteristic being analyzed. A factor may be variable and measurable (e.g. welding speed), or it may be an attribute whose presence or identity may be analyzed, like weld speed or type of shielding gas flow rate. Levels are the steps

or qualitative features of a factor to be analyzed through experimental design. If the factor is an attribute, each of its step is a level. Response is the numerical output/result of an observation with a given treatment like penetration, spatter quantity etc. Effect of a factor is the variation in response due to changes in levels of the factor. Main effect is the effect of a factor averaged over different levels of the other factor. Interaction effect is the respective change in effect of one factor when another factor is changed from one level to another.

4.1.1 Evaluation of Signal to Noise (S/N) Ratio

Taguchi method uses a statistical measure of performance called signal-to-noise ratio(S/N ratio). S/N ratio includes both the mean and the variability into account. The ratio of the mean (Signal) and the standard deviation (Noise) depends on the quality characteristics of the product/process to be optimized [147-148]. The standard S/N ratios are generally calculated using Equations 4.2, 4.3 and 4.4.

a) Taguchi's S/N Ratio for Nominal-the-best (NB): It's used for quality characteristics which are usually a nominal output, for example the atmospheric temperature, rainfall, gas flow rate etc. and calculated using the equation below

$$\eta = 10 \ln_{10} \frac{1}{n} \sum_{i=1}^{n} \frac{\mu^2}{\sigma^2} \quad \text{… Equation 4.2}$$

b) Taguchi's S/N Ratio for Smaller-the-better (SB): Quality characteristics for welding defects, pollution etc. and is calculated using the equation below

$$\eta = -10 \ln_{10} \frac{1}{n} \sum_{i=1}^{n} y_i^2 \quad \text{… Equation 4.3}$$

c) Taguchi's S/N Ratio for Larger-the-better (LB): Used for quality characteristics like purity, strength, toughness etc. and is calculated using the equation below

$$\eta = -10 \ln_{10} \frac{1}{n} \sum_{i=1}^{n} \frac{1}{y_i^2} \quad \text{… Equation 4.4}$$

Where η = S /N Ratio, y_i = Value of the quality characteristic at i^{th} setting, n = Total number of trial runs at i^{th} setting, μ= Mean, σ = Standard Deviation:

The optimal setting is the parameter combination, which has the highest S/N ratio [149-151]. Because irrespective of the quality criteria used S/N ratio should always be maximized. Once experimental data (quality attribute value) is normalized using the above criteria with normalized values, it lies between zero to one. Zero represents the worst quality to be rejected, and one represents the most satisfactory quality. Since the S/N ratio is expressed as mean (signal) to the noise (deviation from the target), maximizing S/N ratio ensures minimum deviation, and hence it is (S/N ratio) to be maximized. UTS, YS and Heat Input were chosen as response variables to evaluate the effect of various parameters. Therefore "Larger the better" for YS and UTS were selected for analysis. As minimum heat would impart lesser temperature and stresses, generating narrower HAZ. So the "Smaller the better" criteria was selected for Heat input.

After DOE experimentation using Minitab17 software and applying Taguchi's method, S/N ratio graph for UTS has been obtained and given in Figure 4.1.

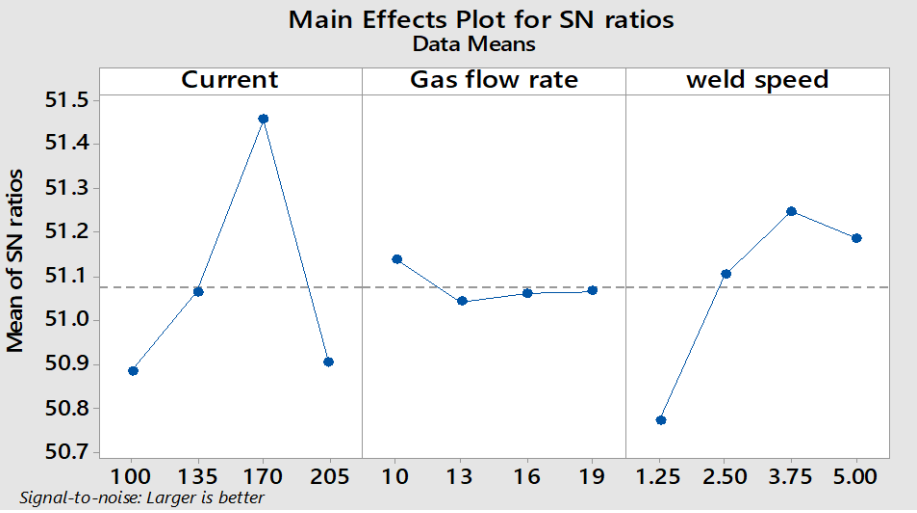

Figure 4.1: Main effect plot for S/N ratio

"Larger the better" criteria was selected to find the effects and contribution of UTS and YS for different levels of parameters. The response for Signal to Noise ratios,

along with the response for means, have been tabulated in Table 4.2. The higher the value S/N ratio better it would be and close to the optimum value. Current and weld speed have shown considerable variation with respect to gas flow rate, and so it needs to be controlled. S/N reached the peak for current: 170 A, weld speed: 3.75 mm/sec and gas flow rate of 10 l/min, which suggest the optimum parameters for maximum UTS and YS. The main effect plot as shown in Figure 4.3 and Table 4.2 were investigated to confirm the optimum welding parameters.

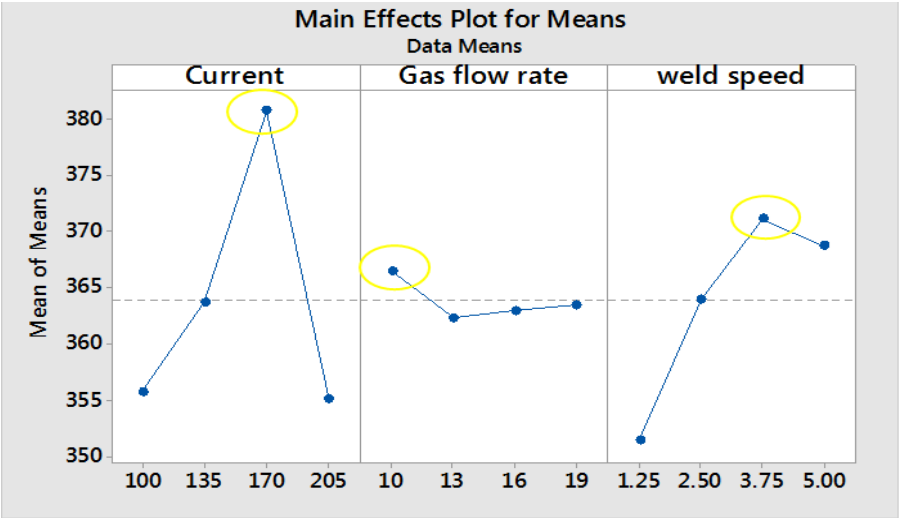

Figure 4.2: Main effect plot of means

The main effects plot for data means has been an indicator for finding the optimum parameter. From the graph in Figure 4.3, the optimum parameters for larger the better criteria were Current: 170 A, weld speed: 3.75 mm/sec and gas flow rate of 10 l/min encircled in yellow.

Through the analysis of UTS and YS results, it was concluded that current is the most influential parameter (Ranked 1), followed by weld speed (Ranked 2) and gas flow rate (Ranked 3). Strength increased with an increase in current and weld speed due to an increase in penetration and removal of impurities. Further increase in current caused serious grain coarsening, causing a decrease in strength further.

Table 4.2: Taguchi Analysis: UTS versus Current, gas flow rate, weld speed

Response for Signal to Noise Ratios "Larger is better"				Response for Means		
Level	Welding Current	Gas flow rate	Welding speed	Welding Current	Gas flow rate	Welding speed
1	50.88	51.14	50.77	357.3	361.8	349.8
2	51.06	51.04	51.1	360.1	355.5	366.9
3	51.46	51.06	51.25	378.9	363.9	364.5
4	50.90	51.06	51.19	345.5	360.6	360.6
Delta	0.57	0.10	0.48	33.4	8.4	17.1
Rank	1	3	2	1	3	2

Individual plots were also plotted using "Larger is better" criteria for UTS and YS, while "Smaller is better" was used and plotted for HI as shown in Figures 4.2, 4.3 and 4.4 respectively.

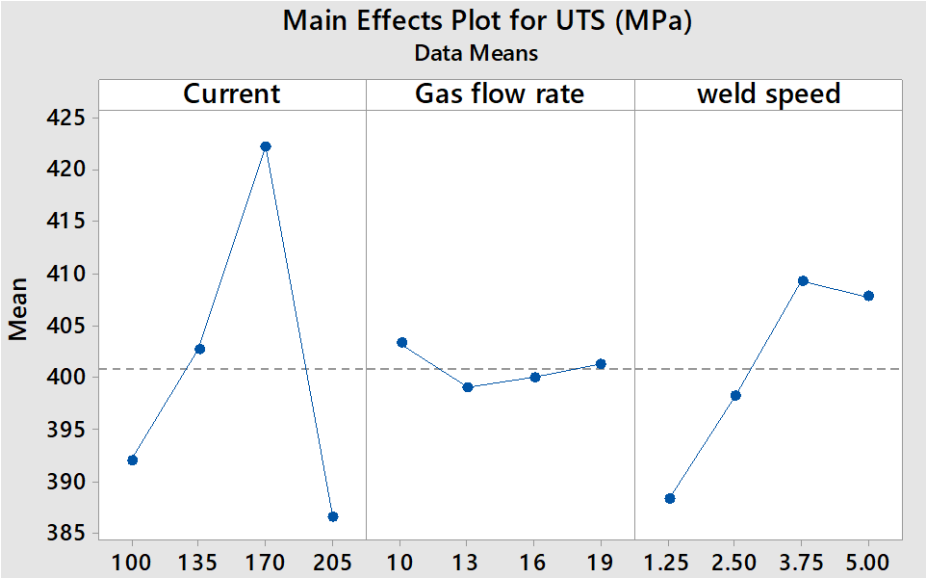

Figure 4.3: Taguchi Analysis: UTS (MPa) Vs Current (A), Gas flow rate (l/min) and weld speed (mm/sec)

More variation in Yield stress with respect to UTS due to the grain coarsening effect in HAZ was found, but the optimum parameters were the same for experimentation. Heat input increased linearly with current and gas flow rate. An increase in weld speed causes a decrease in heat input as HI is proportional to current and decreases with an increase in welding speed.

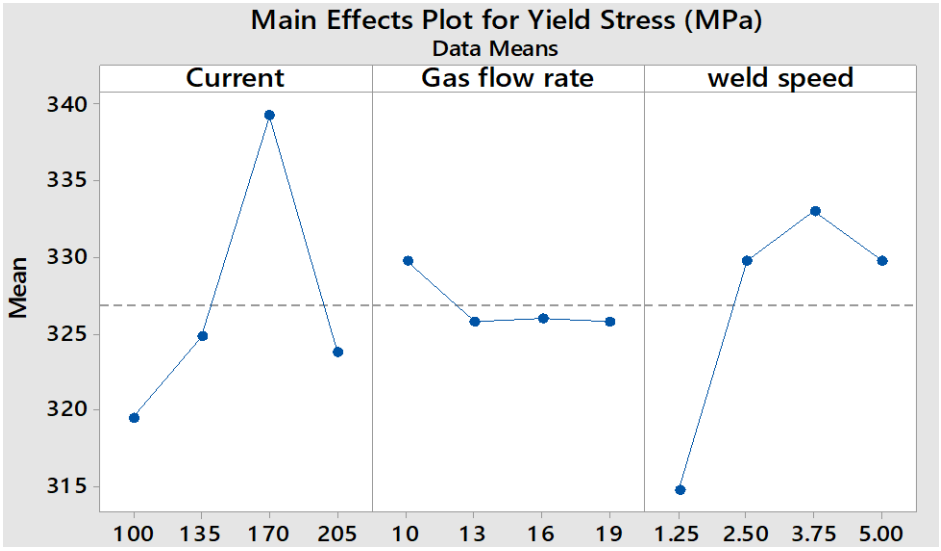

Figure 4.4: Taguchi Analysis: YS (MPa) Vs Current (A), Gas flow rate (l/min) and weld speed (mm/sec)

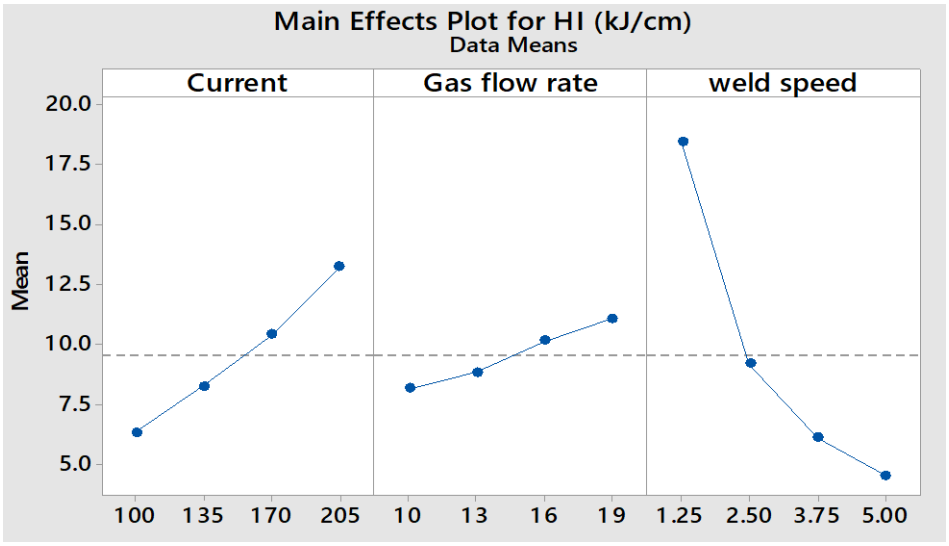

Figure 4.5: Taguchi Analysis: HI (kJ/cm) Vs Current (A), Gas flow rate (l/min) and weld speed (mm/sec)

4.1.2 Analysis of Variance (ANOVA)

The significance of input process parameters on the output quality characteristics is explored by the conduct of Analysis of Variance (ANOVA). The detailed ANOVA result for the output responses is shown in Table 4.3. After analyzing through ANOVA, it was observed that various parameters contributed in response variables. Current contributed the most Current (60.87%), followed by Weld speed (32.69%) and gas flow rate (1.43%). The optimum process parameter analyzed through the main effect plot as

shown in Figure 2(a) was 170 A current, 14 l/min gas flow rate and 1.25 mm/sec welding speed, i.e. sample no. S8. Taguchi's results can be verified through the microstructural changes and hardness patterns which will be discussed later.

Table 4.3: Analysis of Variance for means for UTS, using Adjusted SS for Tests

Source	DF	Seq SS	Adj SS	Adj MS	F	P	%age contribution
Current	3	1709.42	1709.42	569.81	24.27	0.001	60.87
Gas flow rate	3	320.99	320.99	106.6	0.57	0.655	11.43
Weld speed	3	917.92	917.92	305.97	13.03	0.005	22.69
Error	6	140.84	140.84	23.47			5.01
Total	15	2808.36					

The effect of input process parameters on the weld characteristics that influence the UTS, YS and HI has been investigated using interaction plots of the welded joint. The interaction plot shows the relationship among the parameters for each level. Based on the results, the interaction effect of the factors influencing weld tensile characteristics has been generated. The interaction effect of current, weld speed and gas flow rate on UTS, YS and HI have been shown in Figures 4.5, 4.6 and 4.7, respectively.

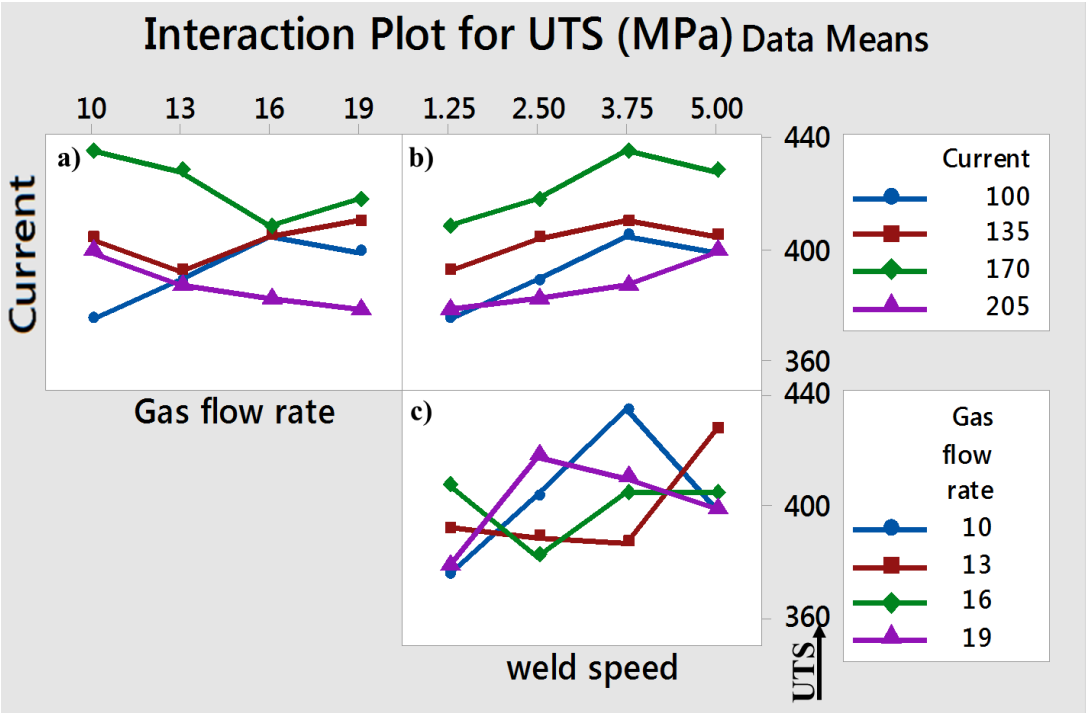

Figure 4.6: The interaction plot for ultimate tensile strength

From the interaction plot for Ultimate Tensile Strength, it can be observed that UTS Increased with current from 100 A to 170 A, followed by a decrease in strength due to excessive coarsening effect in CGHAZ. An increase in weld speed caused an increase in UTS, followed by the decrease of UTS as weld speed increases caused lower heat imparted to weld pool available for HAZ generation along with reduced peak temperature achieved. Downward variation in UTS was observed for the highest gas flow rate (19 l/min) due to excessive turbulence caused at higher gas flow rates.

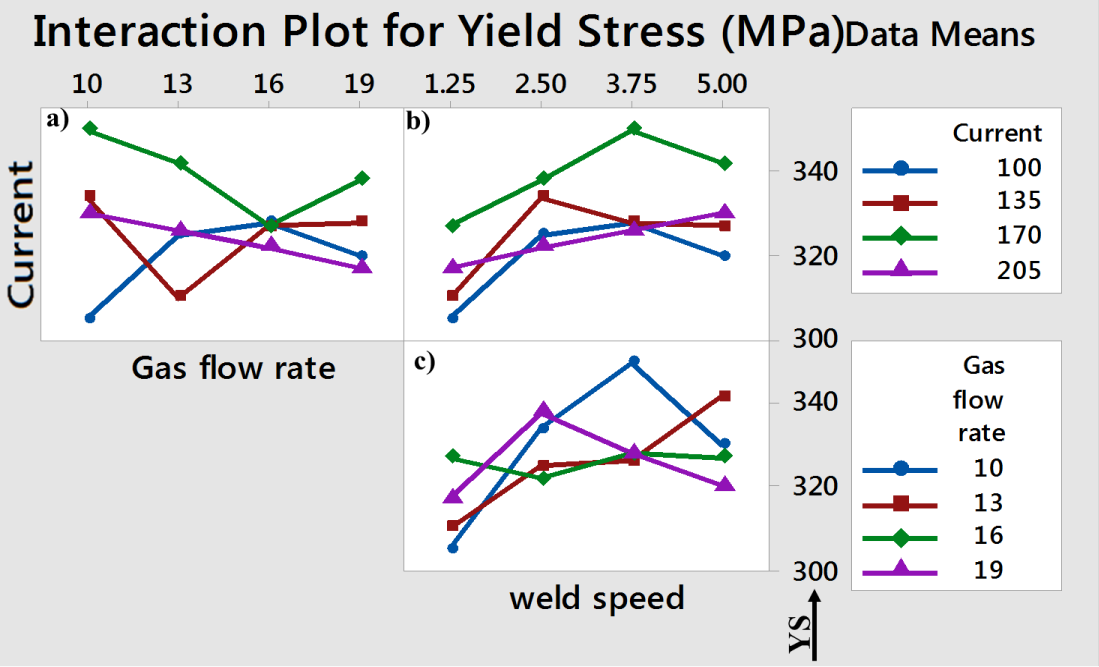

Figure 4.7: The interaction plot for Yield Stress

From the interaction plot for YS from Figure 4.7, it can be deduced that YS increased initially with increasing weld speed followed by a decrease due to lesser grain coarsening effect. A decrease in YS was also observed for an increase in gas flow rate. YS increased with weld speed for most of the gas flow rates and decreased for higher weld speed and current. From the interaction plot for Heat Input (Figure 4.8), it can be found that with an increase in weld speed, there is a decrease in heat input, and considerable variation in HI was observed due to current. For lower values of current with an increase in gas flow rate, there has been a decrease in heat input.

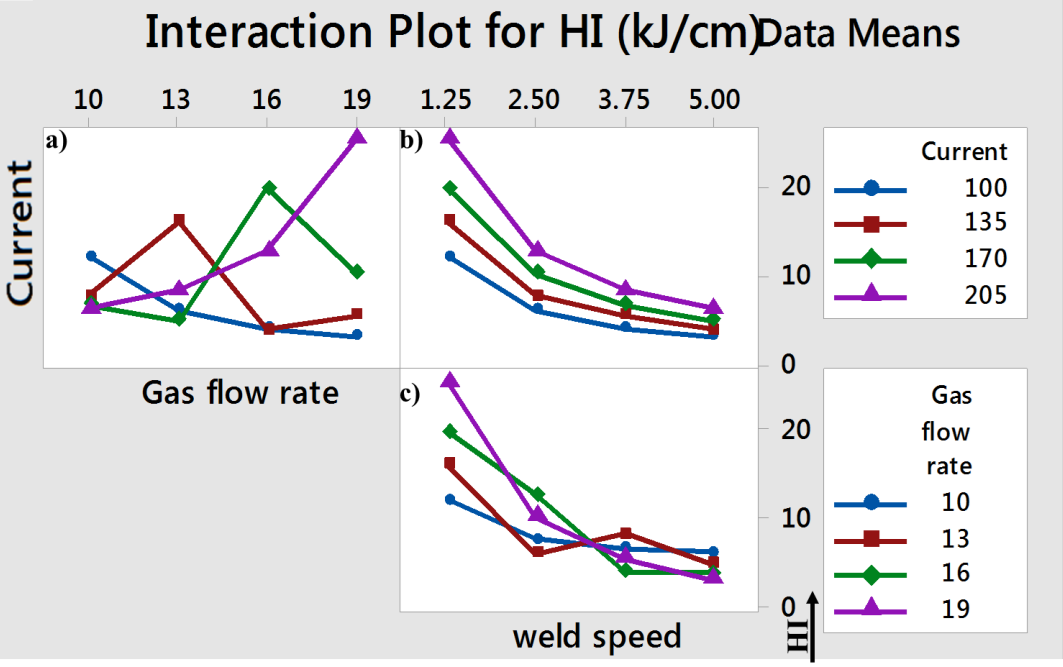

Figure 4.8: The interaction plot for Heat Input

4.2 Heat Input effect on Welded joint of A572 gr. 50

Heat input in welding plays an essential role in the formation of different phases/microstructures in WB, FZ and HAZ. The calculated HI for Samples S1 to S16 has been shown using the bar chart as shown in Figure 4.8. Calculated HI values varied from a maximum of 25.34 kJ/mm (sample no. 16) to a minimum of 3.11 kJ/mm (sample no. 04). It can be observed that current is the most influencing parameter with 53.6% contribution (from Taguchi analysis). It governs the total heat available for fusion and rejection to the adjacent parent metal. An increase in current causes an increase in electrode melting rate for higher heat input [152]. The HI has a major effect on the soft zone width in HAZ as well as it controls the maximum temperature attained, causing variable hardness in the WB and HAZ. Also, for sample no. 01, 06, 11 and 16 with high welding heat input (min.12 kJ/mm), due to constitutional supercoiling, there is sufficient time for grain growth in coarse grain heat affected zone (CGHAZ). High heat caused the disappearance of harder phases gradually with the formation of bainitic structure. An increment in width of HAZ can be easily observed for high HI from the micrograph of

HAZ as it forces slow cooling and microstructural change for a larger area in HAZ. When the welding heat input was around 6 kJ/s, the cooling time was low, and thus a fast cooling rate easily produced smaller grain size grains and harder phases in HAZ. Maximum Heat Input was 25.54 kJ/cm, which is within the permissible range to restore the toughness in the weld joint [153]. For sample no. 01 to 04 gas flow rate and weld speed increases which caused a reduction of heat into the weld pool and reduced the dilution, while for samples 13 to 16, the welding speed decreased while the gas flow rate increased.

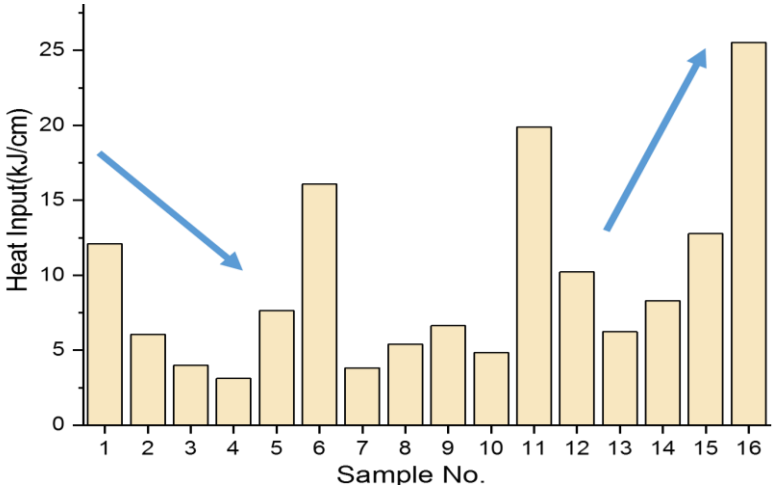

Figure 4.9: Heat Input effect and sample number

4.3 Macrostructural evaluations of A572 gr. 50

As welding consists of a moving heat source, each nital etched sample revealed a distinctly visible Weld Bead (WB), Heat Affected Zone (HAZ) and its different zones along the WB and moving away from it. The macrostructure and different views of all 16 samples have been tabulated in Table 4.3. Welding parameters for samples 01, 02, 05, 06, 08, 09, 11, 12, and 14 produced a perfect bead shape with full penetration. Spatter-free and perfect elliptical bead top ripples can be seen from the macrograph. Also, the width-to-depth ratio was not exceeding 1:2, which is required to avoid solidification cracking [154]. Most of the samples showed no surface defects except for samples having high welding speed and low current levels like sample no. 04, 07, 10 and 13. High HI produced

wider bead at low and intermediate speeds, while lower speeds showed excessive piling of filler wire for samples 15 and 16. For sample no. 02, 05, 08, 09, 11, 12, 14, the appearance of bead shown spatter free surface with a luxurious appearance, indicating fully protected bead on either side of weld also providing the benefit of no further finishing requirement for the weld. Weld joints produced with HI around 6 to 10kJ/cm like 02, 05, 09 and 14 showed excellent appearance with full penetration, and adequate dilution without any spatters (good bead protection), indicating no need for further processing. Sample no. 09, welded at optimum parameters, has the reinforcement of 1.2 mm and lower HAZ.

Table 4.4: Macro graph of all A572 gr. 50 samples

Sample No.	**Heat Input** (kJ/cm)	**Weld Bead View**	**Macro Structure**
1	12.1		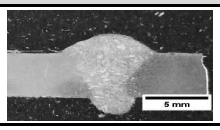
2	6.05		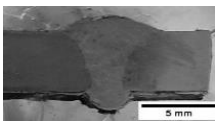
3	3.99		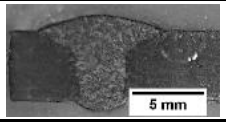
4	3.11		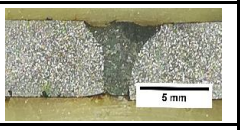
5	7.64		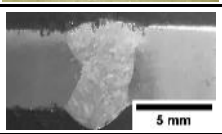
6	16.07		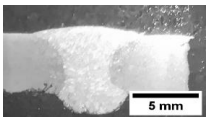
7	3.82		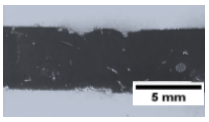
8	5.39		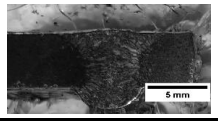

Sample No.	Heat Input (kJ/cm)	Weld Bead View	Macro Structure
9	6.63		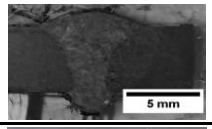
10	4.84	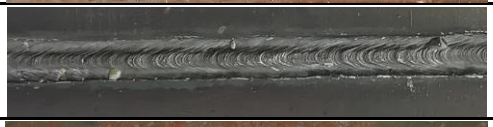	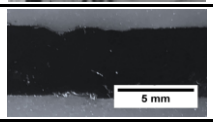
11	19.89		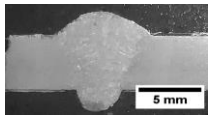
12	10.21		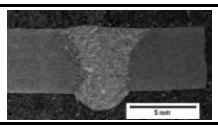
13	6.22		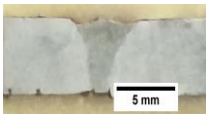
14	8.30		
15	12.77		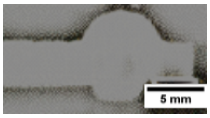
16	25.54		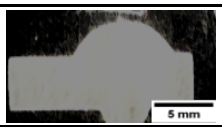

Toe angle, as shown in Figure 4.10, indicates the excess reinforcement in the weld joint and should be minimum but in positive value to avoid undercut defect.

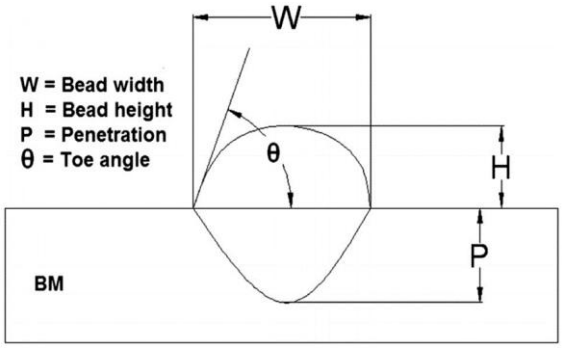

Figure 4.10: Weld bead nomenclature

At comparable weld speeds, the increase in current has caused increase in toe angle and lower weld speed for high current of 205 A changed high toe angle and excessive reinforcement. With an increase in weld speed, heat input decreases, and so is

the toe angle. The shape of the weld pool is controlled by the welding speed. At the low-welding speed of 1.25 mm/s, the pool shape was circular. As the welding speed was increased to an intermediate speed of 2.5 mm/sec, the pool shape became elliptical, and then finally, a more elongated teardrop and trapezoidal shape was observed at higher speeds.

An elliptical weld pool is an indication of adequate weld speed and epitaxial grain growth aligned perpendicular to the elliptical weld pool may avoid the centre line cracks where segregation of elements (low melting solids) may occur, causing hot cracking. Excessively low welding speeds increase the HAZ as cooling rate is low and it facilitates excessive grain growth, while at intermediate weld speeds, a tear drop shaped weld pool with equiaxed grains at the centre of weld may produce lower HAZ and defect-free joint. At high welding speeds, the grains will meet along the centerline and deposit all the contaminants and low melting phases and form a trapezoidal weld pool which should be avoided as it forms centerline cracks if proper locking of grains does not occur due to segregation of elements at the centre visible as cracks [155-157].

An increase in current at fixed heat input may not increase the HAZ width as an increase in current also increases the filler melting rate, which consumes the heat generated, causing a decrease in HAZ width and increased dilution [158, 159]. If other parameters are kept constant, then an increase in current increases the HAZ temperature and width. An increase in CO_2 content in shielding gas increases the overall heat available for fusion and increases the penetration. An increase in gas flow rate also increases carbon availability for weld pool, causing an increase in inclusion which attribute to the reduction in strength at higher gas flow rates with excess spatter.

4.4 Microstructural evolution of A572 gr. 50

Various characteristics zones of GMAW for A572 gr. 50 namely: Fusion Zone (FZ) and Heat affected zone (HAZ) containing Coarse Grain HAZ (CGHAZ), Fine Grain HAZ (FGHAZ), Intercritical HAZ (ICHAZ), Partially Transformed Zone (TZ)/ Tempered zone and Base Metal (BM) is visible from the micrograph in Figure 4.11 (sample no. 09) [160-163]. Grain size variation can be observed in Figure 4.11, with the smallest in FGHAZ followed by TZ, ICHAZ and CGHAZ respectively.

Figure 4.11: Optical micrograph of sample 09: Fusion Zone and Heat affected zone containing CGHAZ, FGHAZ, ICHAZ, TZ and BM

Microstructure plays an important role in deciding the structural integrity and strength behaviour of welded joints. Different welding parameters impart different heat input levels, and HAZ undergoes different cooling/thermal cycles producing a heterogeneous mixture of different phases in and around the weld. Cooling rate and peak temperature in WB and HAZ behaves differently to increase the loss of elements through precipitation or segregation/diffusion of elements to change the size and morphology of the base material morphology. Micro-alloyed steels gain strength through various treatments in an attempt to reduce the grain size and increase the proportion of favourable microstructural phases in the material [164]. Optical micrograph as shown in Figure 4.12 of base material A572 gr. 50 depicts the ferrite and pearlite morphology having a grain size of ~12 µm, which is relatively smaller than mild steel grain size. Pearlites are

identified by a layered structure of ferrite and cementite in the structure that may be coarse.

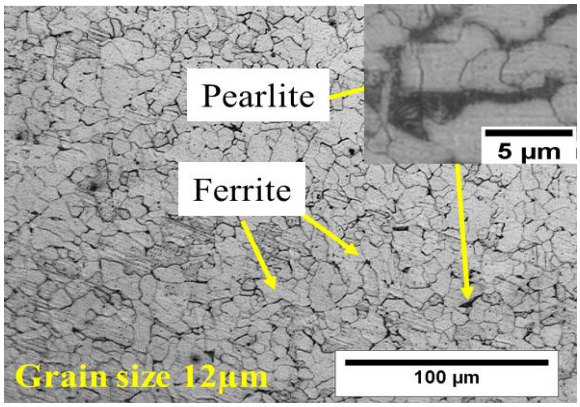

Figure 4.12: Optical micrograph of A572 at 200X (Insert shows perlite at 1000X magnification)

If transformation temperature is decreased, the lamellae become highly finer until the structure becomes irresolvable under the optical microscope. Alternatively, distorted lamellae may appear as virtually irresolvable ferrite/carbide aggregate. The perlitic structure within austenite cooled just under the lower critical temperature is obtained through the diffusional growth of cementite and ferrite from austenite. The main constituents in pearlite are 88% ferrite and 12% cementite. Carbon from the austenite grain boundary diffuses into this platelet and enhances the size of the cementite platelet. Pearlite transformation may occur at the austenite grain boundaries or at inhomogeneities such as inclusions [165].

As the heat input and process parameters vary, the cooling rate at HAZ and weld bead also changes. The rate of rejection of heat acts as another contributing factor that majorly contributes to gain different morphology. Slow cooling transforms the austenitic grains into more complex pearlite, a proeutectic phase having good ductility and but lower strength. Rapid cooling generates martensitic structure, which happens in welding, as the joint comes in contact with room temperature which is at much lower temperature, causing a quenched structure. Reheating of the welded joint (as in multi-pass welding)

may further modifies the structure to tempered martensite ($\alpha+Fe_3C$). A moderate cooling rate creates bainitic ($\alpha+Fe_3C$) structures. Different microstructural features may contribute differently to strength. Weld bead microstructure could be similar to the casted part, while HAZ can be treated as a heat-treated material part having a heterogeneous mix of phases. Figure 4.13 shows the optical micrograph of sample no. 05 at heat input of 7.64 kJ/cm. Different phases like Acicular ferrite (AF), Grain boundary ferrite (GBF)), Polygonal ferrite (PGF), Widmanstatten ferrite (WF), Upper bainite (UB) and Lower bainite (LB) generated during welding can be seen in Figure 4.13.

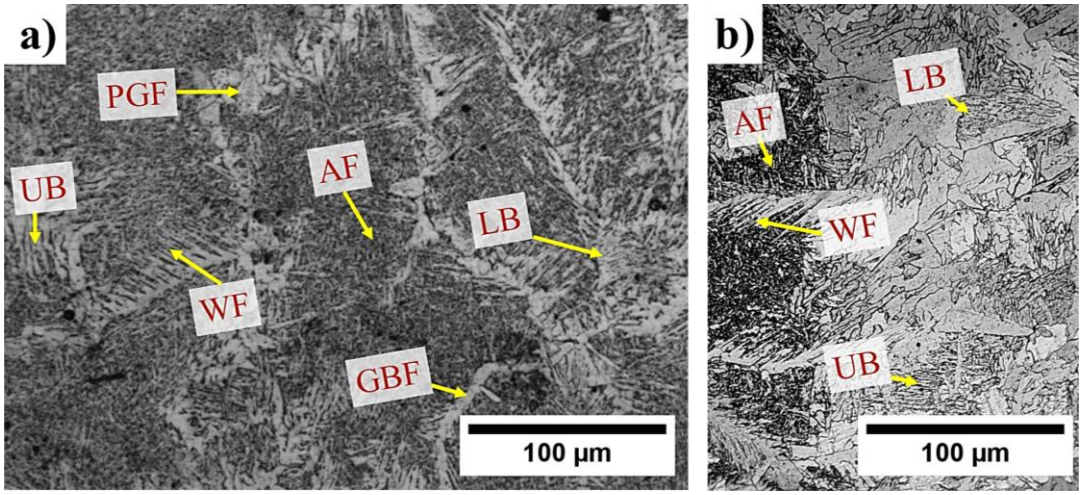

Figure 4.13: Optical micrograph of sample 05 with different morphology found in Weld joint microstructure

From Figure 4.13, Austenitic grain can be seen surrounded by grain boundary ferrite. Austenite is a face-centred cubic (FCC) structure and stable above 723°C depending upon the carbon content. It has the ability to dissolve carbon up to 2% by weight. Its size and inclusions play an important role in the formation of different micro-constituents formed during solidification, as discussed later and found by **Ghomashchi et al.** [166, 167].

Ferrite is a body centered cubic (BCC) form of iron commonly known as α iron. It is this crystalline structure that gives steel and cast iron their magnetic properties. Figure 4.13 shows various types of ferrite constituents formed that generated in welded

A572 gr. 50 steel, namely allotriomorphic ferrite, widmanstetten ferrite, and acicular ferrite. Allotriomorphic ferrite and widmanstetten ferrite are formed due to high heat input and at high temperature in A572 steel. Carbon steel with up to about 0.2% C consists mostly of ferrite and increasing amount results in the formation of cementite in a laminar structure called pearlite.

Acicular ferrite (AF) can also be seen in Sample no. 05 (Figure 4.13) and these are among the most desirable structures for higher strength and toughness in weld metal and heat affected zone microstructure. Acicular ferrite is needle-shaped crystallites or grains viewed in 2D and is denoted by AF. These nucleate intragranularly in the temperature range of 400°C to 600°C around the oxide and non-metallic inclusions. These are also characterized by high angle grain boundaries between the ferrite grains. These grow by a diffusionless mechanism in which the parent and product lattices are related by an atomic correspondence. Its interlocking nature and fine grain size (0.5-5 μm) with an aspect ratio of 3:1 to 10:1 provide maximum resistance for cracks to propagate through grains [168]. These are the lenticular plates in 3D grow by displacive transformation mechanism having 5-10 μm in length and 1 μm in diameter.

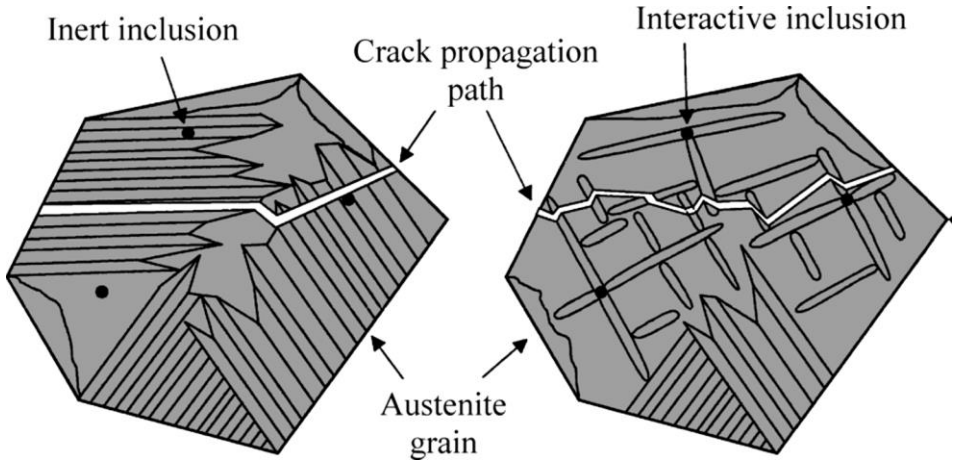

Figure 4.14: Schematic illustration of propagation path for cleavage crack in the steel grains with ferrite side plate and intragranular acicular ferrite [168]

The formation of acicular ferrite involves thermal activation. AF form in completion with widmanstatten ferrite within the austenite grain and are similar to bainite and differ by

morphology. The major classical difference between acicular ferrite and bainite is that it nucleates intragranularly in the appearance of isolated plates radiation from a point nucleation site, relatively that the cluster morphology of traditional bainite which nucleate at austenite grain boundary. From the experimental results (Figure 4.23) for strength in HAZ and WM, it can be concluded that the AF proportion determines the UTS, yield strength and Impact properties. The dominance of AF in a structure improves strength. An increase in yield strength, fracture appearance and transition temperature decreases significantly with AF proportion from 45 to 90%. The experimental results of tensile test too showed improvement of mechanical properties in HAZ and WM with an increased proportion of AF in the microstructure. The additions of Mo, Nb, Ti and Cr improved the toughness due to AF formation in the welds of A572 steel. Similarly, in submerged arc welds of X-70 line-pipe steel (0.087% C, 1.5% Mn and 0.014% Ti), TiN inclusions nucleated AF which resulted in a high toughness [166,169,170]. Steels containing acicular ferrite are better than steels with ferrite-pearlite structures with respect to strength and toughness at high temperatures.

Allotriomorphic ferrite/ Grain boundary Ferrite (GBF) can also be seen in sample no. 05 (Figure 4.13) which is formed by the diffusional mechanism in two main ways: allotriomorphic and idiomorphic ferrite. These are equiaxed crystals that nucleate inside the austenite grains, usually on non-metallic inclusion or other heterogeneous nucleation sites present in the steel. Alloying elements such as Cr, Ni, Vd, and Mo, are added to increase the hardenability causing a decrease in allotriomorphic ferrite. The growth of allotriomorphic ferrite corresponds to a diffusion-controlled process, and an idiomorph has a shape that reflects the symmetry of the crystal as embedded in the austenite.

Widmanstatten ferrite or Thomson structure is a long and pointed ferrite plates that grow along the austenitic grain boundary and are classified as primary Widmanstatten

ferrite (P-WF), and secondary Widmanstatten ferrite (S-WF) can be seen in Figure 4.13. P-WF grow directly on the grain boundary, and these are not part of allotriomorphic ferrite-austenite. While S-WF grows at the allotriomorphic ferrite-austenite boundary and grows in the form of parallel plates distinguished by the thin austenite area between them. P-WF may also grow from the oxide/non-metallic inclusions, while S-WF plates can also grow from intragranular idiomorphic ferrites [171].

At high heat input levels, the high temperature and low cooling rate at the HAZ region insist the formation of WF adjacent to the weld fusion zone which can be seen in Figure 4.14. During the continuous cooling, when the growth of the grain boundary ferrite ceases, the Widmanstatten ferrite transformation temperature is believed to have already been attained. Factors responsible for the formation of Widmanstatten ferrite are austenite grain size, chemical composition and cooling rate [172, 173]. As A572 contained 0.09% of carbon by weight, so it was susceptible to the formation of widmanstatten ferrite in HAZ of weldment [174, 175]. Fine structured widmanstatten ferrite and granular ferrite improves the ultimate tensile strength. Increase in the welding current, the heat input increases, which encourages the formation of widmanstatten ferrite. YS and UTS of steel weldment increase with an increase in the volume fraction of widmanstatten ferrite and a reduction in ferrite grain size [176]. Widmanstatten ferrite and its associated microphases are as ferrite with aligned martensite-austenitic-carbide are regarded as an undesirable constituent it leads to poor fracture toughness [177-179].

Upper Bainite (UB) and Lower Bainite (LB) which is a mixture of ferrite and carbide, and can also be seen in optical micrograph of HAZ and WB as shown in Figure 4.13. Bainite formation takes place over a wide range of temperatures. Bainitic microstructure produced in the welding process of steel may influence the weldment hardness and weldment strength. Figure 4.15 shows the schematic representation of the

transition from upper and lower bainite through diffusion followed by precipitation at lower temperatures. Bainite can be seen as a non-lamellar aggregate of the plate formed of carbide and ferrite. Upper bainite generates at higher peak temperature, while lower bainite at a lower temperature [180]. Bainites are distinguished through their shape, size and their lath size. The big difference between bainite and acicular ferrite is that it nucleates intragranularly in the form of isolated plates radiating from a point nucleation site. Upper bainite consists of the plate of ferrite near each other, which are very nearly the same crystallographic orientation in space. Upper bainite is formed at around 400-550°C in sheaves (growth of plates takes place in clusters called sheaves). Lower bainite is quite similar to upper bainite, except that the amount of interplate cementite is low, and carbide can be found within the ferrite plate itself. Lower bainite is formed at 250-450°C. This intra-ferrite carbide is found to be mostly cementite as in case of low carbon steels with carbon content lower than 0.55% by wt. Figure 4.15 shows a time-temperature curve for steel for the formation of the different constituents such as ferrite, pearlite, bainite, widmanstatten ferrite and martensite at different temperature ranges [181].

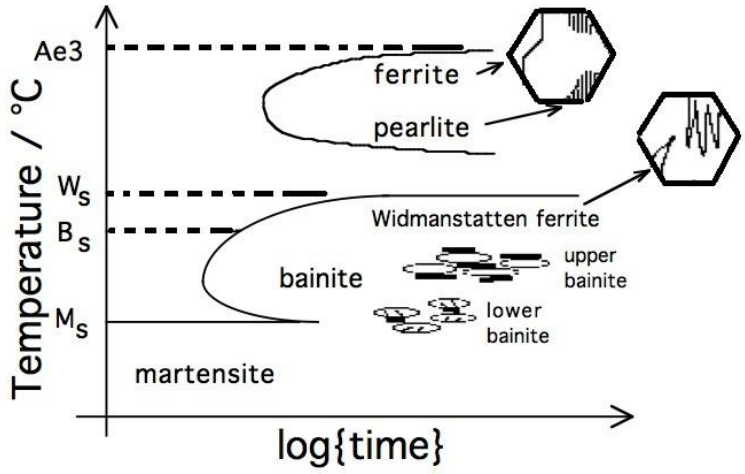

Figure 4.15: The formation of martensite, bainite etc. [181]

Another constituent found in weld joint in the form of fine black dots dispersed in a matrix is Martensite (Figure 4.13). These are very hard and have less ductility formed as a result of a diffusionless transformation, where carbon is retained in solution [182]. It is a product

of a rapid and diffusionless transformation and is found in the form of either laths or plates. Its substructure gains its strength through a high density of dislocations arranged in cells where each martensitic lath is composed of many dislocation cells. The substructure of plate martensite consists of very fine twins, i.e., twinned martensite [183]. At rapid cooling rates, the austenite may reach the temperature of 400°C depending on alloying before the transformation. Transformation at these temperatures is a diffusionless process for the formation of lath martensite. When martensite is heated up to a temperature of 600°C, it becomes soft, causing toughness improvement in steel. A higher cooling rate as in high-speed welding martensite formation took place. If austenite (γ) is cooled down from high temperature, ferrite (α) nucleates at the grain boundary and grows inside the grain. At low temperatures, the mobility of the planar growth front of the grain boundary ferrite decreases and Widmanstatten ferrite also called side-plate ferrite, forms instead. These side plates can grow faster because carbon, instead of piling up at the planar growth front, is pushed to the sides of the growing tips. At even lower temperatures, it is too slow for Widmanstatten ferrite to grow to the grain interior and it is faster if new ferrite nucleates ahead of the growing ferrite. This new ferrite, that is, acicular ferrite, nucleates at inclusion particles and has randomly oriented short ferrite needles with a basket weave feature.

4.4.1 Effect of Heat input

As crystals of weld deposit have derived from the grains of base material at fusion surface (called epitaxial growth), the grain size in HAZ affects the strength and toughness of weld metal too. For all the 16 samples, austenite grain size affected the microstructure and mechanical properties of HAZ and WB. Austenite grain size decreased gradually with an increase in distance from the fusion zone. The coarse grains in HAZ adjacent to the fusion zone are susceptible to reduced strength properties, especially toughness. Acicular

ferrite and martensite can also form depending on the cooling rate and chemical composition [184]. Increasing HI will result in a wider coarse grain area in HAZ. Therefore, there will be a wider low strength area for high heat inputs. The low heat input welds showed 3-phased microstructure having fine grain boundary ferrite (GBF), Widmanstatten ferrite(WF) and Acicular ferrite(AF) colonies, as shown in Figure 4.16 for HI of 6.05 kJ/cm (Sample no. 02) with a larger amount of inclusions. Coarse grain HAZ(CGHAZ) mainly contained ferrite and a small amount of pearlite. Grain size reduction was found from the Weld bead to the base material due to heat transferred from the weld pool to the base material due to conduction preferably. HAZ width was found to be ~2.44 mm. On further increase in HI of 7.64 kJ/cm for sample no. 05 (Figure 4.17), the size of inclusions reduced and increased ferrite content, improving the strength further with HAZ width 3.04 mm. Grain size in CGHAZ too increased with HI. For the high heat input of 10.21 kJ/cm (sample no. 12), the microstructure predominantly consists of AF and coarse GBF. Increasing the HI has reduced the inclusion and caused excessive gain coarsening in HAZ with an increase in grain size, as shown in Figure 4.16 to Figure 4.20. Inclusions formed in the WM have two opposing effects on strength, especially UTS. On one hand, they can assist the intragranular nucleation of acicular ferrite that refines the WM microstructure and improves both strength and toughness effectively. On the other hand, they can act as the initiation sites not only for ductile fracture but also for cleavage fracture [154, 185, 186].

For sample no. 09 welded at HI of 6.63 kJ/cm, AF structure was more dominant, causing an increase in strength overall. As the current has been increased from 100 A to 170 A, the electrode melting rate has also increased, and an increase in HI is utilized in melting the electrode, which transferred lesser heat to HAZ, causing lesser coarsening in HAZ. Grain size in CGHAZ and FGHAZ were similar in size, around 22 μm. As the

proportion of AF in WM and reduction in grain size in HAZ and width (1.44 mm) occurred, the UTS and YS obtained were highest. Sample no. 09 welded at Current- 170 A, Voltage- 16 V, Gas flow rate- 10 l/min, and Weld speed- 3.75 mm/sec depicted the highest strength levels and is also verified through Taguchi's analysis. For higher weld speed of 5.0 mm/sec at Heat Input: 6.22 kJ/cm (Sample no. 13) Current- 205 A, Voltage- 16 V, Gas flow rate- 10 l/min Increase in current increased grain coarsening and grain size in HAZ with undercut at higher speeds (at top) as seen from Figure 4.20. Also, GB ferrite has increased, reducing the strength further. HAZ width calculated was 2.04 mm.

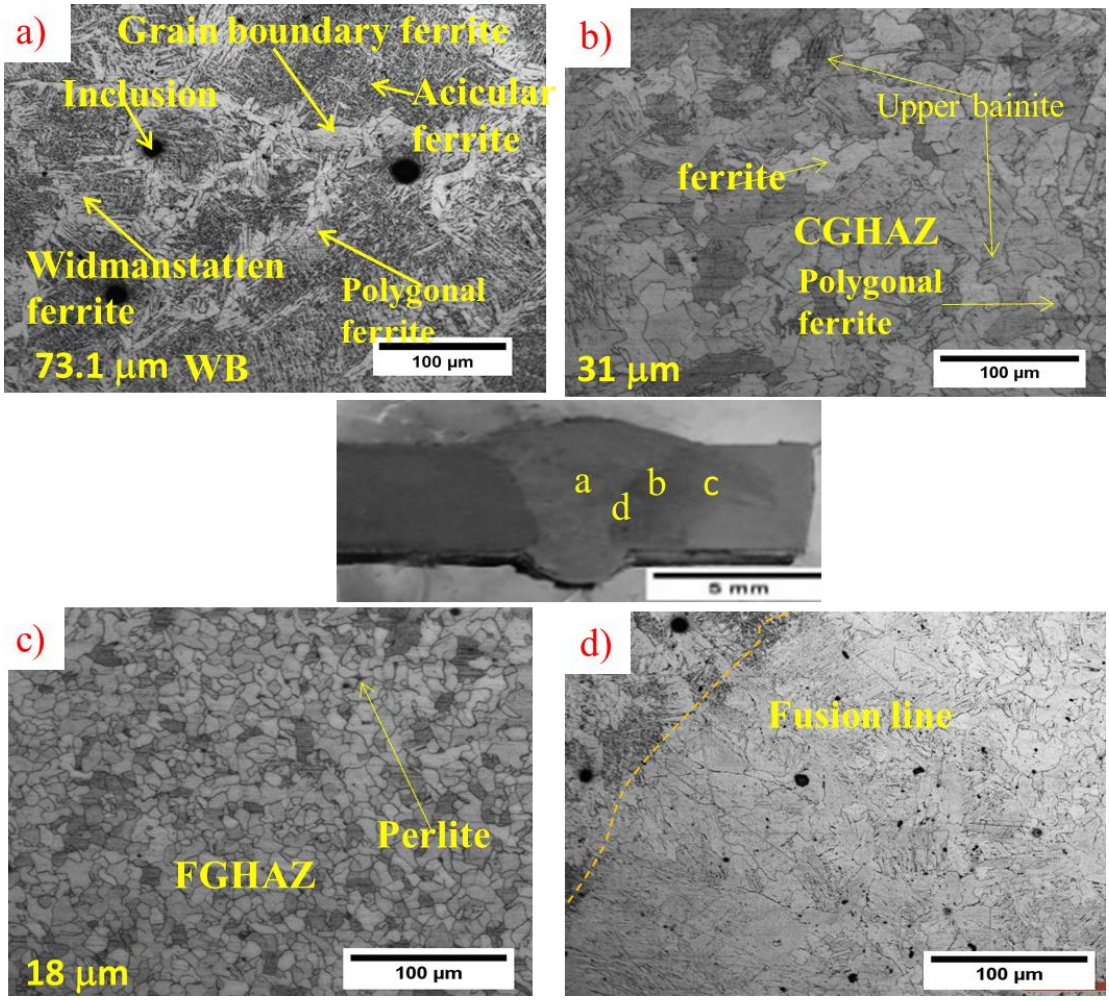

Figure 4.16: Optical micrograph of Sample no. 02 at 200X: Heat input- 6.05 kJ/cm, Current- 100 A, Weld speed- 2.5 mm/sec and Gas flow rate-14 l/min

A similar pattern was observed for the welds, with an increase in welding current causing an increase in HI. At lower HI levels a faster cooling rate can pass into a fairly

narrow window of acicular ferrite and aligned ferrite. Whereas, slow cooling rate or high heat input will produce blocky ferrite or grain boundary ferrite and acicular ferrite. Higher heat input also allows more time for diffusion along the grain boundary, and the GBF became coarser.

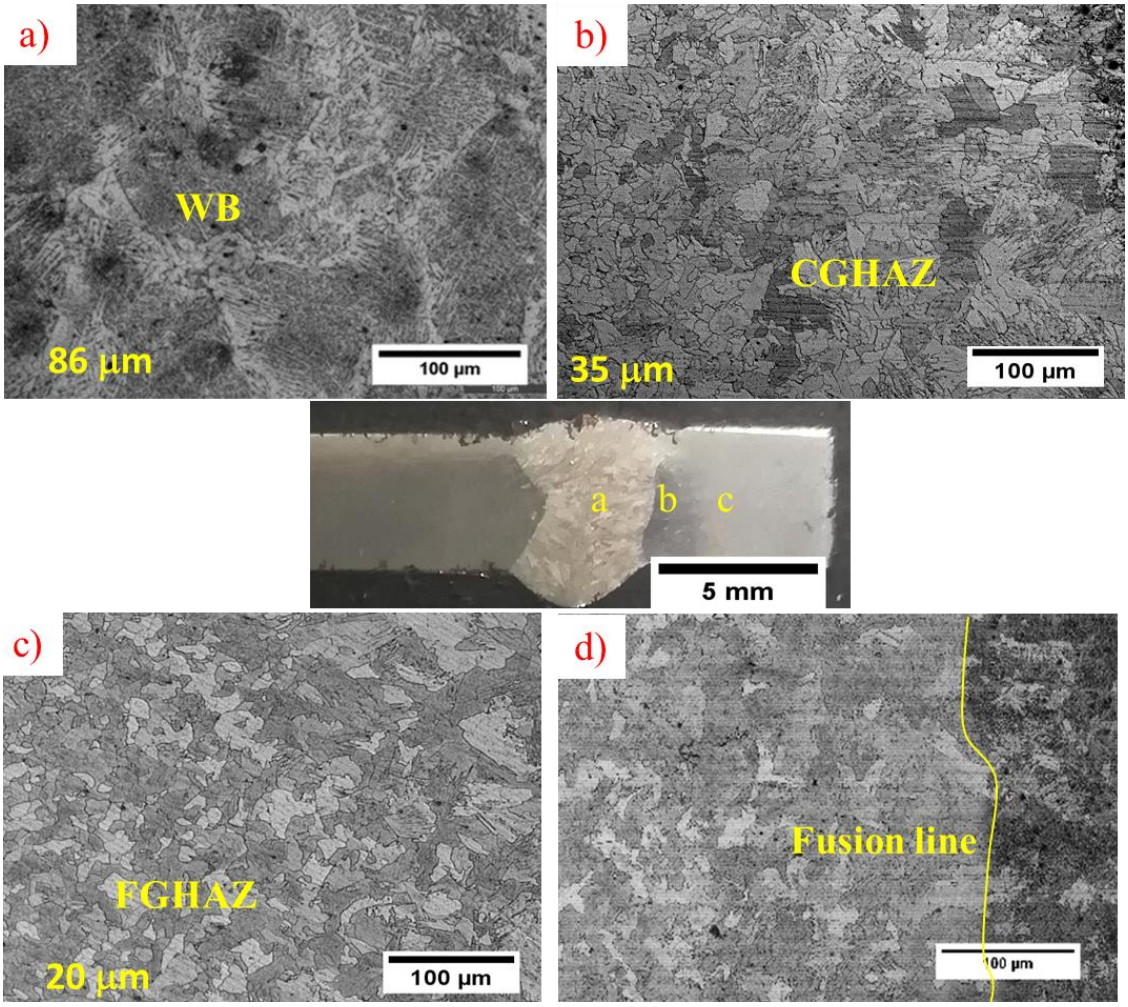

Figure 4.17: Optical micrograph of Sample no. 05 at 200X: Heat Input- 7.64 kJ/cm, Current -135 A, Voltage- 17 V, Gas flow rate- 10 l/min, Weld speed- 2.5 mm/sec

The actual completion temperature of α to ɣ transformation depends on the local heating rate and varies between different locations in the HAZ. The subsequent phase transformation (ɣ to α) depends on the cooling rate (HI) of respective butt welds. Faster cooling will produce different types of ferrite morphologies such as primary ferrite, polygonal ferrite, allotriomorphic ferrite, ferrite side plates and few acicular ferrite as shown in Figure 4.18.

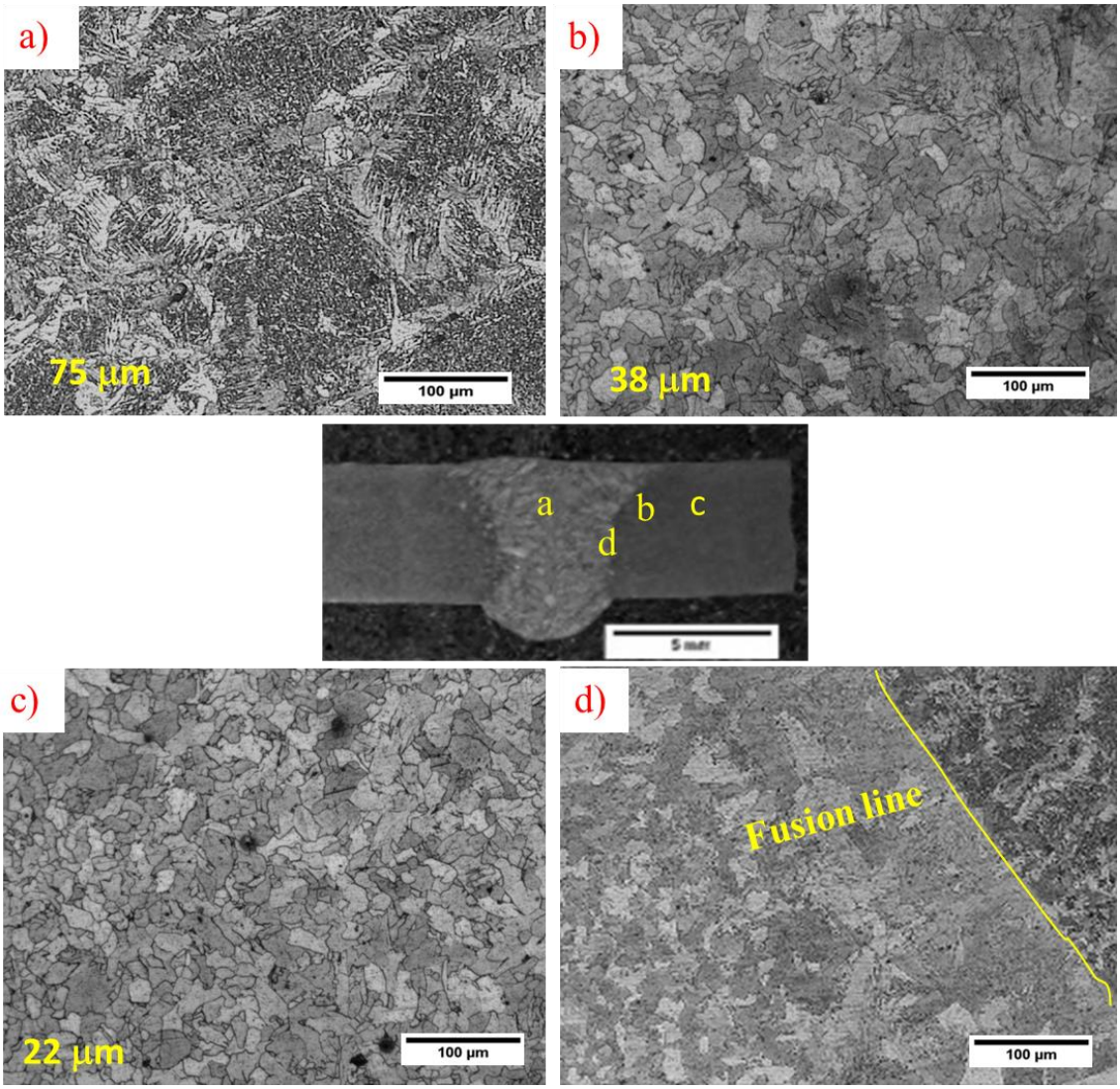

Figure 4.18: Optical micrograph of Sample no. 12 at 200X: Heat Input: 10.21 kJ/cm, Current -170 A, Voltage -17 V, Gas flow rate-19 l/min, Weld speed-2.5 mm/sec

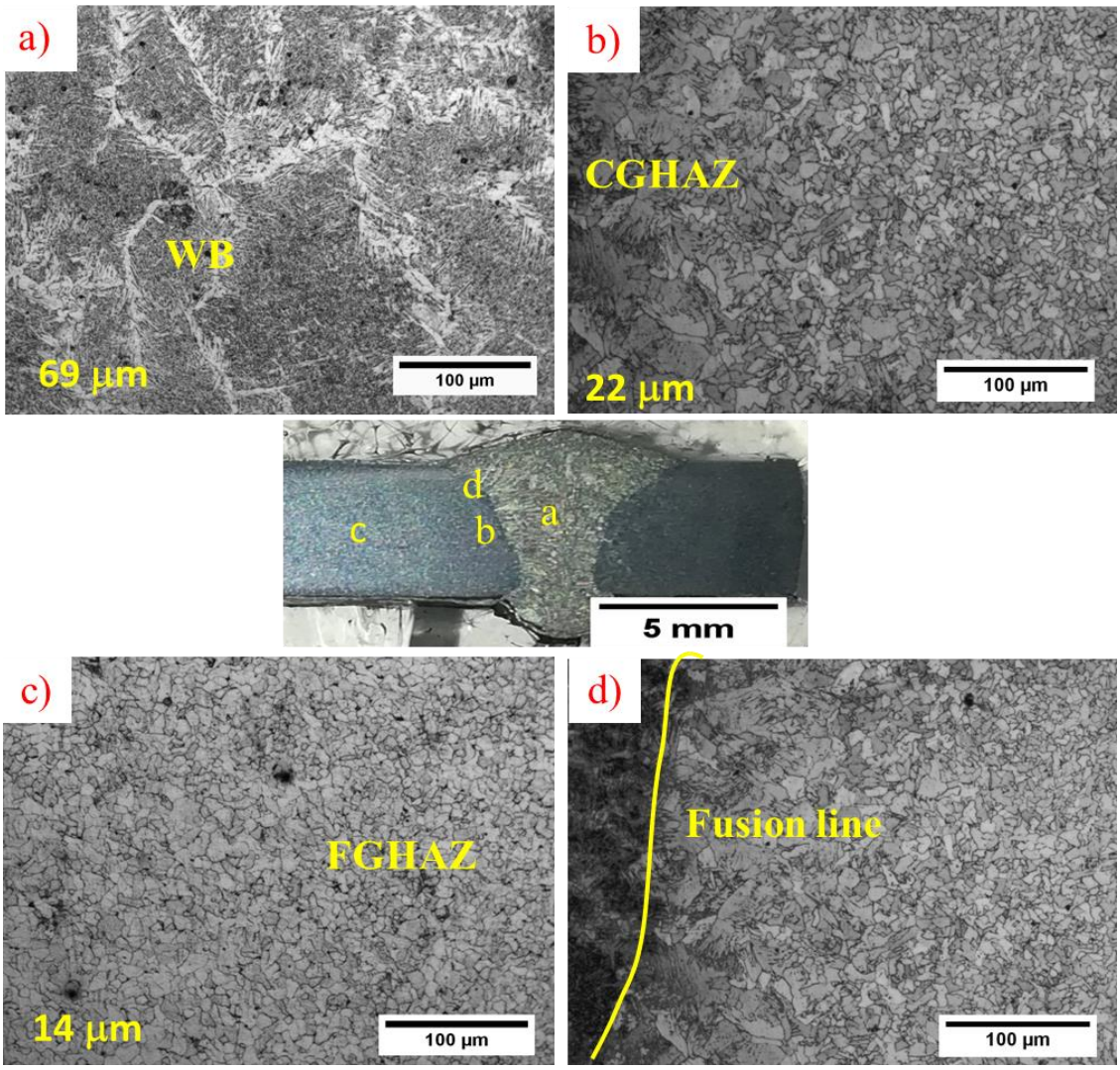

Figure 4.19: Optical micrograph of Sample no. 09 at 200X: Heat Input: 6.63 kJ/cm, Current -170 A, Voltage -16 V, Gas flow rate-10 l/min and Weld speed-3.75 mm/sec

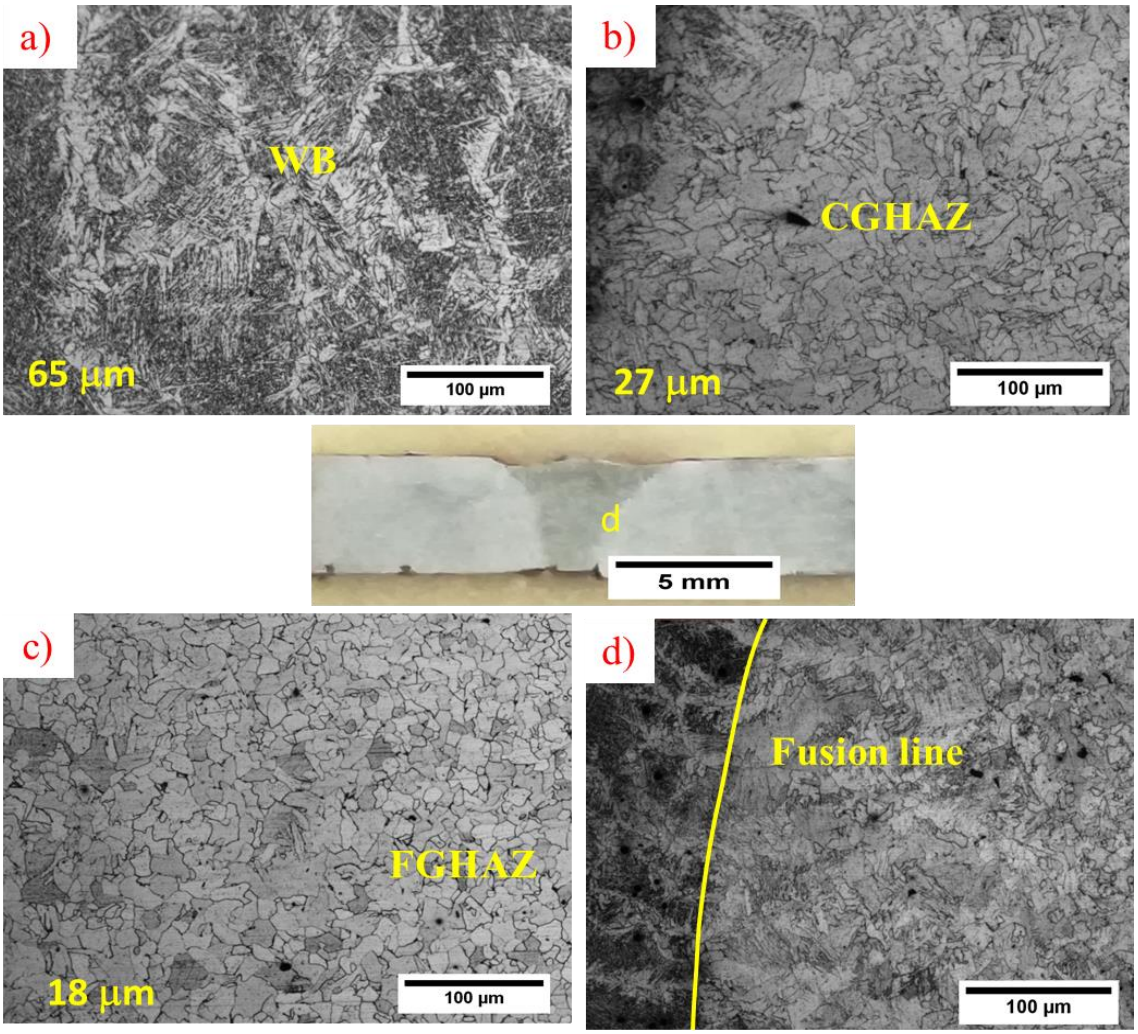

Figure 4.20: Optical micrograph of Sample no. 13 at 200X: Heat Input- 6.22 kJ/cm, Current- 205 A, Voltage- 16 V, Gas flow rate-10 l/min, Weld speed- 5.0 mm/sec

4.4.2 Effect of Welding current

The increase in current would result in an increase in heat input if all other parameters were kept constant. It has been observed that higher dilution is associated with high welding current, high speed and voltage. GB ferrite increased with an increase in welding current and caused a rise in the level of HAZ grain coarsening effect. AF and WF ferrite content too increased with an increase in weld current. From Figure 4.21, it can be concluded that the increase in current caused the reduction in inclusion in WB. Austenitic grain size increased initially, followed by a decrease and highest for current of 205 A. But in CGHAZ and FGHAZ increase in current increased the gain size, causing an increase in YS and UTS up to 170 A current, followed by a decrease due to excessive

grain growth. Proportion AF and thin GBF increased the overall strength levels.

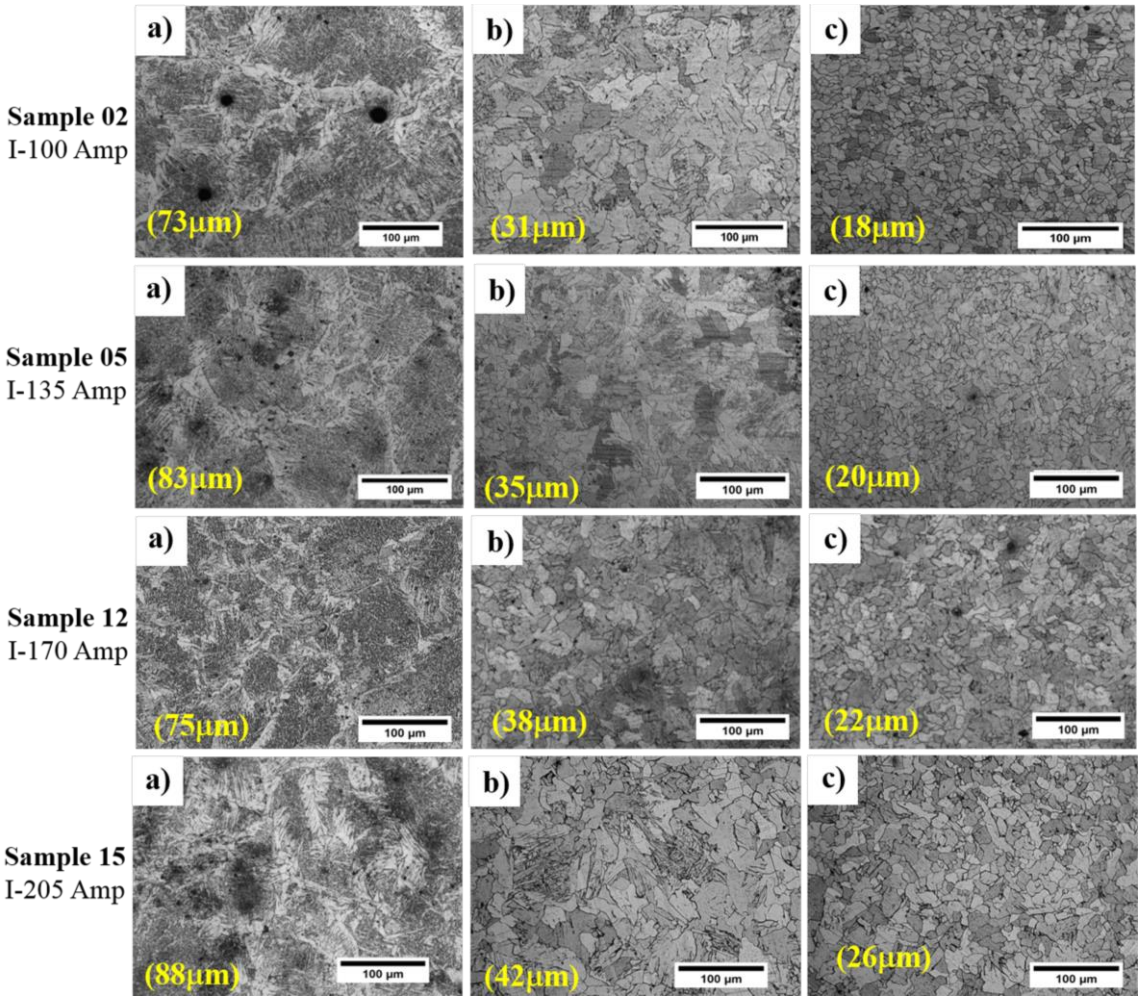

Figure 4.21: Effect of Current on microstructure of a) WB, b) CGHAZ and c) FGHAZ

4.4.3 Effect of Shielding Gas flow rate

It is evident that with an increase in CO_2 content in the shielding gas mixture, the depth of penetration increases due to higher reactivity of CO_2, causing increases in grain size due to the higher heat input. CO_2 has high specific heat and is able to constrict the arc plasma, thereby increasing the current density near arc axis with respect to pure argon and helium [61]. CO_2 breaks into CO and O_2 releasing heat that increases the fluidity of molten weld pool. CO_2 addition to Ar, changes the current-voltage characteristic resulting increase in the current density and results in an increase in metal transfer frequency [187]. Degree of oxidation is high for pure CO_2 and increases with higher quantities of CO_2 in the shielding gas and the microstructure of deposited weld metal is a coarse structure. In

all specimens welded with 82% Ar +18% CO_2, the HAZ has a dendritic structure with ferrite, pearlite and carbides dispersed in the matrix. The percentage of Acicular Ferrite is found high with less fraction of (GBF). The effect of gas flow rate under the test range of 10 to 19 l/min at HI of 6 to 12 kJ/cm has been shown in Figure 4.22.

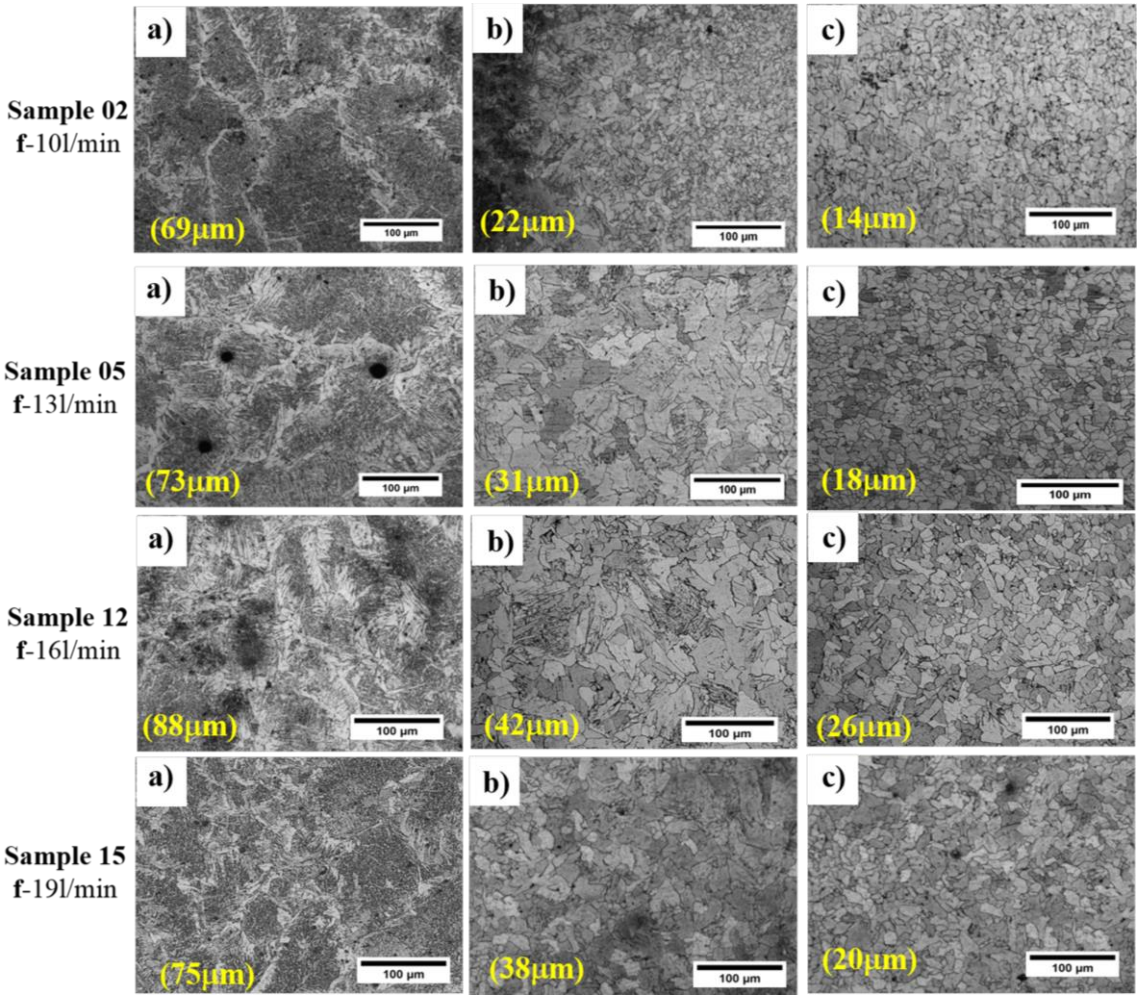

Figure 4.22: Effect of Gas flow rate on microstructure of a) WB, b) CGHAZ and c) FGHAZ

Grain coarsening variation has been found minimal in HAZ due to an increase in gas flow rate. Grain size in HAZ has slightly decreased due to heat taken away by shielding gas. Grain coarsening for a gas flow rate of 16 l/min was maximum with a grain size of 42 µm for sample no. 15. Again gain size in HAZ decreased, further moving away from the fusion zone. An increase in gas flow rate has increased the size of inclusions and further decreased the UTS and YS.

4.4.4 Effect of welding speed

Weld speed increase reduced the total heat input produced a less coarsening effect in HAZ and WB. At weld speed of 3.75 mm/s grain size in the HAZ was 22 µm for sample no. 09 is almost similar in size to the base material. A decrease in overall heat imparted shifts the cooling curve towards the AF region. Therefore, high weld speed associated with faster cooling, in general, produces more AF and finer GBF in the final microstructure of weld metals. From the microstructure in Figure 4.23, it can be seen that for lower weld speed, peak temperature was higher, and cooling rate was low, which provided sufficient time for the growth of grains in CGHAZ.

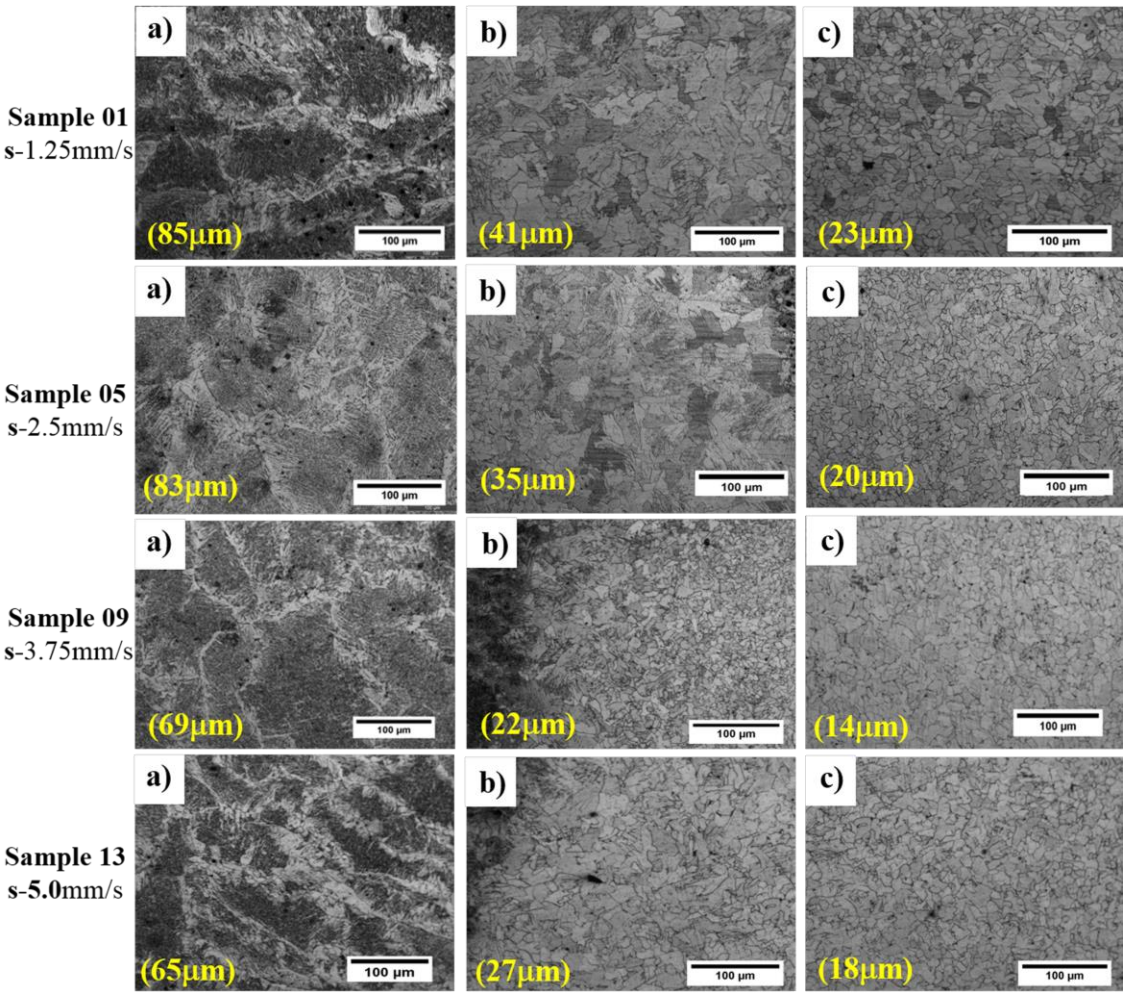

Figure 4.23: Effect of Weld speed on microstructure on microstructure of a) WB, b) CGHAZ and c) FGHAZ

Further, an increase in welding speed reduced the HI, and lower grain coarsening occurred, which ultimately increased the UTS and YS. At a welding speed of 5 mm/sec

it was observed that, the amount of GBF and WF increased along with a decrease in the proportion of AF in the weld metal. For higher speed, there was a decrease in mean effective UTS and YS as higher welding speed increased the precipitation of alloying elements from the matrix, thereby reducing the strength level. An increase in weld speed reduced the grain coarsening effect, causing an increase in overall strength.

4.5 Mechanical Properties of A572 gr. 50 Weld joint

The mechanical properties of a material are greatly influenced by HAZ and WB microstructure, grain size and its morphology dictated by heat available during welding. Austenitic grain size and inclusions in weld bead dictate various phase formation and ultimately the UTS and YS, while in HAZ zone, grain size and phases on material significantly affect the YS following the Hall-patch equation.

4.5.1 Hardness Distribution in HAZ and WB for A572 gr. 50

Hardness is the ability of the material to resist plastic deformation, and the resulting indentation is measured in terms of the area of indentation for a particular load. Considerable variation in hardness can be realized while moving away from the weld centerline. For analysis of microhardness, the hardness distribution in different zones for sample no. 11 has been shown in Figure 4.24. From Figure 4.24, it can be observed that there is a sudden dip in the hardness profile while moving away from the weld center, which indicates the CGHAZ hardness dip. It is recommended that CGHAZ size should be less than half of the plate thickness for a safer joint [188]. It can be observed that the average hardness value in WZ is higher than that of the base metal, however it is lesser than the average hardness value of the heat-affected zone. Among the various zones of HAZ, Fine Grain HAZ (FGHAZ) exhibited the maximum hardness for all the samples due to the smaller grain size. Small grain size caused interaction of higher number of grain boundaries with diamond indenter resisting the plastic deformation which increased

the hardness. The average hardness value obtained for the heat-affected zone is on the higher side, which may be due to the hardening effect.

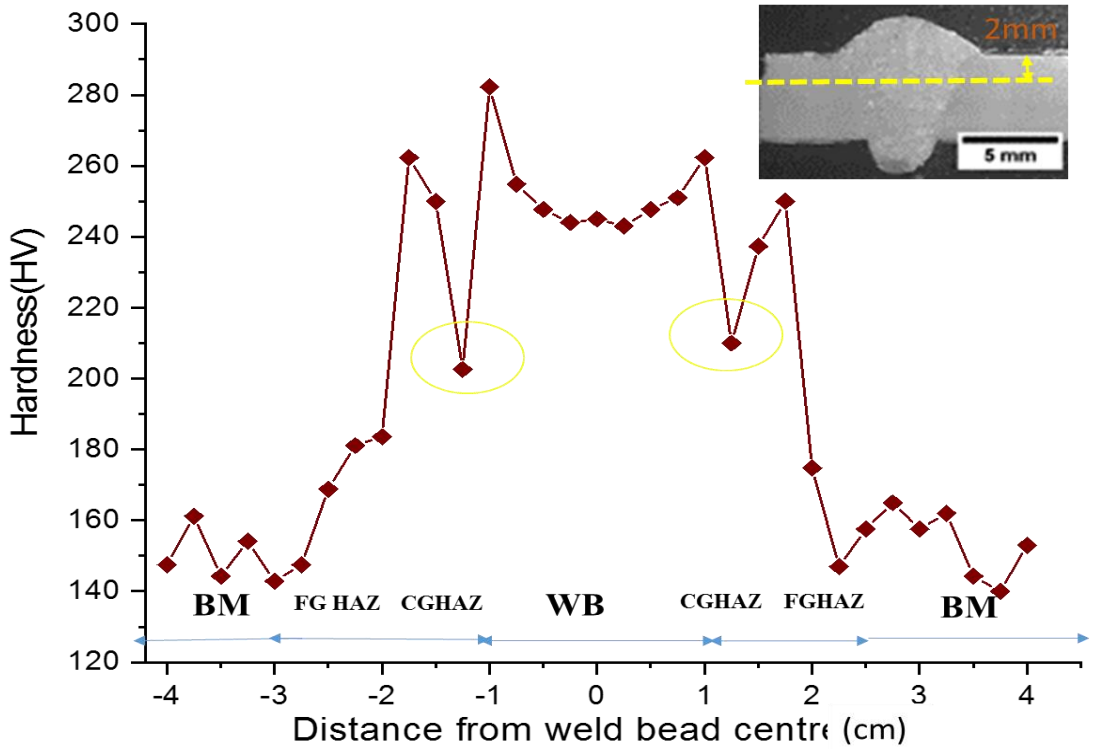

Figure 4.24: Hardness distribution 2 mm below the surface for Sample no. 11

The hardness value for all 16 samples in different zones of HAZ with an error of ±7 HV has been tabulated in table 4.3. It can also be observed from Table 4.3 that, for all 16 samples, the hardness value for the base material is almost constant everywhere, having a hardness of 166±7 HV. Further highest hardness was observed in FGHAZ of all the 16 samples. The heat-affected zone experienced multiple heat cycles during welding, due to which coarse as well as fine grains were formed. The fast cooling rate in this region led to the formation of martensitic structure and higher hardness as compared to the base metal and weld area. It was found that the hardness of all zones of weld joints of weld pool and HAZ enhances with the increase of weld speed and current due to faster solidification of weld pool at higher speed. The average hardness value obtained for the heat-affected zone was 255 HV, and 290 HV is the highest on FGHAZ for sample no. 11, which may be due to the strain hardening effect. As from the micrograph, grain size is

smallest, which increases the number of gain boundaries interacting the indenter and hindering the plastic deformation and movement of dislocations.

Table 4.5: Average Hardness variation in various zones of HAZ and WB

Sample No. (Exp. No.)	**Heat Input** (kJ/cm)	**Hardness** (HV)		
		WB	CGHAZ	FGHAZ
1	12.1	260	222	275
2	6.05	264	234	269
3	3.99	264	255	265
4	3.11	271	262	270
5	7.64	263	230	265
6	16.07	250	225	258
7	3.82	268	242	271
8	5.39	261	255	268
9	**6.63**	**278**	**273**	**285**
10	4.84	280	274	290
11	19.89	262	215	269
12	10.21	272	265	281
13	6.22	270	235	275
14	8.3	258	210	264
15	12.77	251	190	258
16	25.54	239	185	249

The microhardness variation can be attributed primarily to the heat input. The decrease in hardness value in the heat-affected zone due to coarser grain size is mainly attributed to the annealing effect. The higher hardness values in the fusion zone were due to the rapid cooling, influenced by the increased gas flow rate. From the bar chart in Figure 4.25, it can be analyzed that hardness variation and HAZ softening was the least

for sample no. 09. Maximum hardness was found in the FGHAZ (290 HV), followed by WB (280 HV) and CGHAZ (274 HV).

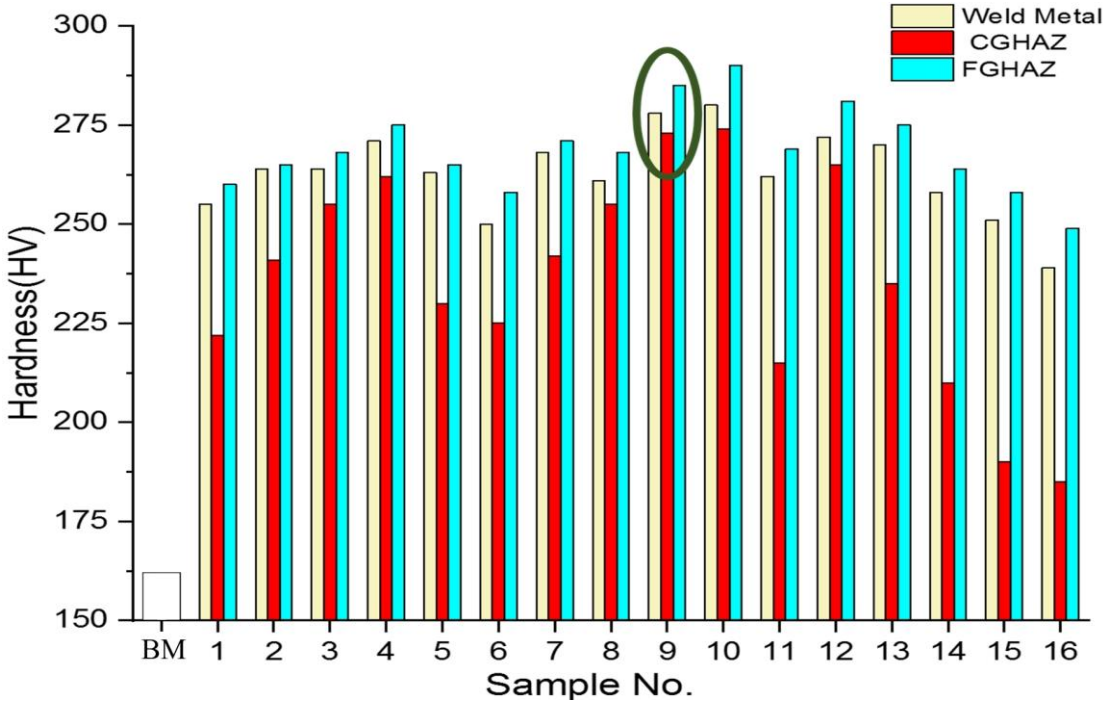

Figure 4.25: Average Hardness in Weld Metal, CGHAZ, FGHAZ and Base metal (BM)

An increase in heat input has caused a decrease in overall hardness in HAZ and weld bead due to the grain coarsening effect in the CGHAZ. A reduction in hardness in most of the samples was observed in CGHAZ due to grain growth. An increase in grain size reduced the energy required for plastic deformation during the hardness test showing lower hardness.

An increase in gas flow rate has increased the hardness in HAZ due to heat removal from HAZ at low current levels. At high heat input, hardness decreased with gas flow rate. Higher flow rate increased turbulence in the weld pool and increased inclusion sizes in the weld bead. From the line diagram in Figure 4.26 for hardness in different zones, it can be found that with respect to base material (BM), the hardness increased considerably. At constant current with an increase in gas flow rate hardness increased (From 01 to 04 and 16 to 13) depending upon HI.

From the bar diagram shown in Figure 4.25, it can be deduced that with an increase in weld speed (from sample 01-04 and 16-13) hardness in WB and FGHAZ has increased due to reduction in HI. The grain size was largely affected by reduction in heat input which restricted the indentation area and increased hardness. With an increase in current, there is a larger variation CGHAZ with respect to WB and FGHAZ due to coarsening effect in CGHAZ for the samples.

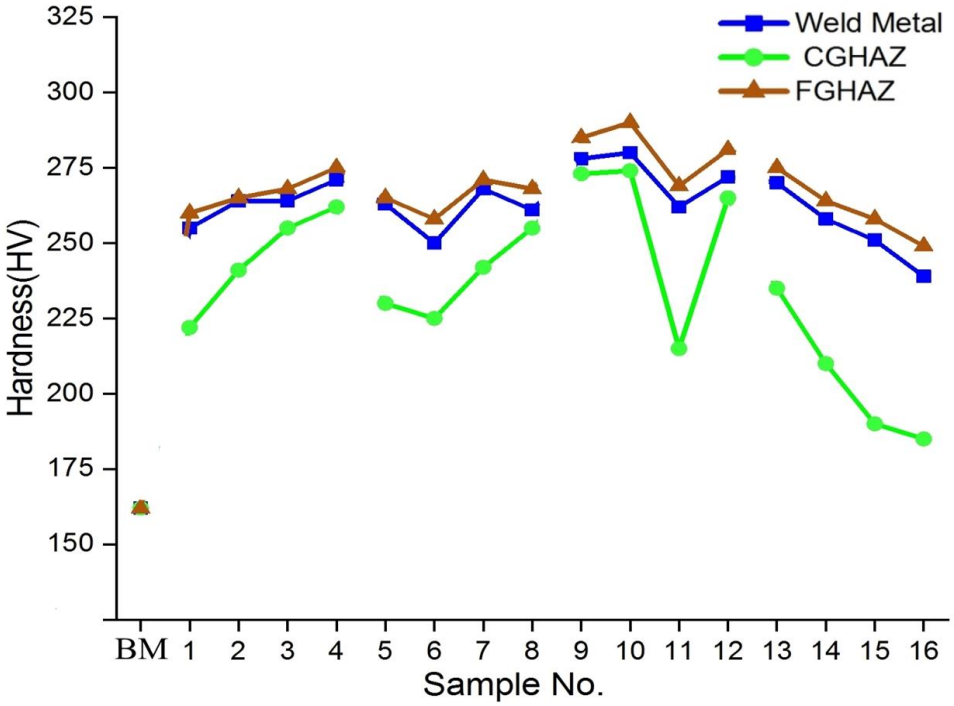

Figure 4.26: Line diagram of Average Hardness in zones of Welded joint

4.5.2 Tensile Properties of A572 gr. 50 Weld joint

Generally, the weld metal is kept comparatively stronger, and the joint properties are controlled by weld metal chemical composition and microstructure. In uniaxial tensile tests, the base material fractured from center having a ductile mode of fracture as revealed from SEM analysis having UTS and YS as 395 MPa and 325 MPa respectively. All welded specimens fractured away from weld bead, i.e. either in base metal or HAZ. Figure 4.27 depicts the prepared tensile test specimens for different current levels for Sample no. 04 (I-100 A), 05(I- 135 A), 12(I- 170 A) and 15(I- 205A) before fracture and after fracture. Sample no. 04 fracture from weld bead having lowest strength. It can be

observed that the specimens fractured from the gauge region and HAZ. Various results of the tensile test have been tabulated in Table 4.1. Maximum UTS and YS were observed for sample no. 9 with parameters of 170 A current, 10 l/min gas flow rate and 3.75 mm/sec weld speed and is in agreement with the results obtained from Taguchi analysis. From the interaction plots of UTS as shown in Figure 4.6, it can be deduced that an increase in current along with heat input has increased the UTS (as it reduced the size of inclusion as revealed from microstructure) up to 170 A current level followed by a decrease. As the grain coarsening effect became more dominant for higher HI, causing an increase in grain size and reduction of UTS and Ys. A similar effect with an increase in heat input due to a decrease in cooling rate was obtained. Nb, Ti, V, etc., being strong carbide/nitride forming elements, contributing to strength by precipitation hardening as they have limited solubility in ferrite and austenite [189]. It may be the reason that the yield strengths of most of the welds increased compared to the parent metal. The percentage elongation of the yield point is attributed to the interaction of solute atoms and moving dislocations [190]. The fractured tensile samples are shown in Figure 4.27.

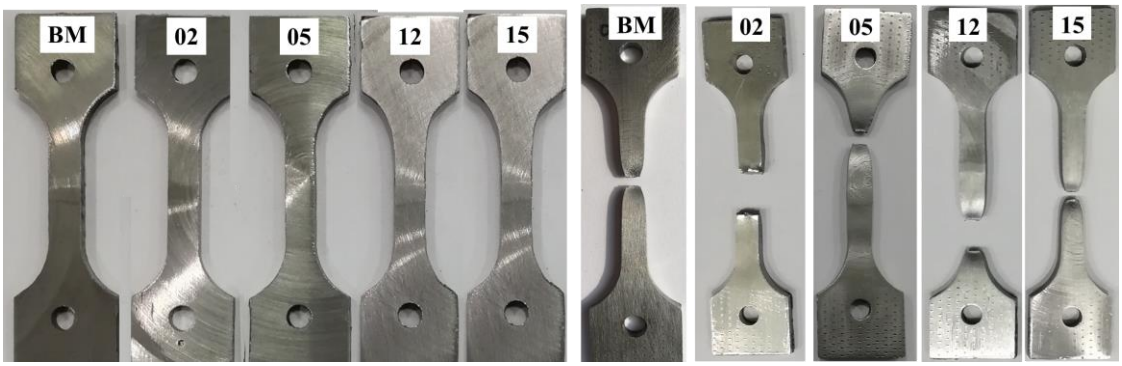

Figure 4.27: Fractured BM and tensile specimen at different current levels of Sample no. 02 (I-100 A), 05 (I-135 A), 12 (I-170 A) and 15 (I-205 A)

The tensile tests revealed that ductile materials containing large voids generally fail from WB prior to necking, and if a neck is already formed, then the void formation becomes much more dominant. Lower HI and high gas flow rate reduced tensile strength and ductility. It can be seen that the shielding gas mixture of Ar and CO_2 improved the

penetration and produced weld of good strength. A gas flow rate of 10 l/min produced joints with UTS values 375 MPa (Sample 01), 404 MPa (Sample 05), 435 MPa (Sample 09), which increased up to maximum, followed by a decrease to 399 MPa (Sample 13). HI also contributed to grain coarsening, causing a decrease in strength at higher HI levels. Compared to the welded joint made with a higher gas flow rate of 19 l/min, the tensile strength of the welded joint made were 399 MPa, 410 MPa, 418 MPa, and 378 MPa followed a similar trend. The tensile testing results suggest that all the fractures occur at the HAZ and BM except samples 04, 07 and 13 for the lowest HI and high speed. It is consistent with the hardness test results.

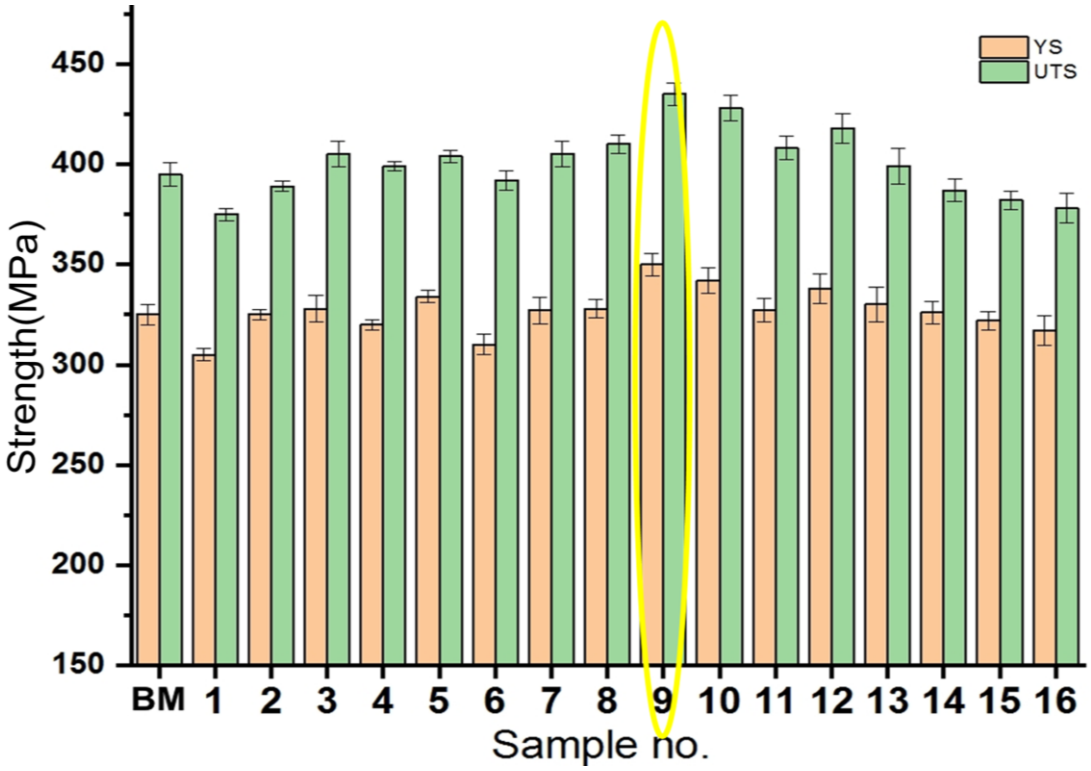

Figure 4.28: Strength Variation for base material and welded samples as per L16 array

From the bar chart shown in Figure 4.28, it can be concluded that the heat input influences the tensile strength of the weld. An increased heat input resulted in increased strength up to optimum, followed by a decrease as seen for samples 01 to 04 and 16 to 12. It was found that a reduction in inclusion size up to fine inclusion consequently increased the tensile strength up to an optimum level of the weld. From Figure 4.28, UTS

and YS increased with a decrease in HI caused due to smaller grain size in HAZ and WB. There is a larger variation in YS with respect to UTS as ductility is largely affected by grain growth in HAZ and grain morphology in HAZ. For higher HI, i.e. sample no. 01, 06, 11 and 16, lower YS was observed. Apart from sample no. 09, which exhibited maximum UTS and YS samples joined at HI around 6 kJ/cm and 10 kJ/cm too exhibited comparable strength 170 A and weld speed of 3.75 mm/sec. From the line diagram in Figure 4.29, it can be deduced that increase in current levels increased the UTS up to 170 A, followed by a drop due to higher grain coarsening. With an increase in weld speed and a decrease in HI, there is an increase in UTS. With an increase in current, there is a larger variation in YS due to increased soft zone caused by coarsening effect in CGHAZ.

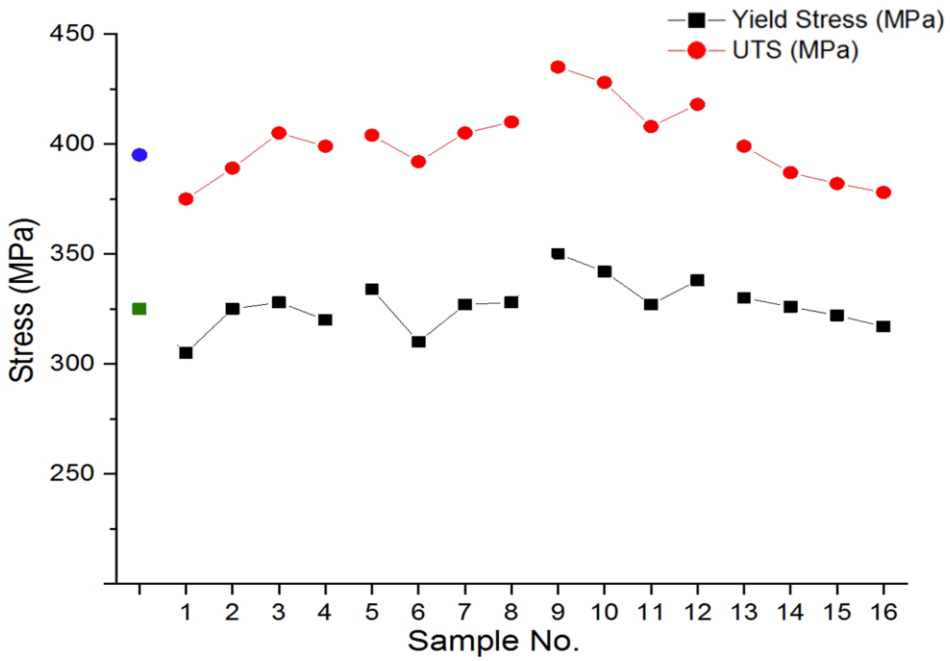

Figure 4.29: Line diagram showing Strength variation among samples

SEM fractography of A572 steel consists of features of ductile fracture showing plastic flow lines in the form of white lines around the dimples. The dimples become deep with increasing current up to 170 A, indicating an increase of strength. Cracks have been found for lower current fractographs, as shown in Figure 4.30. SEM images for samples 12 and 09 reveal that a large number of smaller dimples mixed with several larger dimples distributed on the fracture surfaces. After observing the fractured specimens, it can be

seen that they have a ductile type of failure. During the testing, it was observed that the specimens welded at 170 A current level showed higher strengths with deep dimples in fractured samples. The two possible mechanisms responsible for the strengthening of HAZ may be dispersion strengthening and/or grain refinement. As discussed in the microstructure section, Grain refinement played a dual role by enhancing strength and ductility. Grain refinement increases the number of grain boundaries that impede dislocation's movement and coordinate mutually during plastic deformation. SEM image of tensile fractograph for variable current and weld speed can be seen in Figures 4.30 and 4.31. Sample no. 09 contains coarse as well as fine dimples, which shows the heterogeneous nature of HAZ microstructure. The presence of fine dimples along with coarse dimples indicates that higher resistance is offered by weld before fracture.

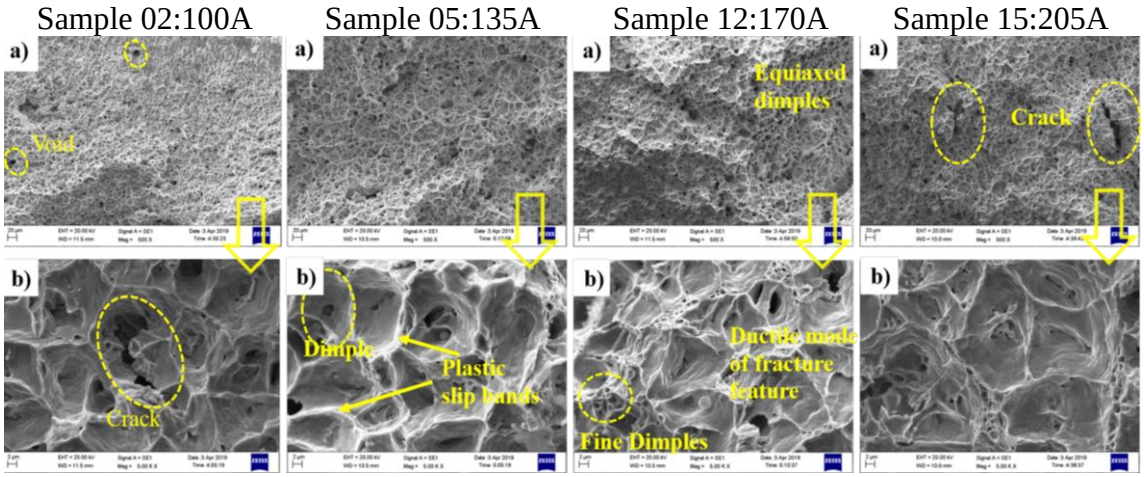

Figure 4.30: Effect of current: SEM micrograph of fractured tensile specimen

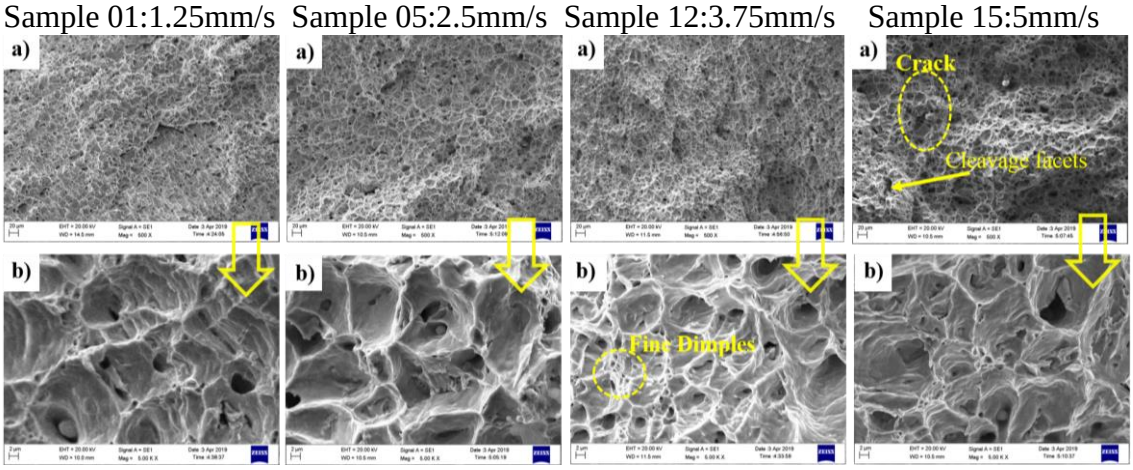

Figure 4.31: Effect of weld speed on SEM micrograph of fractured tensile specimen

4.6 Optimization of 316L SS Weld joint using Taguchi's approach

In a similar way, for 316L SS steel, DOE analysis proved to be more economical through the minimization of the number of experiments. 316L SS being costlier with respect to A572 steel, as it contains Cr, Ni, Mo as major elements along with other elements. Prediction of the most influential parameters needs to be carefully addressed during experimentation for desired output. The levels of welding parameters for 316L SS steel for full penetration welded joints and minimum spatter quantity have been finalized through preliminary experiments. Results of preliminary experiments showed much lower penetration at lower current values less than 90 A, as shown in Figure 3.5(d-e). High current values caused excessive piling of weld metal and low penetration and adversely affected the HAZ. SS welds also showed coloured heat tint indicating segregation of alloys in the HAZ zone, so it was more challenging to weld stainless steel with respect to A572 alloy. If weld speeds were too high, then again, lack of penetration was observed, as shown in Figure 3.5(e). Lower shielding gas below 10 l/min proved to be insufficient in protecting the weld bead causing severe oxidation and defects. So during the experiment, joints were inspected for a spatter-free smooth appearance, lower tint colour and absence of any surface defects (like surface porosity, undercut etc.) and full penetration.

Taguchi's robust design approach was used to generate the L_{16} orthogonal array for 3-factors and 4-levels of Input variables/factors to perform experimentation. Their corresponding levels, UTS, YS and HI for all 16 welded samples, have been calculated using Equation 4.1 and tabulated in Table no. 5.1. HI varied from 2.71 kJ/cm (minimum for S04) to 21.28 kJ/mm (maximum for S16), which is well within the recommended HI for best impact properties. UTS varied from a minimum of 466 MPa (Sample S03) to a maximum of 535 MPa (Sample S09). Main effect plots and S/N plots were used for

finding the optimum process parameters.

Table 5.1: L_{16} orthogonal array and corresponding levels and obtained Average Ultimate Tensile strength (UTS), Yield stress (YS) and Heat inputs (HI)

Sample No. (Exp. No.)	**Current** (Amp)	**Gas flow rate** (l/min)	**Weld Speed** (mm/sec)	**Heat Input** (kJ/cm)	**Yield Stress** (MPa)	**Ultimate Tensile Strength** (MPa)
S01	95	10	1.5	8.51	228	500
S02	95	13	2.0	5.43	230	480
S03	95	16	2.5	3.51	227	476
S04	95	19	3.0	2.71	215	466
S05	120	10	2.0	6.85	255	511
S06	120	13	1.5	11.76	230	489
S07	120	16	3.0	3.63	260	499
S08	120	19	2.5	4.84	270	520
S09	**145**	**10**	**2.5**	**5.68**	**273**	**535**
S10	145	13	3.0	4.38	275	525
S11	145	16	1.5	15.43	255	493
S12	145	19	2.5	8.77	265	512
S13	170	10	3.0	6.06	256	520
S14	170	13	2.5	8.51	250	505
S15	170	16	2.5	12.45	247	501
S16	170	19	1.5	21.28	240	495

4.6.1 Evaluation of Signal to Noise (S/N) Ratio

Taguchi method was again used to generate S/N plots and main effect plots for 316L SS and find the variability of parameters along with optimum parameters. “Larger is better” for YS and UTS were selected for analysis, while for HI, the “Smaller is better” criteria was selected. DOE experimentation was carried out, and the S/N plot and main effect plots were shown in Figures 5.1 and 5.2.

The “Larger the better” criteria were used to generate response for Signal to Noise ratios along with response for means to find the effects and contribution of different factor levels on UTS and YS and have been tabulated in Table 5.2. The results concluded that current and weld speed showed considerable variation around the mean with respect to gas flow rate.

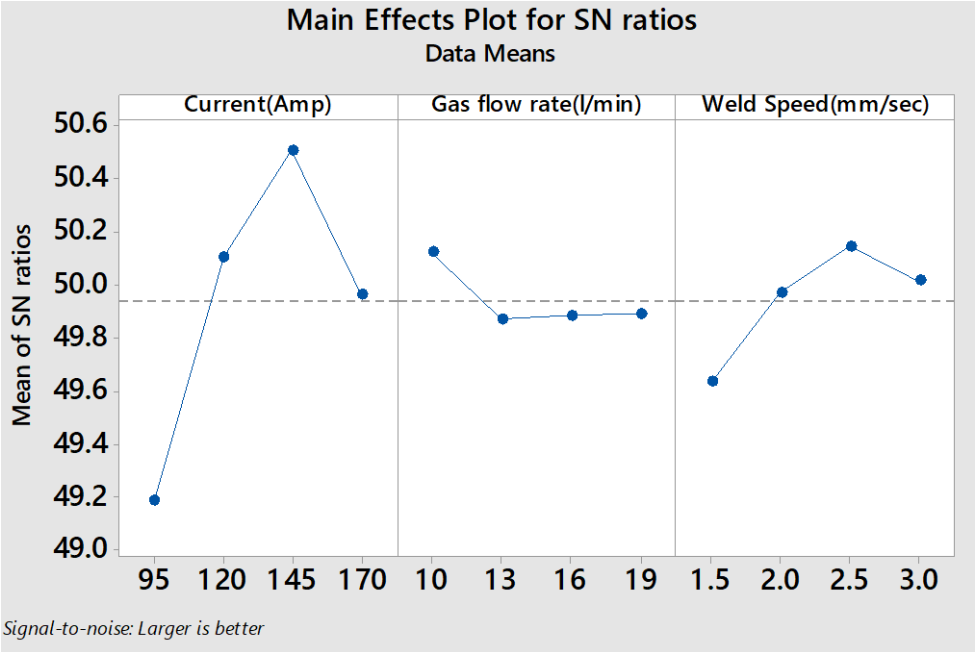

Figure 5.1: Main effect plot for S/N ratio

Finally, to confirm the optimum parameters, the results of the main effect plot, as shown in Figure 5.2 and Table 5.2, were analyzed.

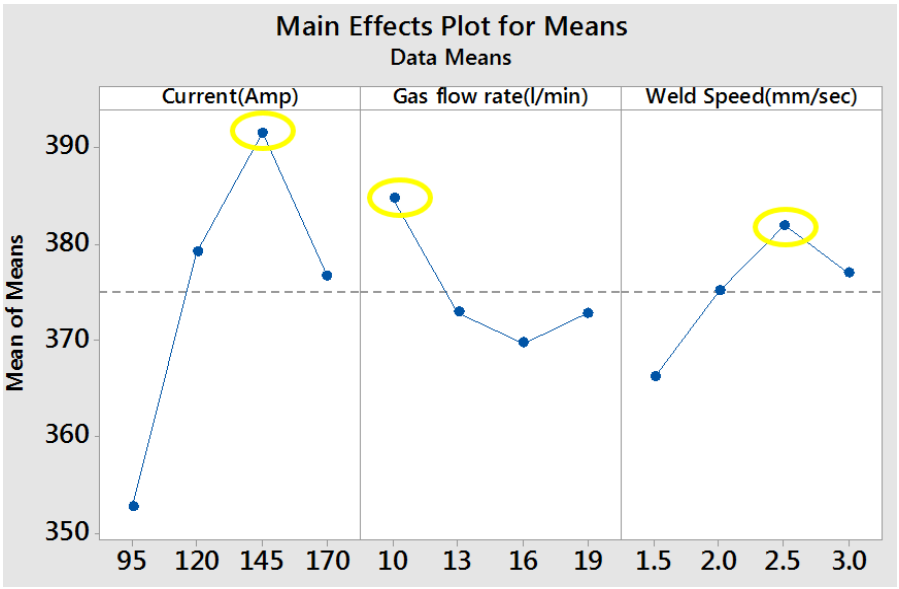

Figure 5.2: Main effect plot of means

The Main effects plot indicates the optimum parameter, and the optimum levers have been encircled in Figure 5.2. From the graph in Figure 5.2, the optimum parameters for larger the better criteria were Current: 145 A, weld speed: 2.5 mm/sec and gas flow rate of 10 l/min encircled in yellow.

Table 5.2: Taguchi Analysis: UTS versus Current, gas flow rate, weld speed

Response for Signal to Noise Ratios "Larger is better"				Response for Means		
Level	Welding Current	Gas flow rate	Welding speed	Welding Current	Gas flow rate	Welding speed
1	49.19	50.12	49.63	352.8	384.8	366.3
2	50.10	49.87	49.97	379.3	373.0	375.1
3	50.51	49.88	50.15	391.6	369.8	382.0
4	19.97	49.89	50.02	376.8	372.9	377.0
Delta	1.32	0.25	0.51	38.9	15.0	15.8
Rank	1	3	2	1	3	2

Through the analysis of UTS and YS results from Table 5.2, it was deduced that the current is the most influential parameter (Ranked 1) followed by weld speed (Ranked 2) and gas flow rate (Ranked 3) and was also indicated by ANOVA analysis. Strength increased with an increase of current due to an increase in penetration and removal of inclusions. An increase in weld speed initially increased strength as higher penetration and lesser grain coarsening occurred at HAZ, while further increase caused loss of alloying elements resulting in a decrease in strength along with lower dilution as in current of 95 A at higher weld speeds also revealed from macro graphs (For S02). Further increase in current caused serious grain coarsening, causing a decrease in strength further. Individual plots were also plotted using "Larger is better" for UTS, YS and "Smaller is better" for HI are shown in Figures 5.3, 5.4 and 5.5, respectively.

The individual main effect plot of UTS (Figure 5.3) shown similar behaviour, i.e. increase in mean strength was observed up to the third level followed by a decrease. For gas flow rate, mean strength decreased and was found to be lowest for 16 l/min flow rate. For yield stress (Figure 5.4) similar behaviour was concluded with 145 A current, 10 l/min and 2.5 mm/sec shown the highest yield strength.

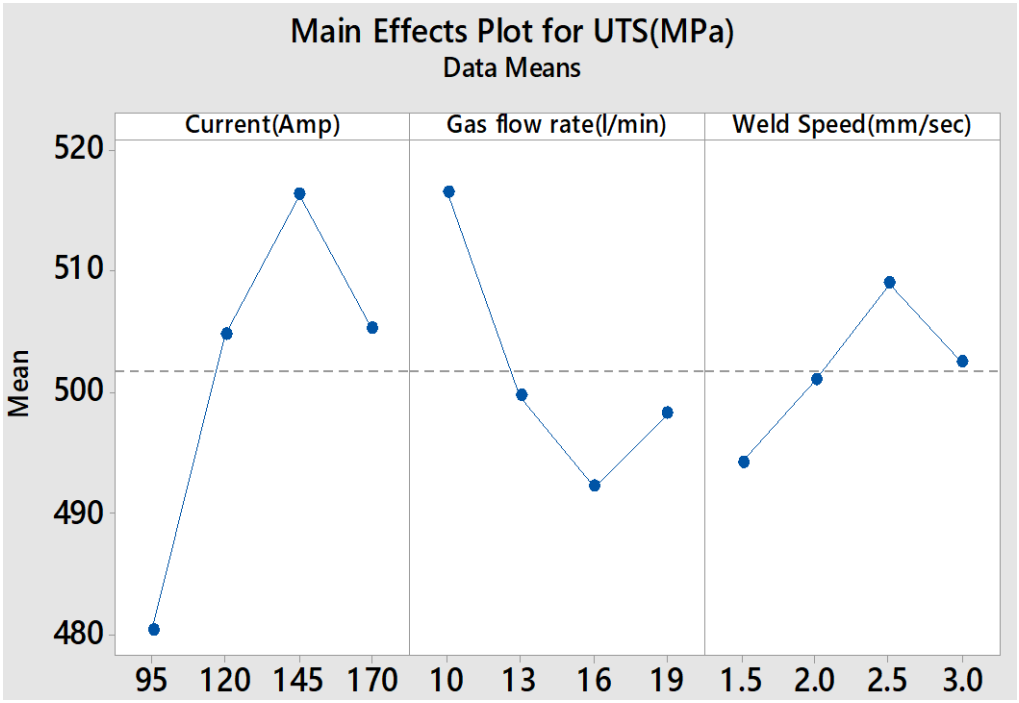

Figure 5.3: Taguchi Analysis: UTS Vs Current, Gas flow rate and weld speed

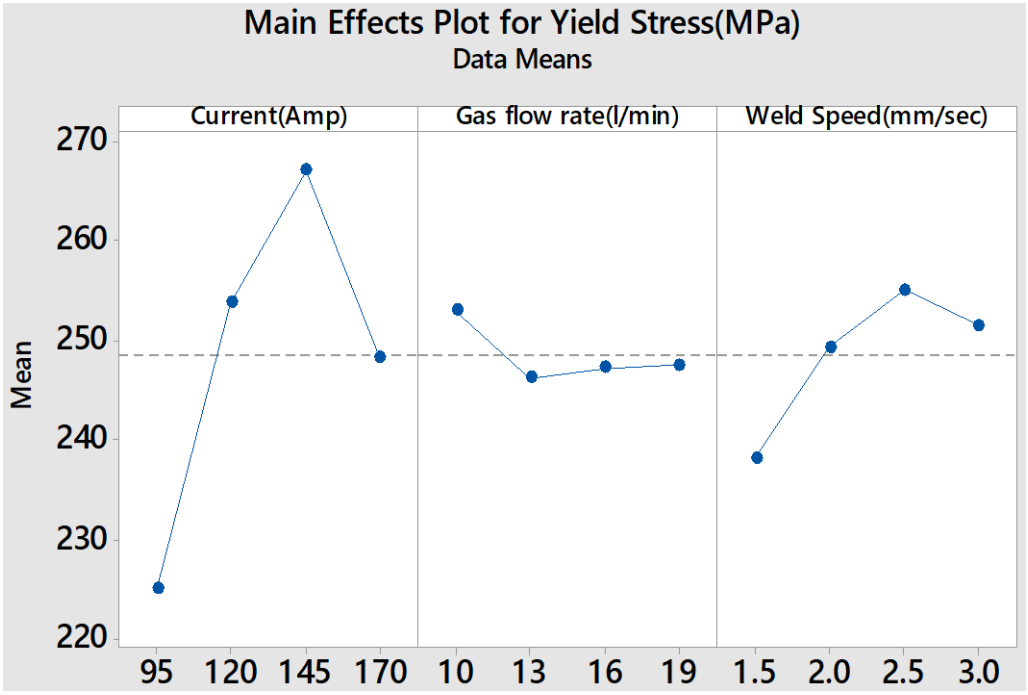

Figure 5.4: Taguchi Analysis: YS Vs Current, Gas flow rate and weld speed

It can be seen from Figure 5.5, showing the main effect plot of Heat input Vs other parameters, increased almost linearly with Current and Gas flow rate that increases in weld speed caused a decrease in Heat input as HI is proportional to current. It decreases with an increase in welding speed.

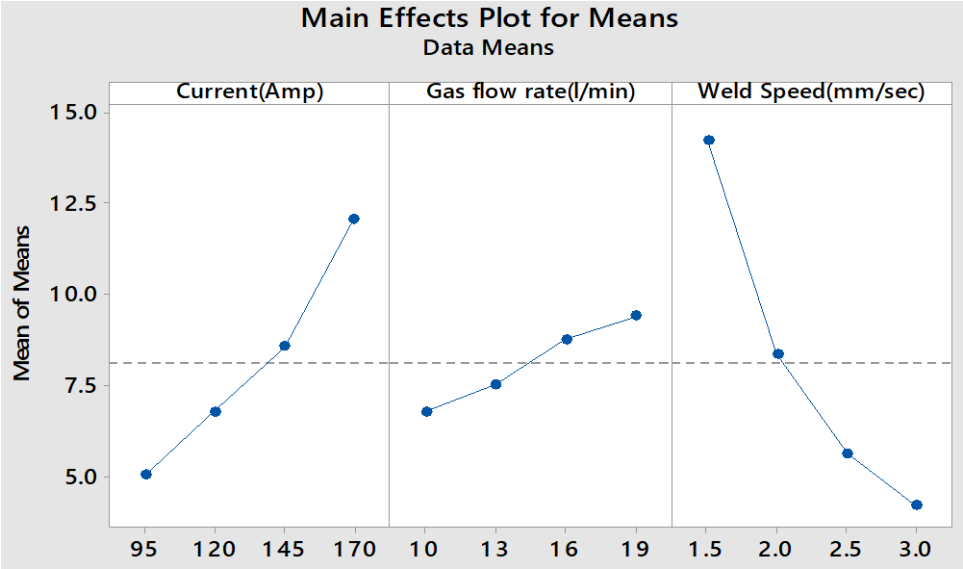

Figure 5.5: Taguchi Analysis: HI Vs Current(A), Gas flow rate(l/min) and weld speed(mm/sec)

4.6.2 Analysis of Variance (ANOVA)

ANOVA was applied to find the percentage contribution of each factor. The detailed ANOVA result for the output responses has been tabulated in Table 5.3

Table 5.3: Analysis of Variance for UTS, using Adjusted SS for Tests

Source	DF	Seq SS	Adj SS	Adj MS	F	P	%age contribution
Current	3	3170.2	3170.2	1056.7	9.65	0.01	65.10
Gas flow rate	3	518.2	518.2	172.7	1.58	0.290	10.64
Welding speed	3	524.4	524.4	174.8	1.60	0.286	10.77
Error	6	656.8	656.8	109.5			
Total	15	4869.6					

It was concluded from ANOVA analysis that various parameters contributed differently. The calculated percentage contribution indicates the valuable parameter needs to be analyzed carefully. Current contributed the most, 65.10%, followed by weld speed of 10.77% and gas flow rate of 10.64%. Optimum process parameters were analyzed through the main effect plot and are encircled in yellow in Figure 5.2. Sample S09, with welding parameters of 145 A current, 10 l/min gas flow rate, and 2.5 mm/sec welding speed, were the optimum parameters for welding 316L SS steel. Taguchi's results have been verified through the microstructural changes and hardness patterns which will be

discussed later. Interaction plots have been used to correlate the various input parameters and show the relationship among the parameters for each level. Based on the results, the interaction effect of the factors influencing weld characteristics has been generated. The interaction effect of current, weld speed and gas flow rate on UTS, YS and HI have been shown in Figures 5.6, 5.7 and 5.8, respectively.

From the interaction plot for Ultimate Tensile Strength (Figure 5.6 b), it can be observed that UTS Increased with current from 120 A to 170 A, followed by a decrease in strength due to an increase in dilution and removal of impurities at higher heat input. For lower levels of current (95 A), UTS decreased with an increase in weld speed, as much needed heat for better dilution was available in less quantity, causing lack of fusion and low penetration defects resulting in lower strength levels. For a higher level of current 120-170 A, an Increase in weld speed caused an increase in UTS followed by a decrease of UTS as weld speed increases caused lower heat imparted to weld pool available for HAZ generation along with reduced peak temperature achieved and lower grain coarsening effect. Downward variation in UTS was observed for the highest gas flow rate

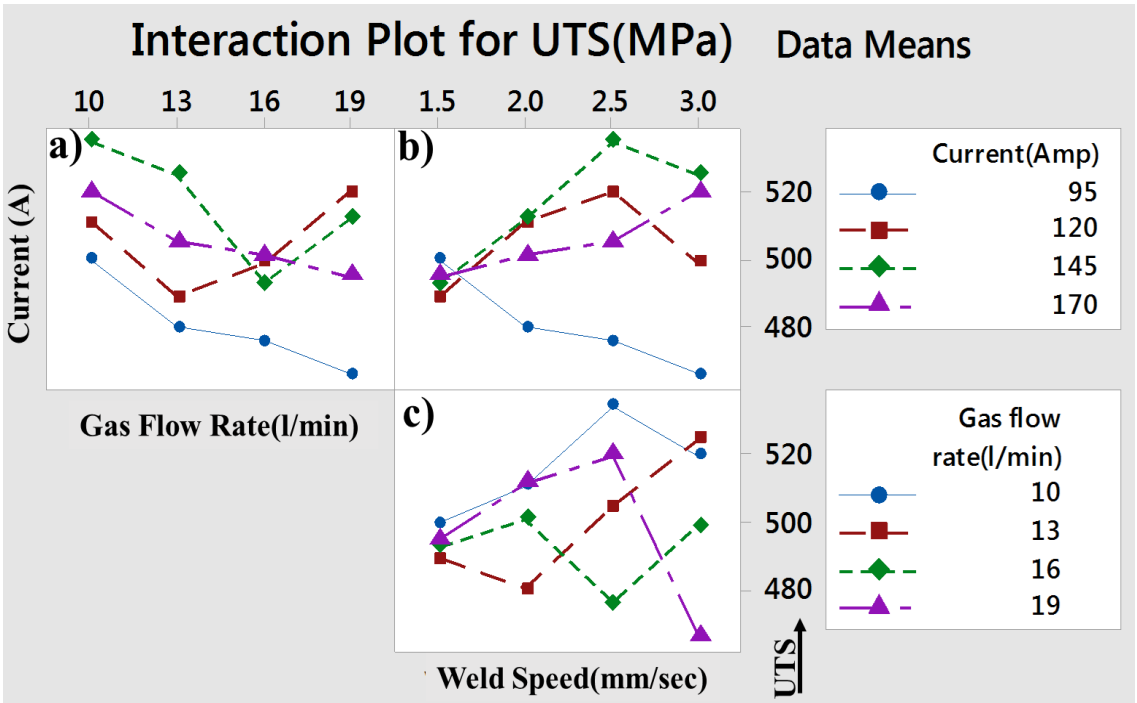

Figure 5.6: The interaction plot for Ultimate Tensile Strength (UTS)

(19 l/min) due to excessive turbulence caused at higher gas flow rates. From Figure 5.6(c), conclusive results cannot be deduced while 10 l/min gas flow rate at 2.5 mm/sec weld speed showed maximum strength.

From the interaction plot for Heat Input (Figure 5.7), it can be found that with an increase in weld speed, there is a decrease in heat input, and considerable variation in HI was observed due to current. For lower values of current with an increase in gas flow rate, there has been a decrease in heat input.

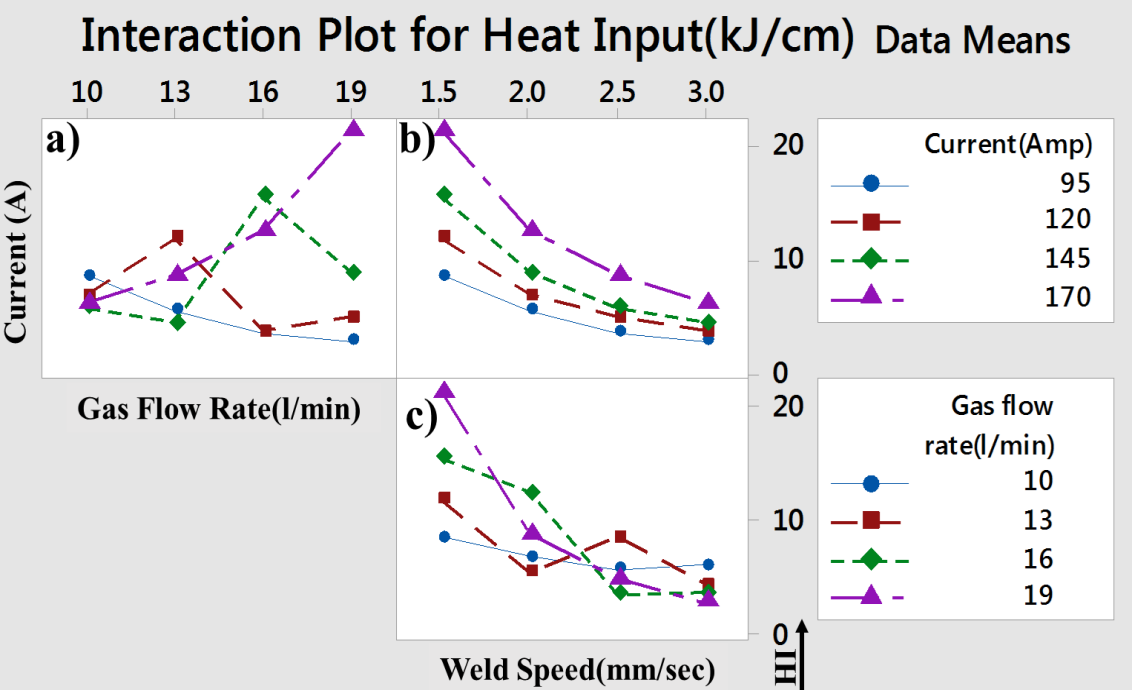

Figure 5.7: The interaction plot for Heat Input

From the interaction plot for YS from Figure 5.8, it can be concluded that YS increased initially with increasing weld speed followed by a decrease due to lesser grain coarsening effect pertaining to lower heat input at higher weld speeds. A decrease in YS was also observed for an increase in gas flow rate. YS increased with weld speed for most of the gas flow rates and decreased for higher weld speed and current.

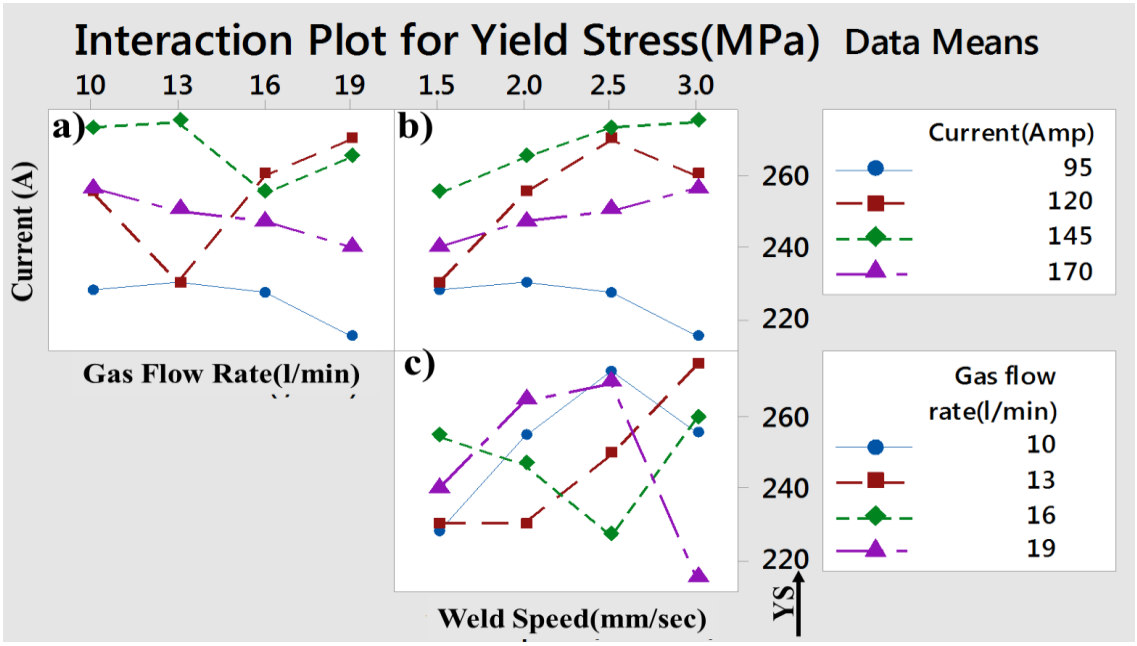

Figure 5.8: The interaction plot for Yield Stress

4.7 Effect of Heat Input on 316L SS Weld joint

Heat input plays a significant role in defining the peak temperature reached and heat tint generated in and around the weld pool, i.e. the Heat affected zone. The interaction plot for Heat input is shown in Figure 5.8. The bar chart shown in Figure 5.9 shows the variation of HI for all samples.

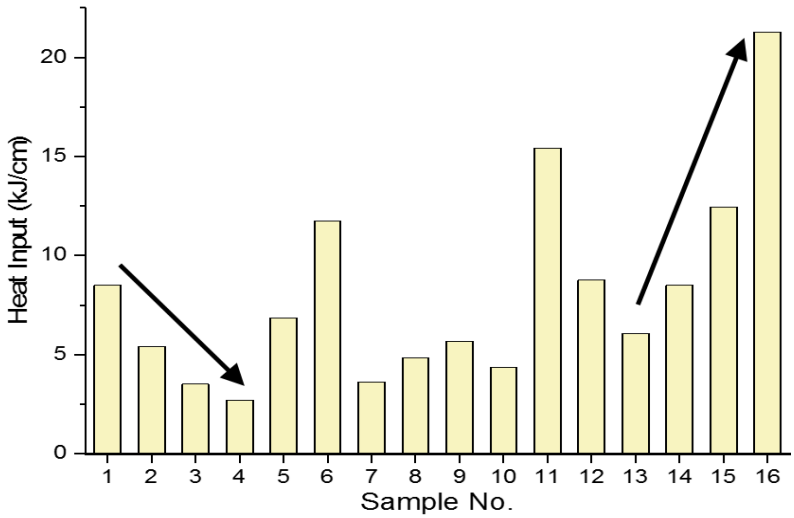

Figure 5.9: The bar chart for Heat Input

From Table 5.1, it can be found that HI varied from 2.71 kJ/cm (minimum) to 21.28 kJ/cm (maximum). Samples S01, S06, S11 and S16 possessed the highest HI values for all current levels. From the bar chart, it can be concluded that for samples S01 to S04,

HI decreased while for S13 to S16, its nature is increasing. It can also be deduced from the bar chart and table 5.1 that heat input levels around 6 kJ/cm (S01, S5, S08, S09, S12 and S13) possessed higher UTS and YS values while heat inputs around 20 kJ/cm had lower UTS and YS which might be due to higher grain coarsening effects in HAZ. HI for the welded specimens with optimum parameters was 5.68 kJ/cm. A higher amount of heat available in HAZ results in an overall increase in peak temperature. A higher temperature gradient leads to a higher cooling rate and wider HAZ. The increase in the heat input leads to an increase in the fusion zone and HAZ dimensions and increases δ ferrite volume fraction. Higher heat cycles may result in considerable migration of ferrite stabilizers (Cr and Mo) from weld Metal to HAZ, causing an increased volume fraction of δ ferrite. Increased δ ferrite would restrict the grain growth, minimize the cracking tendency and increase the UTS and YS [191]. The contribution of 21 kJ/cm showed the highest volumetric fraction of δ ferrite that, along with excessive grain growth in HAZ may deteriorate the properties of HAZ. Similar results were found by **Demarque et al.** [71]. **Vitek et al.** [192] found similar results, as with an increase in δ ferrite for the cooling rate increase from 1 to 7 K/s followed by a decrease after reaching the highest value at 5 K/s. It indicates that the ferrite content and strength in weld joints can vary depending on welding conditions and the welding parameters. The heat inputs of 5.68 kJ/mm and 6.06 kJ/mm provided the best combined results with higher strength values and lower heat input levels. Furthermore, the dimensions and areas of the zones indicated that the welded joints are suitable for these heat inputs.

4.8 Macrostructural evaluations of 316L SS Weld joint

The macrostructural view provides information about the quality of weld joints in terms of macro-cracks, porosity, blow holes, weld speed levels and sometimes the peak temperature reached in the HAZ through colour tint for stainless steels. Also, it conveys

the reinforcement quantity, dilution and any kind of lack of fusion, undercuts and discontinuities. From the micrograph shown in Table 5.4, it can be concluded that samples S02, S03, S04 showed low penetration, and sample S04 showed a lack of fusion under the bead with an increase in weld speed, as sufficient heat was not available for requisite dilution. Upon further increase in current and HI, full penetration was achieved for the remaining samples. Sample S01, S05, S06, S07, S08, S09, S10, S12 and S13 were well under prescribed ratios of bead width to depth which should be 1:2 as per TWI. For higher heat input, high current and lower weld speeds, the excessive reinforcement increased the HAZ size. A decrease in toe angle and bead height was found with an increase in weld speed and decreasing heat input. Ripples formed on sample S02 and heat tint generated can be seen in Figure 5.10 and the ripple structure changed from elliptical (Sample S03, S05, S06, S08, S15 and S16) to trapezoidal shape (Sample S04, S07, S10 and S13) for similar heat inputs.

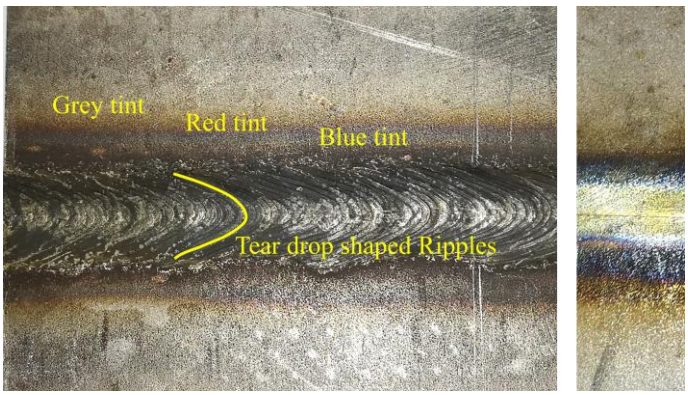

Figure 5.10: Sample S02 at weld speed 2.0 mm/sec HI of 5.43 kJ/cm

For Samples having HI around 6 kJ/cm and 10 kJ/cm like Sample S05, S08, S09, S12 and S14, the surface appearance was very good with full penetration with a very low level of spatters, indicating good bead protection. Analyzing the macrograph of sample S09, it can be observed that optimum weld current, weld speed, and gas flow rate and can give full penetration without spatter. At Higher weld speed and low current, there has been underfills. At higher current and excessive low-speed piling of filler has occurred,

causing considerably wider HAZ.

Table 5.4: Macro structure of 316L SS welded joints

Sample No.	Heat Input (kJ/cm)	Weld bead Top View	Macro Structure
1	8.51	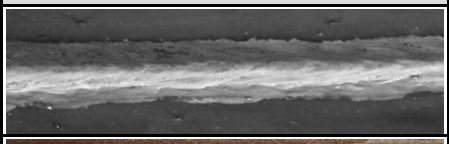	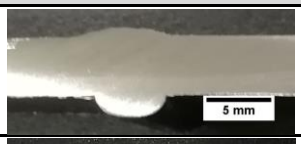
2	5.43		
3	3.51		
4	2.71	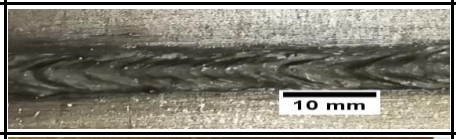	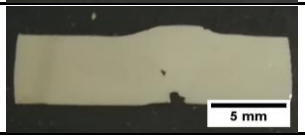
5	6.85		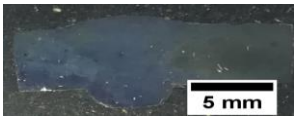
6	11.76		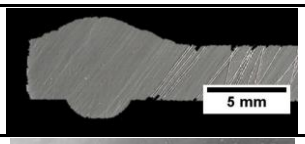
7	3.63		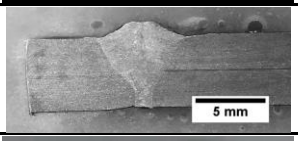
8	4.84		
9	5.68		
10	4.38		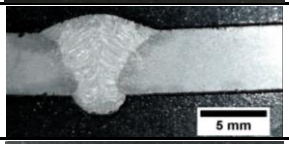
11	15.43		
12	8.77		

Sample No.	Heat Input (kJ/cm)	Weld bead Top View	Macro Structure
13	6.06	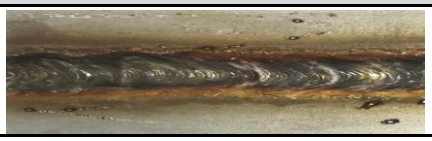	
14	8.51		
15	12.45		
16	21.28		

4.9 Microstructural evolution of 316L SS Weld joint

In austenitic stainless steels, microstructural changes which ultimately dictate the strength and morphological features in a welded structure are the chemical composition (weld bead) and thermal cycle during welding. Austenite can contain 0.15% Carbon and more or less acts as an impurity, but it increases the yield strength. Excess of carbon causes the formation of carbides around grain boundaries resulting in a Chromium (Cr) depleted zone (sensitized zone) which makes the material sensitive to corrosion. The carbide precipitation reaction occurs between 600°C and 1000°C. At similar temperatures, other intermetallic phases like sigma can precipitate at a longer duration in the heavily alloyed industrially used grades. This occurs in alloys where the matrix is rich in chromium equivalents, over 18%, and low in dissolved carbon. The investigated 316L SS (Base material) and ER-316L SS filler material contained 0.03% carbon by weight. Recrystallized austenite grains with a small amount of δ ferrite stringers can be seen from the optical micrograph of base material at 200X in Figure 5.11. The annealing twins can also be seen in 316L SS, which are its characteristic features, and the average austenitic grain size calculated was 22 μm.

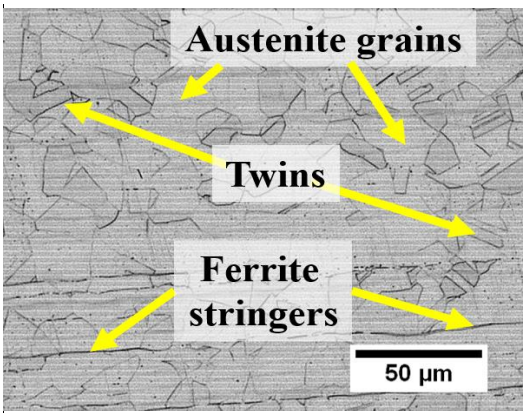

Figure 5.11: Optical micrograph of 316L stainless steel (Base material)

Microstructure dictates the structural integrity and strength behaviour of welded joints. Different heat inputs execute different thermal cycles producing a heterogeneous mixture of phases in the weld bead and HAZ. Cooling rate and loss of elements through precipitation or segregation of elements can reduce the properties (mechanical/ corrosion). The microstructure of welded joint consists of ferrite and austenite i.e. δ-ferrite structure that could be described by primary solidification modes of weld metals but in excess dictate the sensitivity to corrosion. Cr_{eq}/Ni_{eq} ratio plays an important role in explaining the metal solidification mode and heat rejected to base material forming HAZ. As per the Schaeffler diagram solidification mode, phase transformation, and phase composition depend upon the composition of alloys and following reactions may took place during solidification. To predict the mode of solidification following equations can be used where L is the liquid, δ is delta-ferrite, and γ is austenite respectively.

Austenite mode (A): $L \rightarrow (L + \gamma) \rightarrow \gamma$, $(Cr_{eq}/Ni_{eq}) < 1.25$

Austenite Ferrite mode (AF): $L \rightarrow (L+\gamma) \rightarrow (L+\gamma+\delta)(\gamma+\delta)$, $1.25 < (Cr_{eq}/Ni_{eq}) < 1.48$

Ferrite Austenite mode (FA): $L \rightarrow (L+\delta) \rightarrow (L+\delta+\gamma) \rightarrow (\gamma+\delta)$, $1.48 < (Cr_{eq}/Ni_{eq}) < 1.95$

Ferrite mode (F): $L \rightarrow (L + \delta) \rightarrow \delta \rightarrow (\gamma+\delta)$, $(Cr_{eq}/Ni_{eq}) > 1.95$

The peritectic reactions ($L + \delta = \gamma$) stimulate the formation of austenite and the partial eutectic reaction ($L = \gamma + \delta$) took place upon cooling. A partial δ ferrite is retained and the remaining liquid is transformed directly to austenite in the weld [49, 193]. Equations 2.2 and 2.3 were applied for calculation of Cr_{eq}/Ni_{eq} ratio and predicting the solidification

mode. Furthermore, the Cr_{eq}/Ni_{eq} ratio (19.64/12.90) was calculated using the chemical composition of 316L (Base material) and ER 316L (Filler) as shown in Table 3.3. For low Cr_{eq}/Ni_{eq} ratios, mode of solidification causes no change in structure after solidification as ferrite was absent. For a higher ratio, AF mode solidification occurs in which the primary phase is austenite, and the remaining liquid solidifies as intercellular ferrite. For higher Cr_{eq}/Ni_{eq} ratios during FA and F mode solidification, the high-temperature microstructure contains 70 to 100% ferrite. Upon reduction of temperatures, most of the ferrite transforms, and the residual ferrite left behind in the Cr-rich dendritic cores depicts a characteristic vermicular ferrite structure. These structures are formed due to diffusional transformation at high temperatures (1373-1573 K) under normal arc welding. Due to sluggish transformation kinetics, elongated acicular and Widmanstetten type morphologies are promoted.

In the current study, the Cr_{eq}/Ni_{eq} ratio base material and filler was 1.53. This was found to match with the ferrite-austenite mode (FA); therefore, the solidification mode is Ferritic-Austenitic mode (FA) as $1.48 \leq Cr_{eq}/Ni_{eq} \leq 1.95$. The cooling rate is the most contributing factor that contributes to attaining different morphologies. Slow cooling

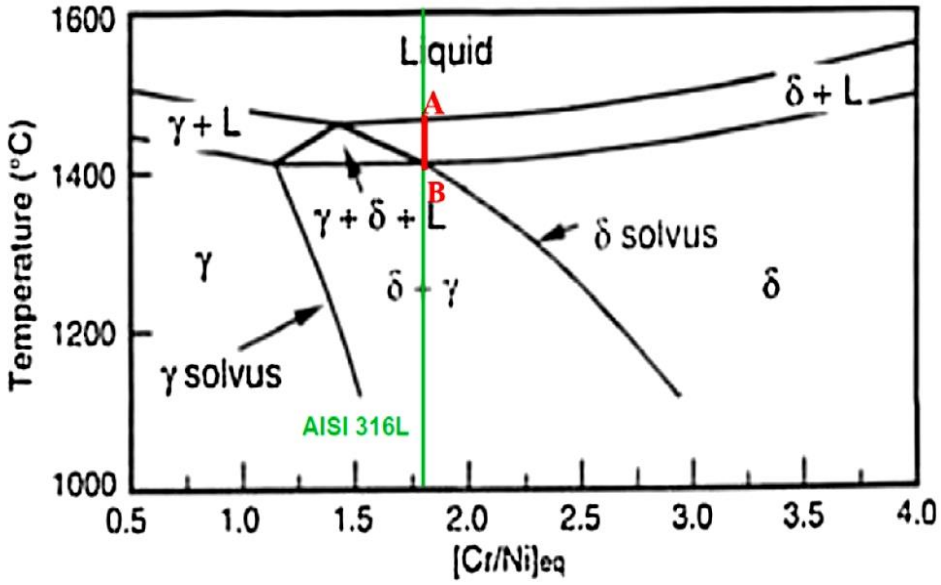

Figure 5.12: Pseudo-binary diagram of the Fe [Cr–Ni]eq for AISI 316L. Reproduced with permission from Ref. [71]. Copyright (2018) Elsevier

transforms the austenitic grains into more complex pearlite and even martensite. Figure 5.12 shows the binary phase transformation diagram of the 316L steel. The highlighted straight segment A-B line in red shows the region of δ ferrite formation during cooling [49, 71]. Being a diffusional reaction, the formation of the ferrite depends on the cooling time, so the longer the material remains in this area the greater would be the proportion of δ ferrite generated as per **Ronqueti et al.** [194].

Various characteristics zones in GMAW welded 316L SS joint are Fusion Zone(FZ), Unmixed zone(UMZ) and Heat affected zone (HAZ), and Base metal (BM) is clearly visible from the micrograph Figure 5.13(a-b) (Sample S12).

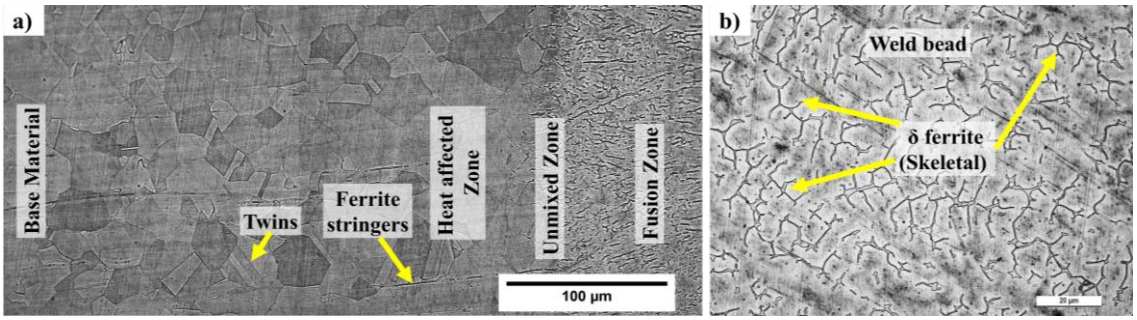

Figure 5.13: Optical micrograph of Zones in welded joints a) Sample no S12 (200X), b) Weld bead morphology (1000X)

The HAZ of AISI 316L austenitic stainless steels contains δ ferrite and γ austenite grains. In addition, the transition zone/ unmixed zone between the fusion zone and HAZ is mainly differentiated by the δ ferrite morphology. HAZ possess an altered grain structure, but some localized grain growth is expected due to heat conduction in all directions increasing the average grain size in FZ and reduced while moving away from the weld center. In 316L stainless steel, there exists an unmixed Zone (UMZ), which is an area that significantly affects the mechanical properties of the welded joints [195]. This area is visibly seen in almost all samples. Due to the higher temperature and low thermal conductivity of 316L steels close to the molten pool, an improper mix of molten filler and BM exists. No meaningful microstructural evolution is occurring and is

characterized through δ ferrite morphology. The effect of various parameters has been analyzed separately.

4.9.1 Effect of Heat input

Different zones of welded joint for 316L SS has been shown in Figures 5.14, 5.15, 5.16, 5.17 and 5.19 for sample S02, S05, S12, S16 and S09 respectively. Microstructure depicted austenite matrix and various δ ferrite morphologies in FZ, transition Zone (UMZ), heat affected zone and ferrite in the form of stringers in BM.

HI varied from 2.7 kJ/cm to 21.28 kJ/cm, and for optimum sample according to DOE experimentation, was 5.68 kJ/cm (for S09). Increasing HI increased the penetration. From Figure 5.4, we can see, there was a lack of fusion inside the weld bead (in S04), and upon increasing HI, full penetration was obtained for S09 (5.68 kJ/cm), S05 (8.77 kJ/cm), S12 (8.77 kJ/cm), S16 (21.28 kJ/cm). An increase in HI caused the increase in HAZ width from 40 µm (for S02) to 289 µm (for S16) as higher HI increased the peak temperature in the weld. CO_2 addition with Ar improved the stability of the process through the increase in flow-ability of molten filler wire along with an increase in inclusions and carbide in the form of fine particles in WB, as shown in micrographs in Figure 5.15. As higher heat cycles are required for austenite to ferrite transformation high, HI resulted in more ferrite stringers in HAZ. δ ferrite would restrict the grain growth and HAZ liquation cracking. During the cooling process, at low HI, the δ ferrite volume percentage was low (7% in S02) while it increased up to 12% (for S15) with increased HI.

An increase in HI changed the ferrite morphology from thinner dendrite with smaller dendrite spacing (at HI- 5.43 kJ/cm for S02) to thick dendrite with larger spacing (at HI- 21.28kJ/cm for S16) as shown in Figure 5.14 and 5.17, respectively. Higher HI gives rise to the greater spacing between δ-ferrites because greater inputs imply lower cooling rates. Therefore, during solidification, the austenite dendrites will have more time

to grow, consequently increasing the spacing between the δ-ferrites, which are mostly found in the austenite contours [196].

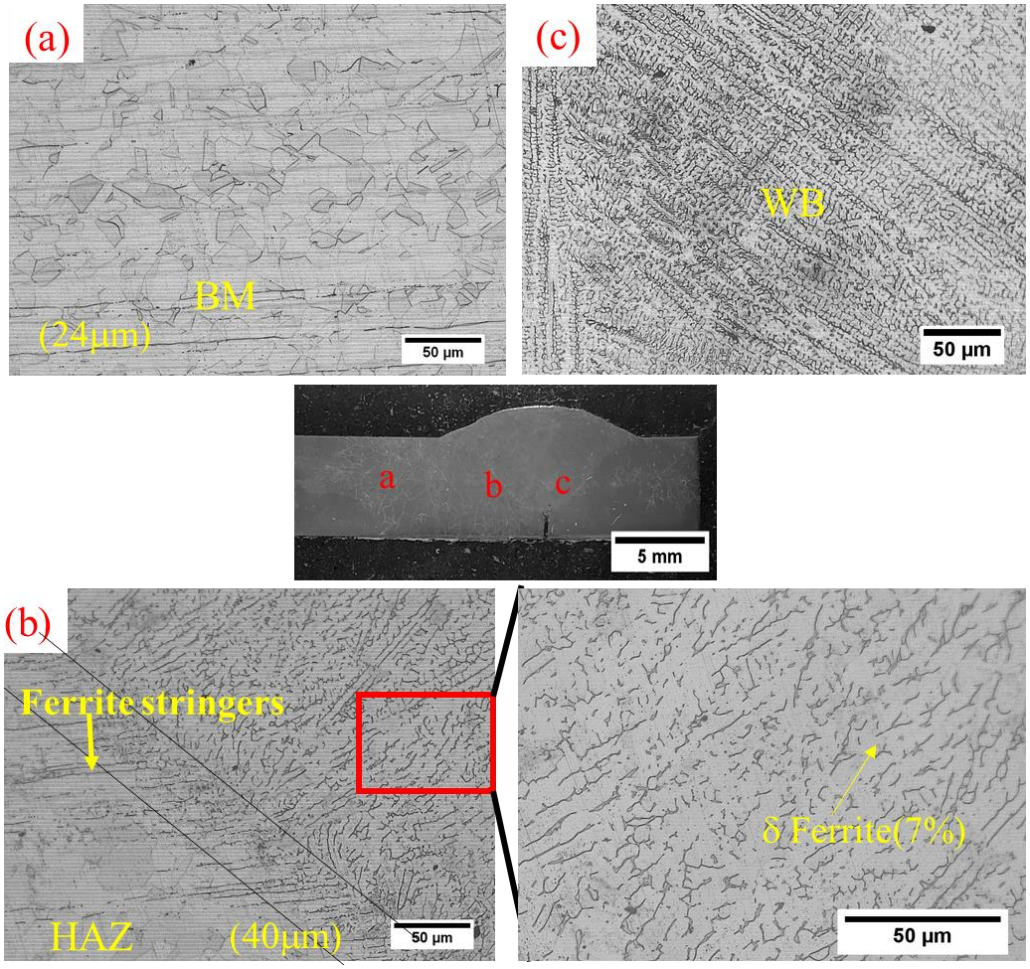

Figure 5.14: Optical micrograph of Sample S02 at 200X: Heat Input- 5.43 kJ/cm, Current- 95 A, HAZ Width- 40 µm

From Figure 5.15, it can be seen that the skeletal morphology of ferrite has changed to lathy structure in Figure 5.19 due to restricted diffusion during ferrite to austenite transformation. Low heat input and high cooling rate increase the fraction of δ ferrite with considerable influence on YS. Smaller dendrite size and lesser interdendritic spacing was observed (for S02) at low HI, while for high input welds like Sample S16 large interdendritic spacing was observed.

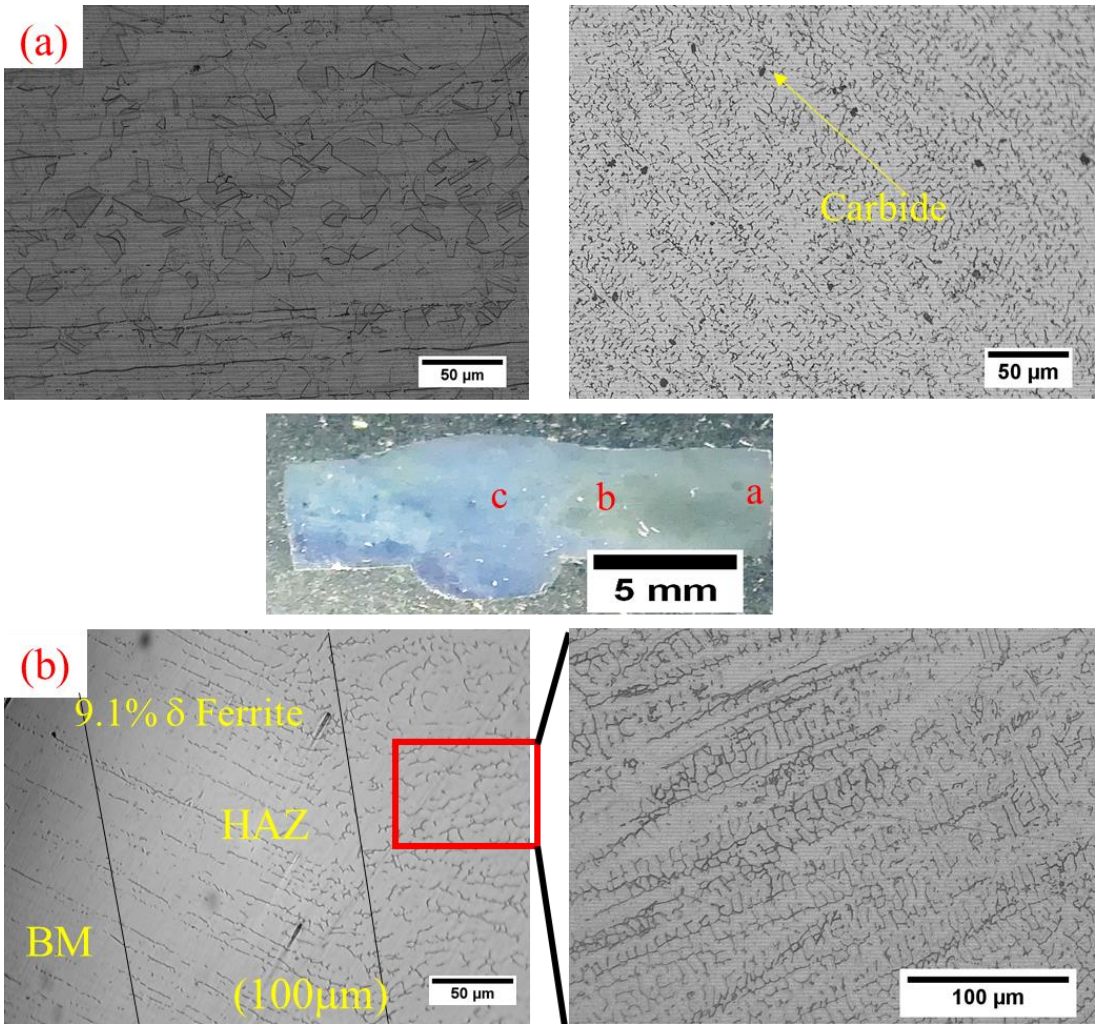

Figure 5.15: Optical micrograph of Sample S05 at 200X: Heat Input: 6.85 kJ/cm, Current- 120 A, HAZ Width- 100 µm

For sample welded at optimum welding parameters according to Taguchi analysis, i.e. Sample S09 as shown in Figure 5.19 depicts skeletal morphology of δ ferrite having the proportion of 6.5% in the weld bead having highest UTS values. δ Ferrite of 8.5% in the HAZ reduced the grain coarsening effect and ultimately increased the strength. It can be seen that vermicular ferrite was more discontinuous at a low volume of δ-ferrite content in the weld metal than at a high HI level. It was observed that the dendrite length and inter-dendrite spacing decreased when lowering the heat input levels.

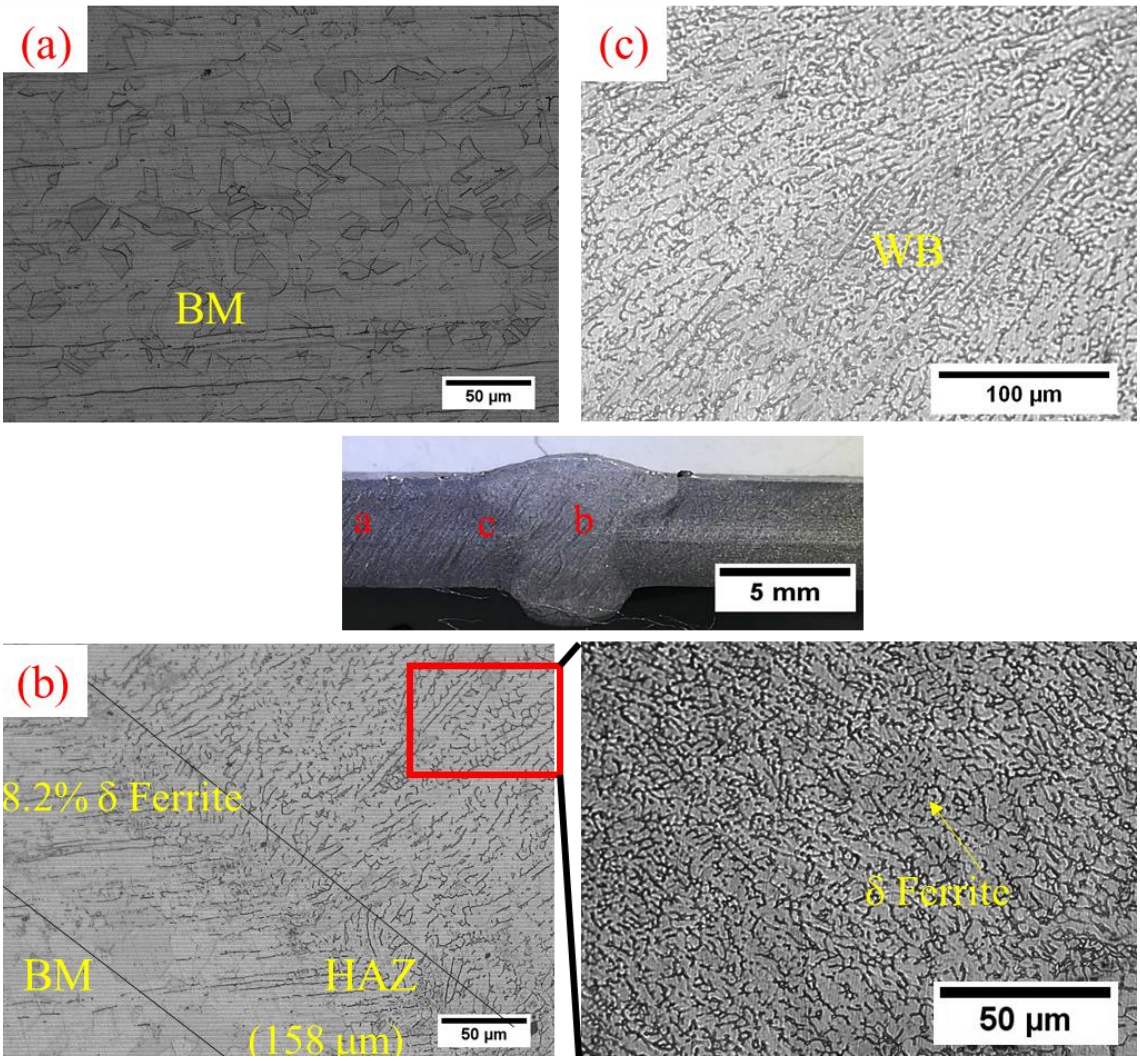

Figure 5.16: Optical micrograph of Sample S12 at 200X: Heat Input- 8.77 kJ/cm, Current- 145 A, HAZ Width- 158 µm

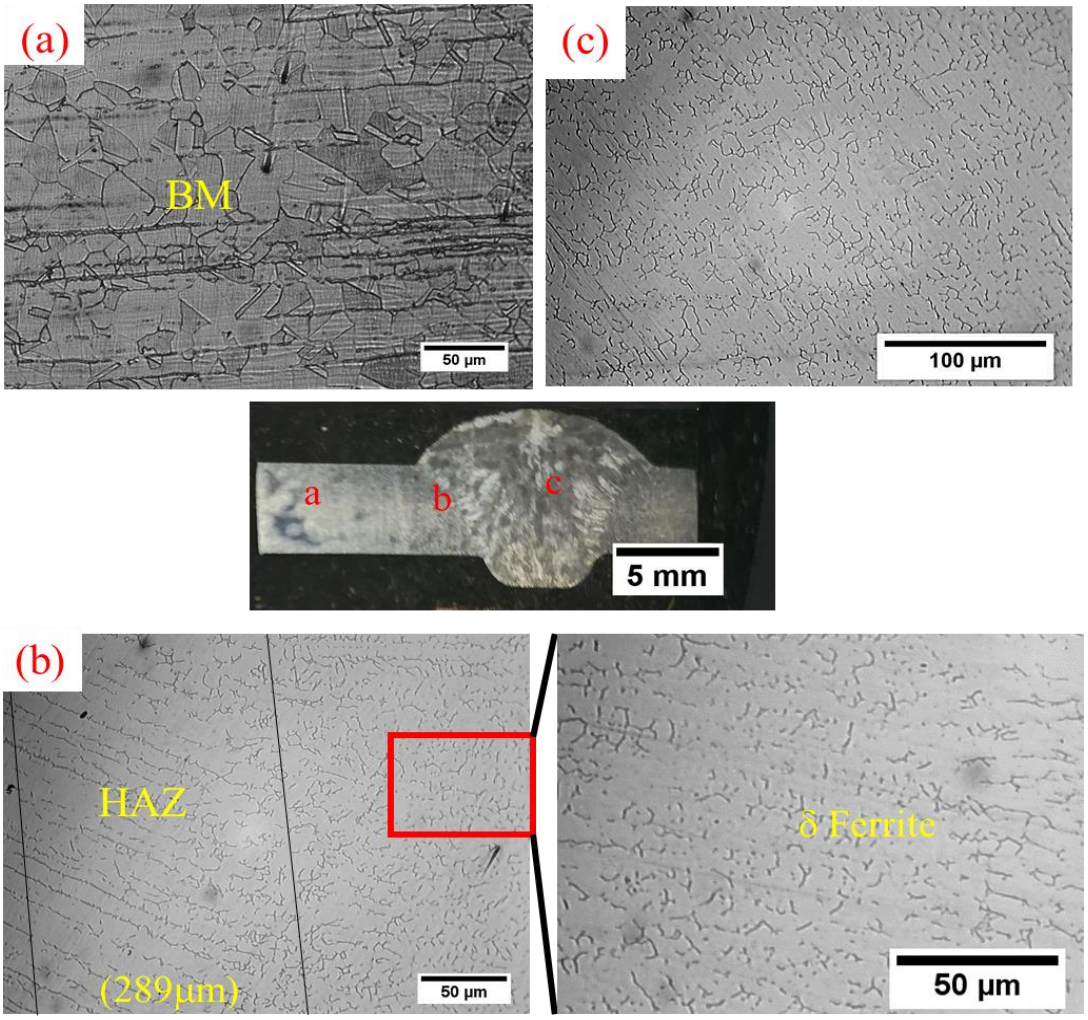

Figure 5.17: Optical micrograph of Sample S02 at 200X: Heat Input- 21.28 kJ/cm, Current- 170 A, HAZ Width- 289 µm

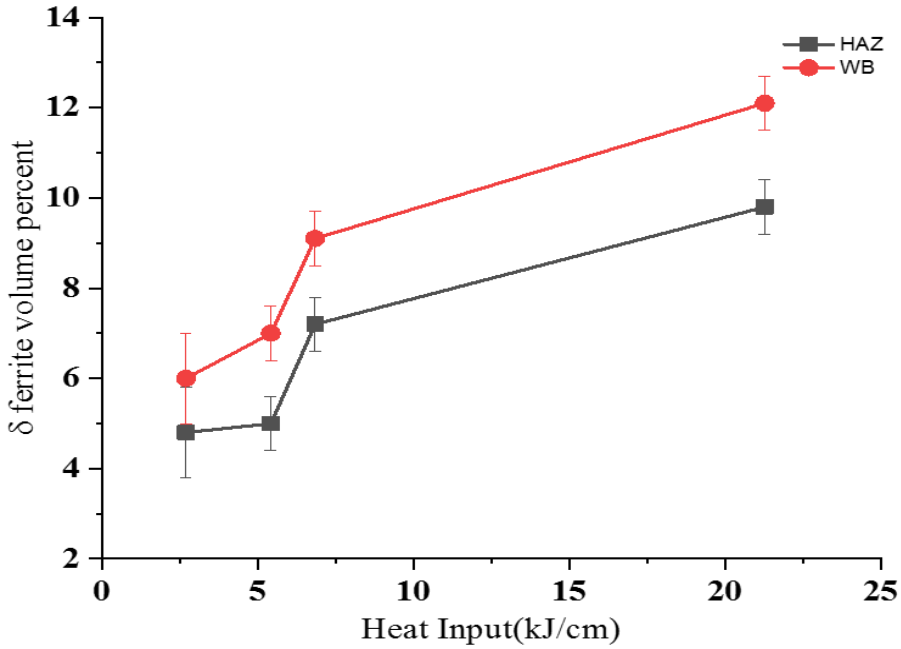

Figure 5.18: HI effect on δ ferrite content for sample S04 (2.71kJ/cm), S02 (5.43 kJ/cm), S05 (6.85 kJ/cm) and S16 (21.28 kJ/cm)

Figure 5.18 shows an increase in δ-ferrite volume percent increase from ~5% to ~ 12% with increase in heat input from 2.71 kJ/cm to 22.28 kJ/cm in weld bead and HAZ. Increase in ferrite content degrades the corrosion resistance in HAZ area.

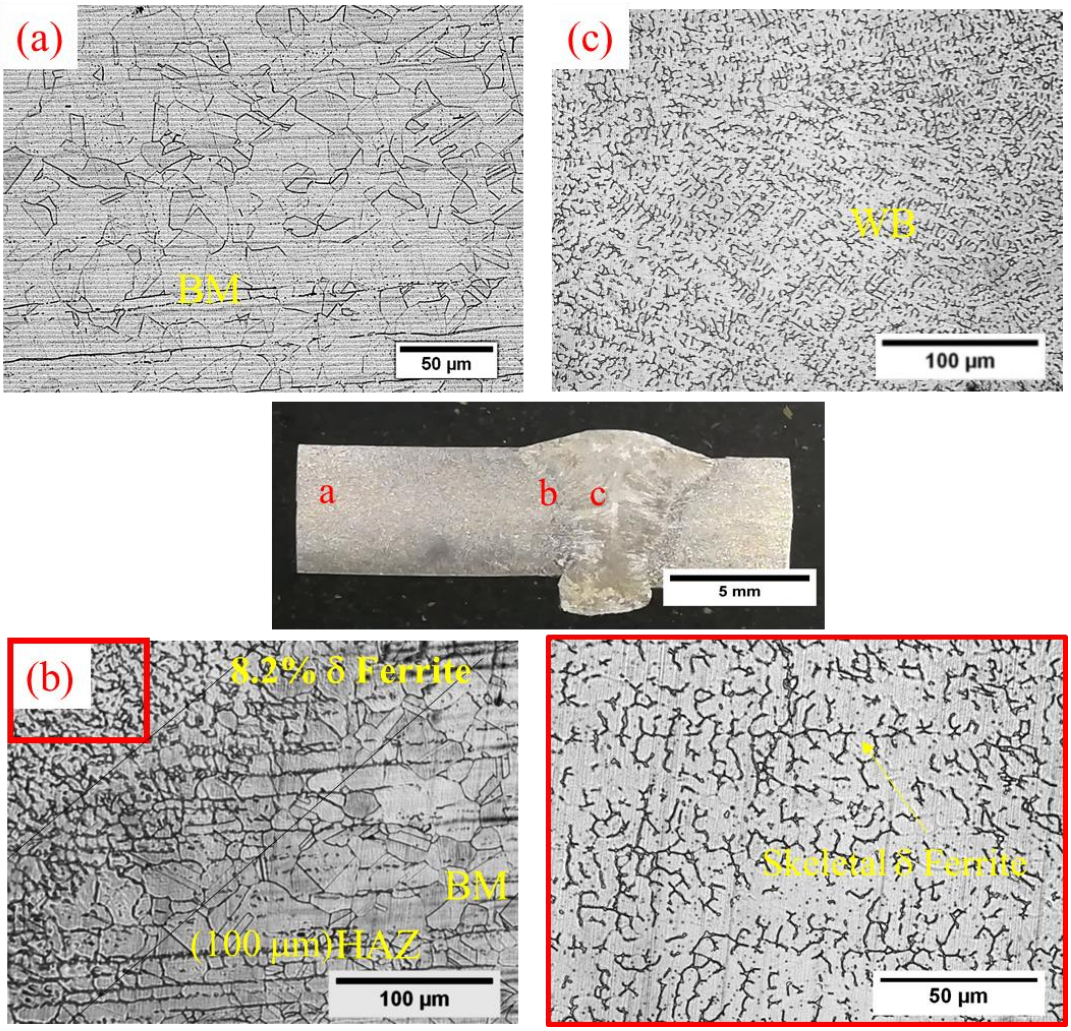

Figure 5.19: Optical micrograph of Sample S09 at 200X and 1000X: Heat Input- 5.68 kJ/cm, Current- 145 A, HAZ Width- 100 µm

Grain size in HAZ is directly related to the heat imparted during welding, and an increase in HI retards the cooling rate and increases grain size in HAZ due to more time available for grain growth. Grain coarsening and precipitation providing the pinning effect can restrict the grain coarsening effect and grain size distribution in HAZ.

4.9.2 Effect of Welding current

The effect of welding current on microstructure morphology can be seen in Figure 5.20. The Figure shows the grain size variation in the weld bead and heat-affected zone,

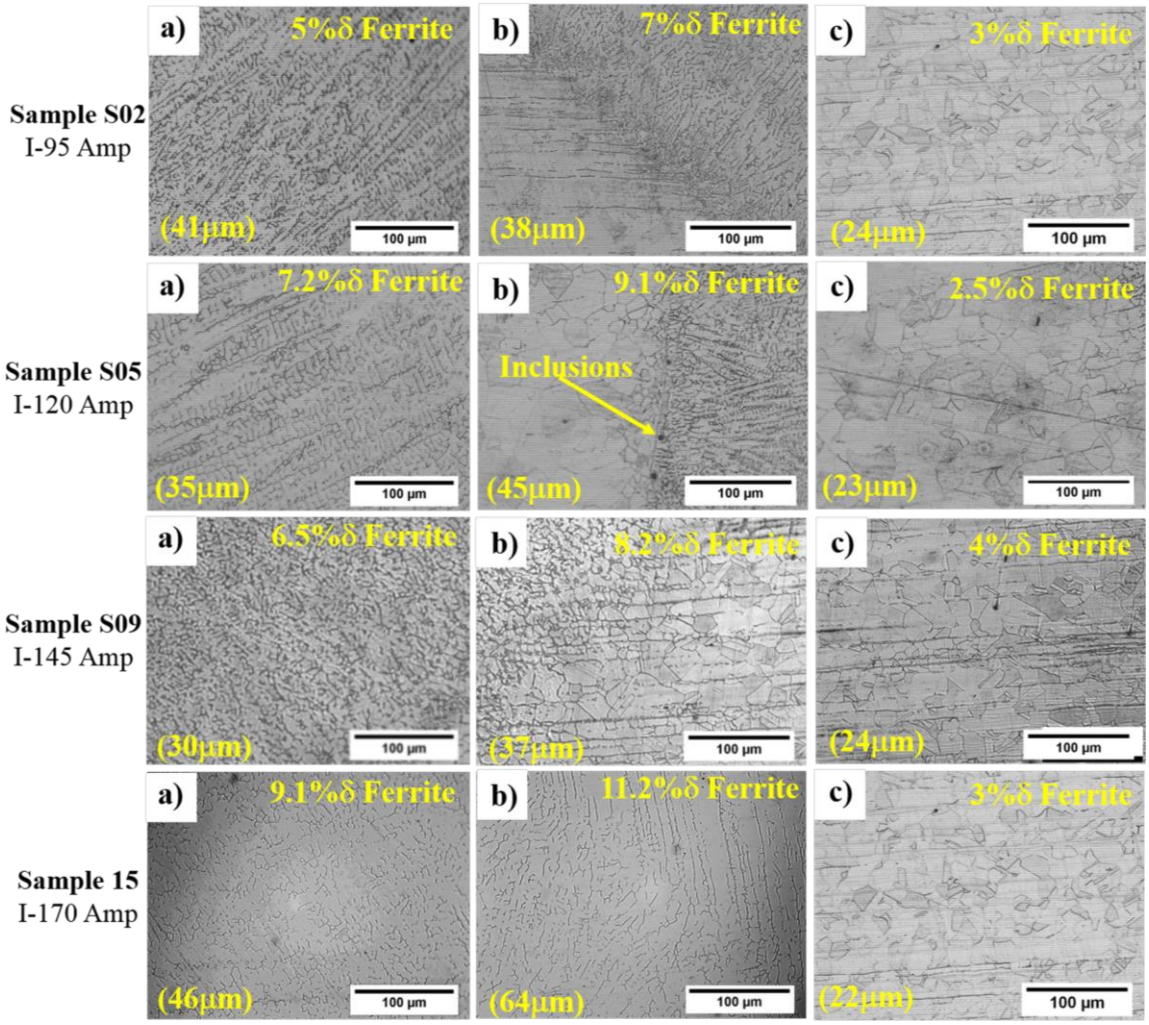

Figure 5.20: Effect of welding speed on microstructure of a) WB, b) HAZ and c) BM

At high current levels, the penetration increased, and a reduction in the dispersed carbides was found due to the availability of sufficient heat for sufficient time. As long time was available, the carbides dispersed in the matrix. From Figure 5.20, the grain size in HAZ also increases with current from 38 µm to 64 µm due to increased heat input, causing grain coarsening effect at higher current levels, and the HAZ width increased too. With an increase in current, removal of large and small inclusions occurred due to increased HI and the UTS and YS increased initially up to 145 A then decreased due to grain coarsening at very high heat inputs. From Figure 5.21, it can be observed that an increase in welding current increased δ-ferrite volume percent increase from 5% to 11% with the increase in current from 95 A to 170 A in weld bead and HAZ. As the heat input increased with current, which promoted the δ ferrite volume percent. At 145 A, slight

decrease in ferrite content in the HAZ area was observed, which may be due to increased electrode melting rate that may have reduced the overall HI.

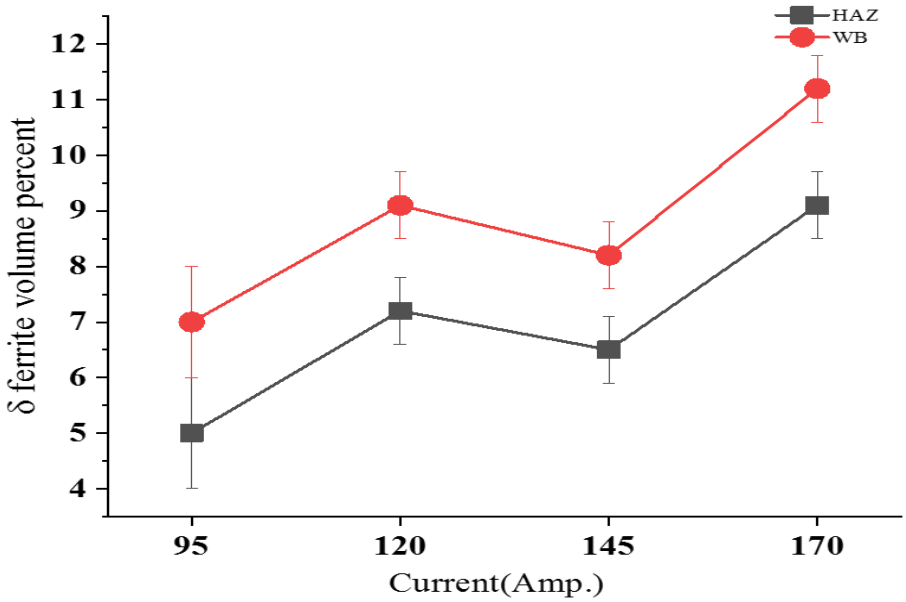

Figure 5.21: Current effect on δ ferrite content for sample S02(95 A), S05(120 A) and S09(145 A), S15(170 A)

The initiation of the solidification firstly starts from the partial melting zone in the interface at the UMZ. It then progresses along the melt line and moves towards the center of the WM. From the micrograph of HAZ in Figure 5.20(b), it can be seen that the use of a lower current leads to the reduction of the width of the UMZ compared with the high current. The difference in the width of the UMZ can be related to the factors of the agitation of the melt pool due to gas flow rate and the convection heat transfer rate. Current is the main contributing factor that controls the heat input and metal deposition rate.

4.9.3 Effect of Shielding Gas flow rate

The effect of shielding gas flow rate on microstructure morphology can be seen in Figure 5.22. Heat input mostly dominated the microstructure and grain morphology. Lesser variation in δ Ferrite was observed due to an increase in gas flow rate. Grain size variation was 42 µm (S09) to 33 µm (S02) as HI increased, and a maximum of 64 µm in

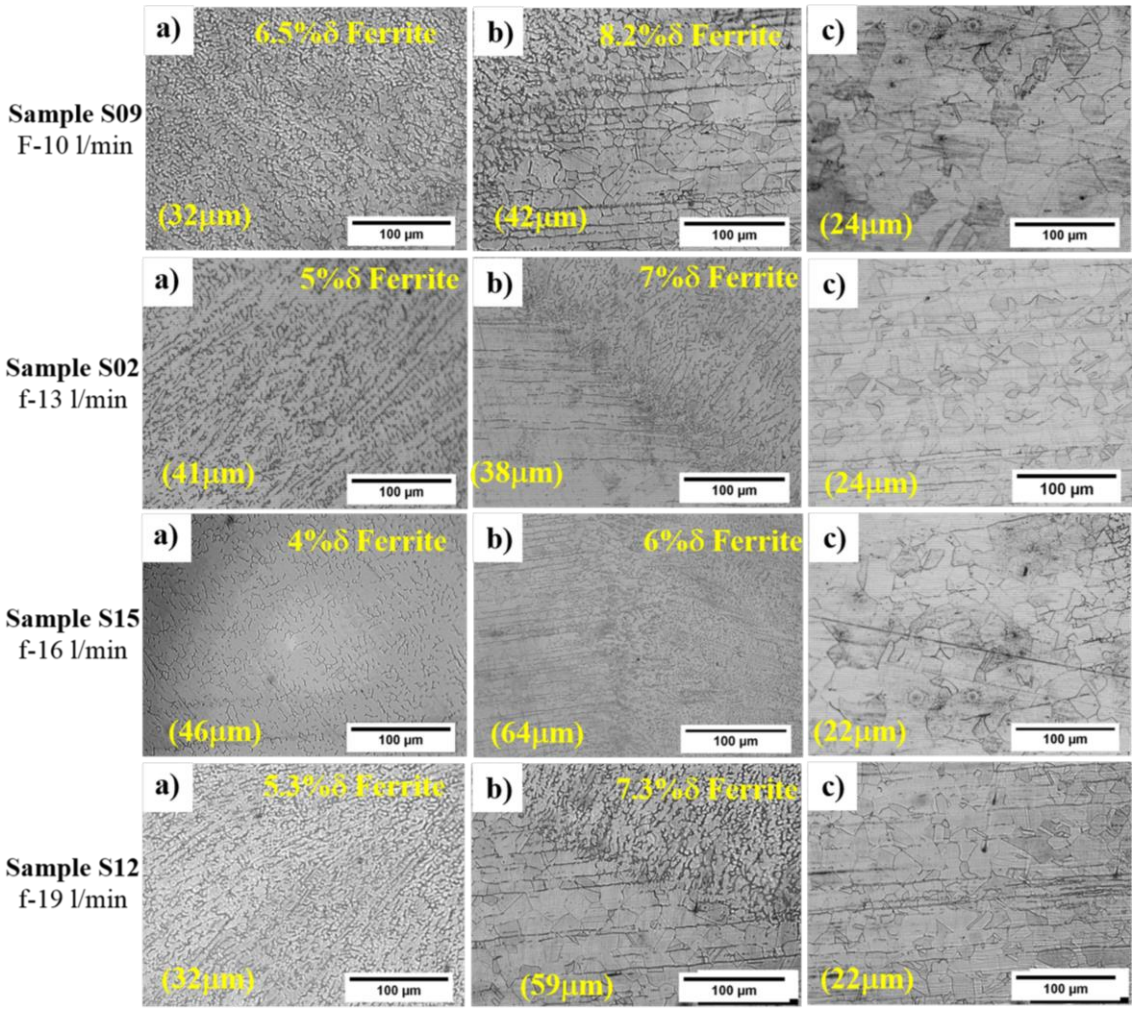

Figure 5.22: Effect of gas flow rate on microstructure of a) WB, b) HAZ and c) BM

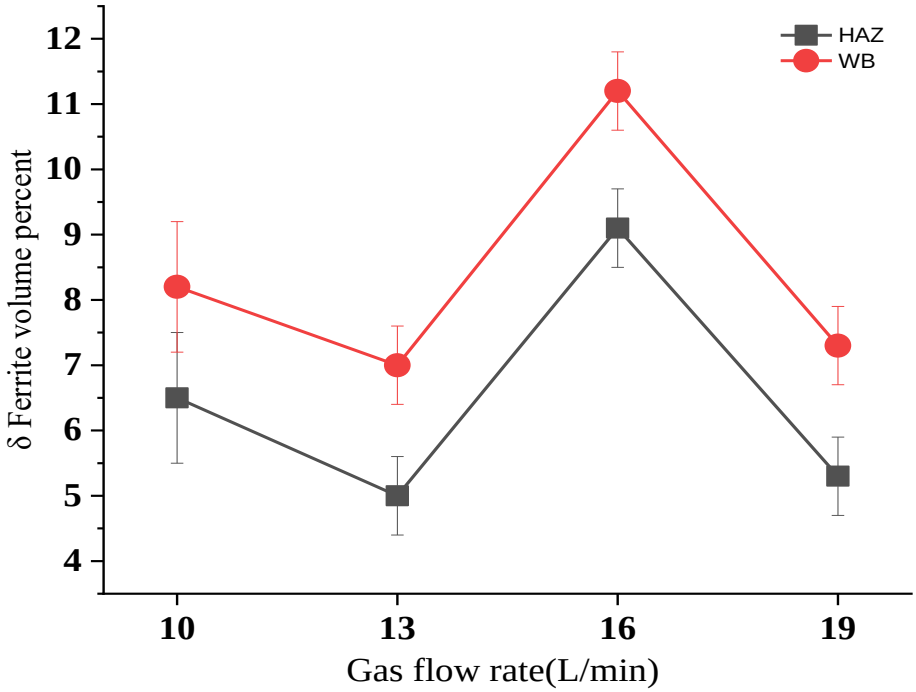

Figure 5.23: Gas flow rate effect on δ ferrite content for sample S09(10 l/min), S02(13 l/min) and S15(16 l/min), S12(19 l/min)

The Level of spatters decreased for a medium level of flow rate (16 l/min), indicating proper shielding of the weld pool. From Figure 5.23, it can be observed that gas flow rate variation has caused more variation in δ-ferrite content, as higher gas flow rate increased the spatter quantity and CO_2 available around the weld.

4.9.4 Effect of welding speed

The effect of welding speed can be visualized in Figure 5.24. From Figure 5.24, it can be observed that an increase in welding speed increases, strengthening precipitates so the strength increased and microstructure changed from the skeletal structure to lathy can be seen in the weld bead.

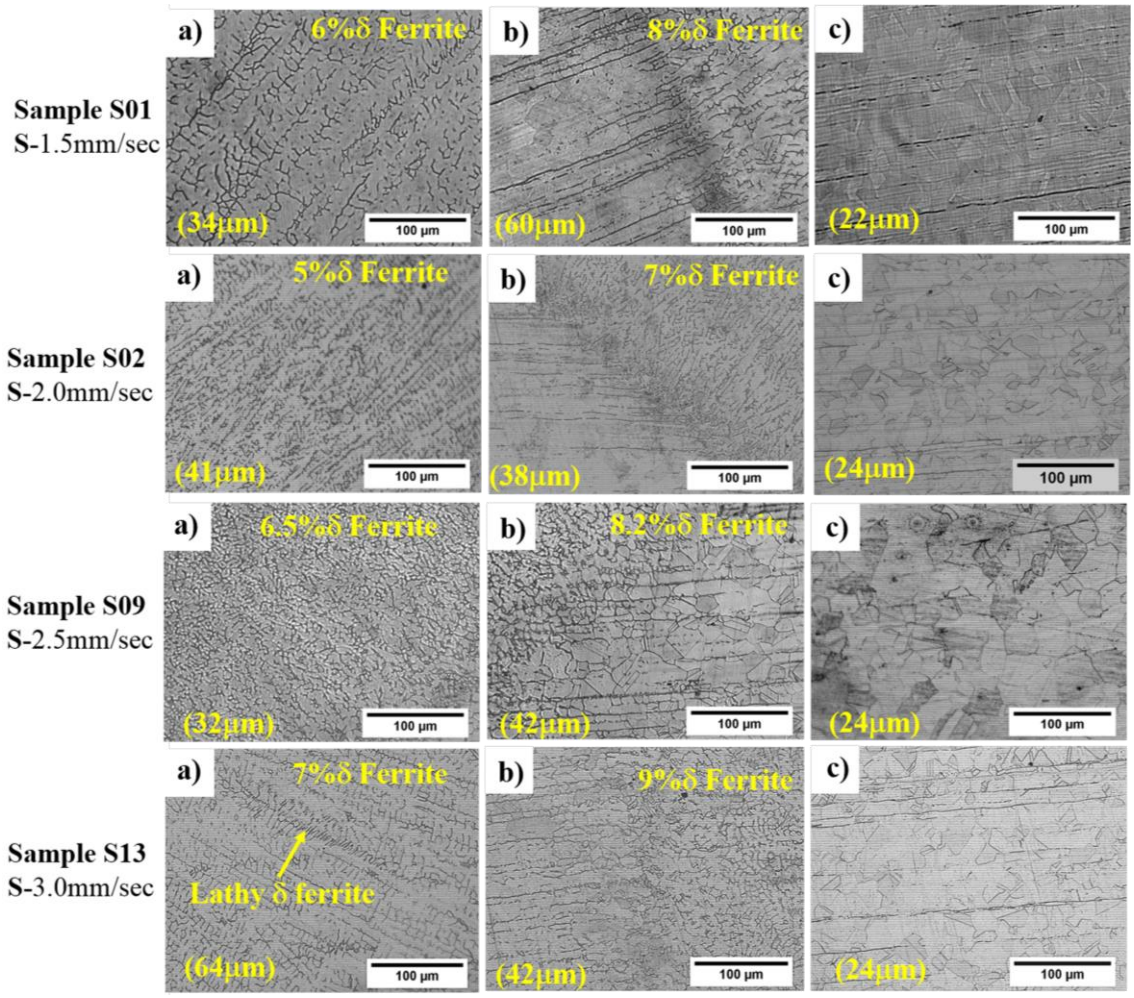

Figure 5.24: Effect of weld speed on microstructure of a) WB, b) HAZ and c) BM

Also, reduction in HI caused a reduction in δ ferrite and grain coarsening in HAZ. Grain size in HAZ also decreases with an increase in weld speed. High welding speed

provided a higher cooling rate, while low welding speed reduced the cooling rate. During the cooling process, the δ-ferrite phase precipitated in the WM and then transformed into the γ-austenite phase. The cooling speed was too fast that only a small portion of δ → γ transformation could be achieved. Some Cr-rich austenite nuclei were preserved and formed into wormlike or skeletal δ-ferrite [197]. Welding speed increase transformed the lathy structure to skeletal, and the grain size initially decreased slightly and then increased and finally reached the 42 µm in HAZ. From Figure 5.25, it can be seen that ferrite volume percent initially decreased and further increased from 5% to 7% following the trend of low heat input(for S02 having HI-5.43 kJ/cm) resulted in lower δ ferrite with respect to high HI(for S01 having HI- 8.51 kJ/cm). So control of HI also controls the morphology of HAZ and weld bead.

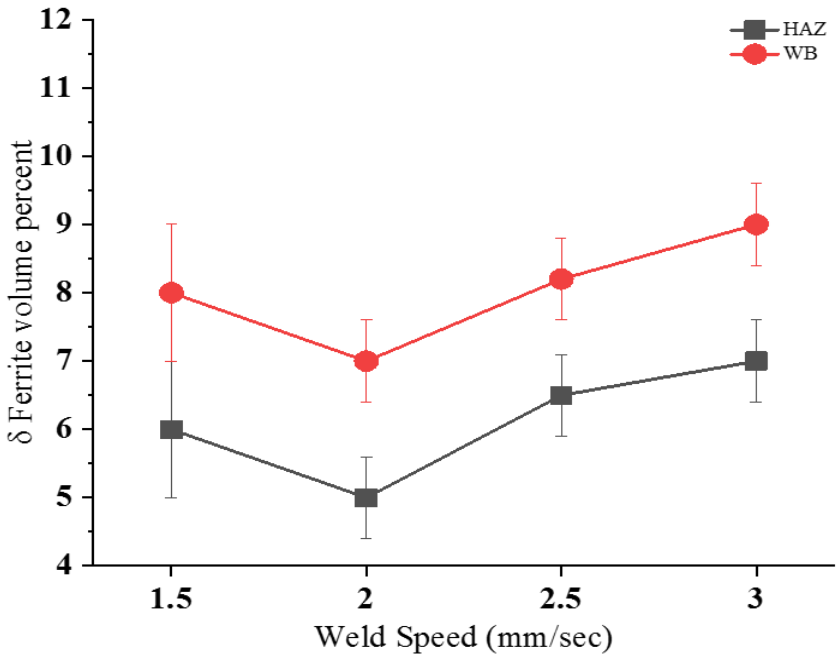

Figure 5.25: Weld Speed effect on δ ferrite content for sample S01(1.5 mm/sec), S02(2 mm/sec) and S9(2.5 mm/sec), S13(3 mm/sec)

4.10 Mechanical Properties of 316L SS Weld joint

4.10.1 Hardness Distribution in HAZ and WB for 316L SS

Average Vickers Hardness in weld bead, unmixed zone, heat-affected zone, and base material for all samples have been tabulated in Table 5.5.

Table 5.5: Average hardness in WB, UMZ, HAZ and BM

Sample No.	Heat Input (kJ/cm)	Hardness (HV)			
		WB	UMZ	HAZ	BM
S01	8.51	207	228	208	179
S02	5.43	209	231	213	174
S03	3.51	211	243	225	179
S04	2.71	221	228	210	174
S05	6.85	211	207	198	178
S06	11.76	209	213	195	179
S07	3.63	221	228	210	179
S08	4.84	214	241	223	180
S09	5.68	216	248	230	184
S10	4.38	221	246	228	177
S11	15.43	216	236	218	179
S12	8.77	219	243	225	179
S13	6.06	221	233	215	181
S14	8.51	219	243	235	178
S15	12.45	210	241	223	179
S16	21.28	211	232	212	179

For all the samples, the microhardness values increase when they reach the fusion zone (FZ), becoming larger when they approach from the center. This is due to the fact that FZ has a greater amount of δ ferrite, which is a phase that has a greater hardness than austenite. A gradual decrease in hardness moving away from the weld centerline was observed. Hardness distribution for sample S08 is shown in Figure 5.26, which shows a gradual decrease in HAZ hardness moving away from the centre line.

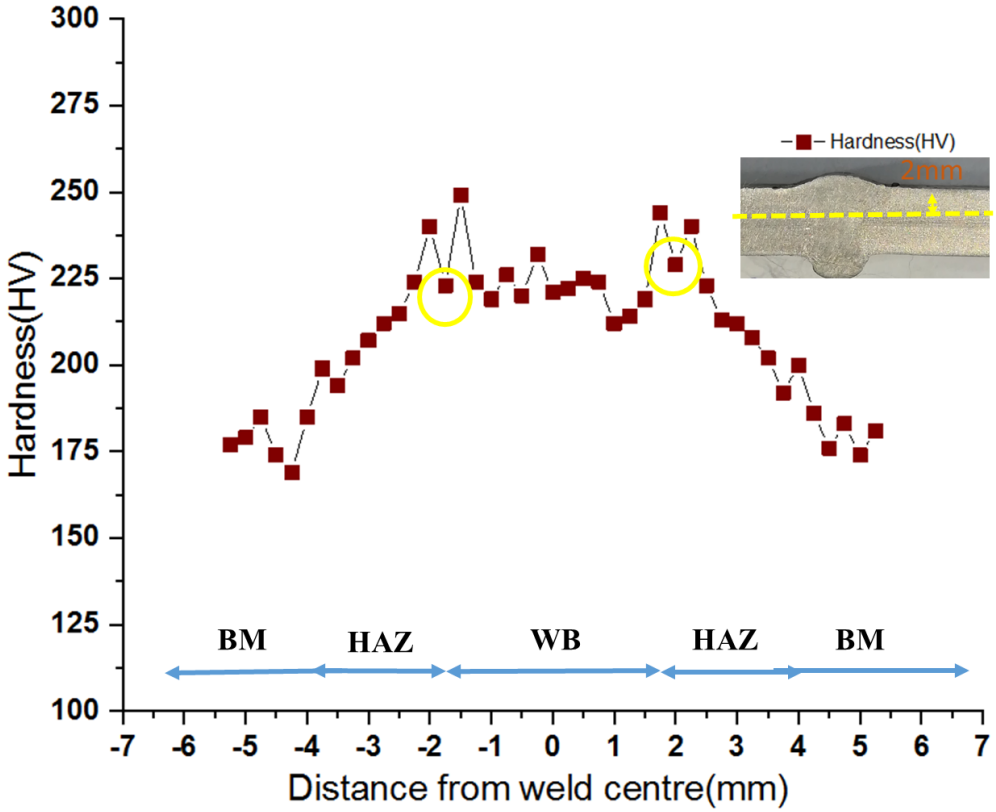

Figure 5.26: Hardness distribution for Sample S08 (I-120 A, f-19 l/min and 2.5 mm/s)

A sudden dip in hardness was also observed in the region of grain growth. It is evident from the hardness graph that there lies a soft zone governed by the cooling rate in WB and HAZ [198]. High HI results in more reduction in hardness. Maximum hardness in the outer part of HAZ was found due to heat transferred from weld pool to base metal, while high HI decreased the volumetric percentage of δ ferrite and hardness levels due to favoured growth of austenite at high temperatures. Grain growth in HAZ has caused a decrease in hardness adjacent to the fusion boundary but not as critical as in high strength low alloy steel. Sample S05 showed minimum variation in hardness with respect to other samples along with good UTS and YS but slightly lower than Sample S09. As Heat input varied from 3.11-25 kJ/cm and Hardness varied from 178-246 HV showing larger variation across the weld for higher HI levels. An increase in heat input has caused a decrease in hardness in HAZ due to the grain coarsening effect in HAZ and attains a maximum value around the grain coarsened zone, i.e. in UMZ and low temperature HAZ.

Hardness shows a gradual decrease in Hardness up to the base material for 316L. Figure 5.27 shows the comparison of hardness profile for different heat input values for S02(5.43 kJ/cm), S05(6.85 kJ/cm), S12(8.77 kJ/cm) and S16(21.28 kJ/cm) samples. It can be seen from the graph that WB hardness is higher for all the samples with a gradual decrease. A sudden dip in hardness can be seen from the hardness profile. Lower to medium HI levels showed higher hardness with narrower HAZ with respect to the S16 sample. High HI enlarged the UMZ and HAZ there, decreasing the hardness and austenite volume percentage.

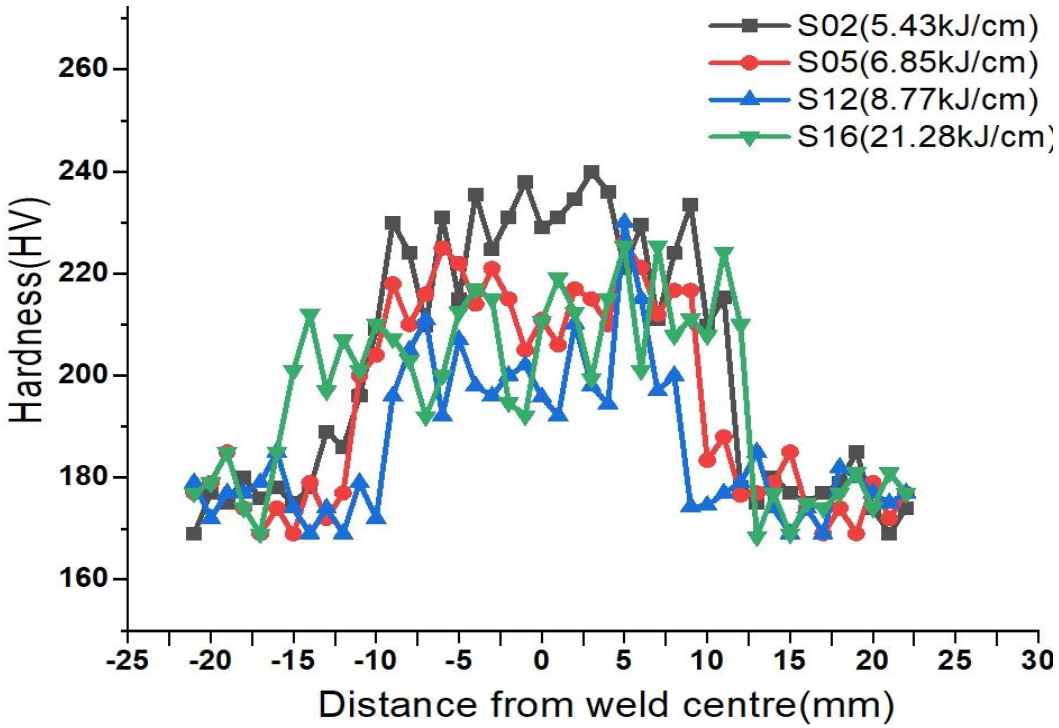

Figure 5.27: Hardness distribution for different HI in S02, S05, S12 and S16

Hardness in UMZ is higher due to fine δ ferrite and martensite in austenite matrix restricting the plastic deformation and increase in hardness values and similar results were found by **Lippold et al.** [195, 199].

An increase in the current level also shows a similar trend as the current increase also increases the HI and removes the harder phases. Grain coarsening too comes into effect more dominantly at higher current levels along with precipitation of hardening

alloys. It is also observable that in the HAZ region, hardness value has reduced gradually due to a rise in temperature and lowering of the cooling rate that results in a reduction in hardness [200]. On the other hand, an increase in weld speed lowers the HI causing a reduction in grain size up to a certain level; hence improvement in hardness according to the famous Hall-Petch relation was observed.

Correlating the bar diagram for HI in Figure 5.9 with the average hardness shown in Table 5.5, it can be seen that the specimen welded with low heat input depicts a higher hardness value, and the specimen welded using high heat input shows the lowest harness value in the weld zone due to lower δ-ferrite content and relatively coarse grain structure. The specimen made using medium heat input was having the highest hardness values due to higher δ-ferrite content and having a relatively finer grain structure.

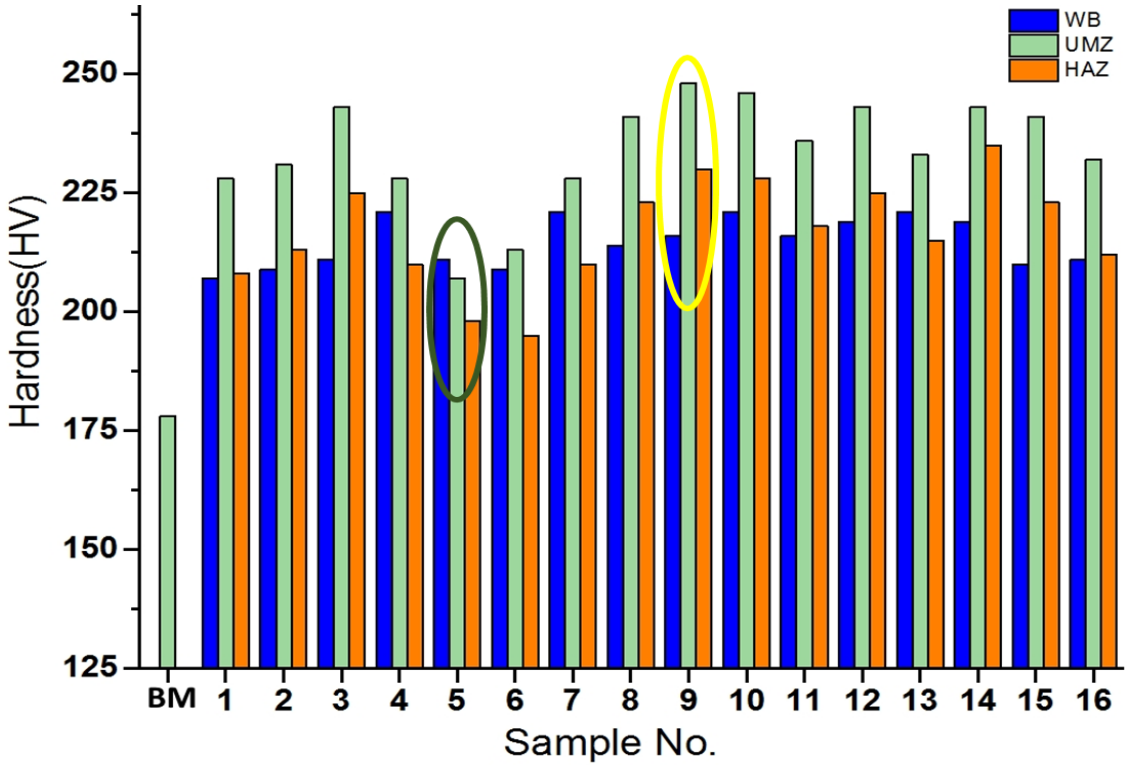

Figure 5.28: Hardness distribution in Weld Bead, UMZ, HAZ and BM

The variation in hardness values in different weld specimens may be induced by their microstructure refinement due to the quick solidification of the weld pool. Hardness in HAZ increased with weld speed and gas flow rate for Sample S01 to S04 and S16 to

S12, as evident from Figure 5.28. It can also be seen that for sample S05 the variation in Hardness zones is lower as compared to other samples, so it might be good as far as hardness variation is concerned and mechanical properties.

4.10.2 Tensile Properties of 316L SS Weld joint

The tensile strength and respective yield strength of all the 16 samples and base material can be seen in Figure 5.29. Through Taguchi's analysis, the sample S09 welded at Current: 145 A, Gas flowrate: 10 l/min at 2.5 mm/sec Weld speed was the optimum parameters for 316L SS having the highest Ultimate tensile strength (UTS) of 535 MPa. Its Yield strength (YS) was 273 MPa. Sample S09 welded at optimum welding parameters was having 6.5% δ ferrite with skeletal morphology in WB and lower level of grain coarsening in HAZ having a grain size of 32 µm and 42 µm, respectively.

Figure 5.9 shows the relationship between sample number and HI suggests that from S01 to S04, HI decreased continuously along with an increase in gas flow rate, while from Sample S13 to S16, HI decreased continuously. So the effect of parameters can be analyzed through these samples as well. The relationship between HI and other parameters can be analyzed through the interaction plots as shown in Figure 5.6 to Figure 5.8 for 316L SS. The increase in dilution and removal of impurities at higher HI may have increased the UTS with current from 120 A to 170 A, followed by a decrease at higher HI pertaining grain growth in HAZ. For lower levels of current (95 A), less availability of much-needed heat caused UTS decrease and lack of fusion and low penetration. For a higher level of current 120 A to 170 A, an Increase in weld speed increased the UTS, followed by a decrease as weld speed reduced heat availability for weld pool and HAZ, resulting lower grain coarsening effect. Most of the samples fracture from weld bead (for low HI levels S02 and S04) and HAZ area showing good weldability characteristics and ductile mode of fracture was observed to be discussed later.

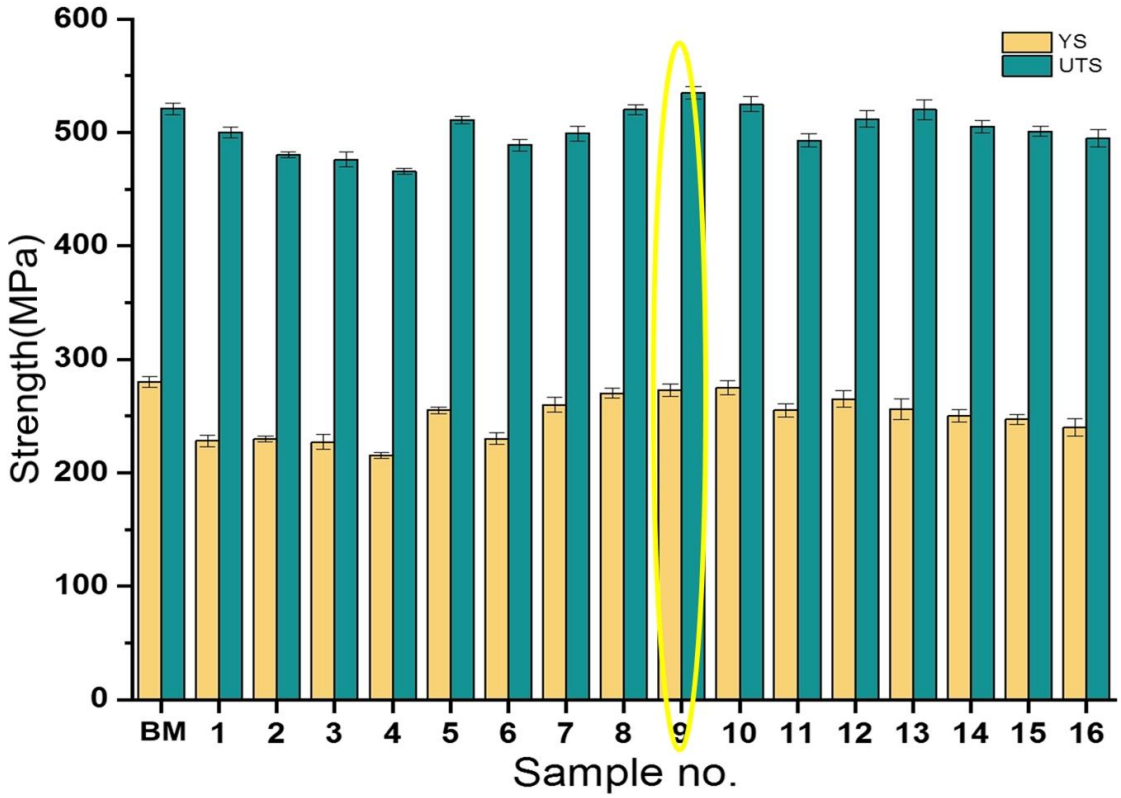

Figure 5.29: Effect of Heat Input on UTS and TS Vs Sample no.

From the bar charts in Figure 5.29, it can be seen that Mean UTS and YS both gradually increased as HI increased with current, causing an increase in penetration. The removal of inclusion and increase of δ-ferrite in HAZ up to a current level of 145 A with maximum UTS and YS of 535 MPa and 273 MPa, respectively. For sample S09 as full penetration joint without carbide inclusion and lesser grain coarsening in HAZ pushed the UTS to the highest level. So UTS levels found at 145 A current were 535 MPa (S09), 525 MPa (S10), 493 MPa (S11) and 512 MPa (S12). Grains size in HAZ were also low as 37 µm for the sample S09. A decrease in UTS and YS was found at 170 A current levels and higher HI, causing diffusion of carbon in the austenite matrix. A similar trend in the yield strength was obtained with respect to UTS, but more variation in YS was observed from the line diagram shown in Figure 5.30.

For current of 95 A level increase in gas flowrate decrease in UTS was observed with UTS as 500 MPa (S01) at 10 l/min, 480 MPa (S02) at 13 l/min, 476 MPa (S03) at

16 l/min and 466 MPa (S04) was found due to increased volume percentage of CO_2 available for weld pool increase also higher gas flow rate increased turbulence in the weld pool. For the current level of 145 A increase in gas flow rate followed a similar trend of decrease. Conclusive results cannot be obtained for yield strength as from the interaction plot Figure 5.7 showed a high level of dependency on other parameters. Increased level of gas flowrate from 13 l/min to 19 l/min also increased the chances of carbon pickup in the weld pool, thereby increasing inclusion levels and decreased UTS and YS. From the microstructure, not much variation in HAZ grain size was observed, but delta ferrite volume percent increased for higher heat input and higher gas flowrate.

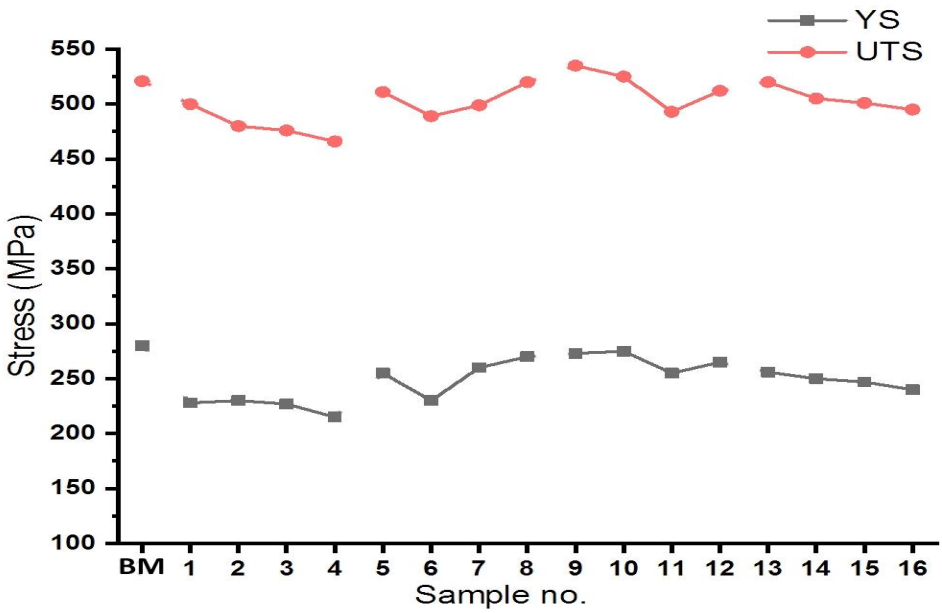

Figure 5.30: UTS and YS variation for each sample number

Welding speed behaves inversely with respect to an increase in the current level. An increase in weld speed decreases the total heat input, causing a decrease in δ ferrite volume fraction, restricting the diffusion of carbon in the austenite matrix, making carbon available for carbide formation in as harder phases. An increasing trend in UTS up to 2.5 mm/sec was observed, followed by a decrease as 3-6% δ ferrite is required to avoid hot cracking in 316L stainless steels. A decreasing trend in UTS and Heat Input with an increase of weld speed was found due to a higher volume of ferrite. For the lowest weld

speed of 1.5 mm/sec, UTS levels found were 500 MPa, 489 MPa, 493 MPa and 495 MPa for samples S01, S06, S11 and S16, respectively, while for 2.5mm/sec weld speed for current level 145 A UTS were 476 MPa, 520 MPa, 512 MPa and 505 MPa for sample S03, S08, S09 and S12 respectively. Further increase in Weld speed decreased the UTS levels. A similar trend was followed by YS for an increase in weld speed caused decrement in HI, which decreased the grain size in HAZ, and according to the Hall-patch equation, YS decreases with an increase in Grain Size due to increased HI. It was also found that the δ-ferrite content fluctuated with the welding speed variation. Lathy δ-ferrite and skeletal δ-ferrite and precipitates were simultaneously observed, depending upon the heat input in the welding [201]. The Cr and Ni elements could concentrate or migrate at the grain boundaries of the austenite matrix in 316L SS due to rapid cooling or insufficient heat in welding, decreasing the UTS. This would lead to a variation in the local Cr/Ni ratio. As shown in Figure 5.12, at the same peak temperature, the phase diagram enters the δ + γ area with the ratio of Cr/Ni increasing; therefore, δ-ferrite is formed again. This may result in a variation in the content of δ-ferrite and a change in morphology due to HI. With an increase in the grain size and the δ-ferrite content, the tensile strength decreased. δ ferrite content increased with HI and varied from 5% (for S02) to 11.2% (for S15) at 12.5 kJ/cm and affected UTS more significantly. The austenitic grain size affected the YS largely under experimented conditions; similar results were found by **Demarque et al.** [71], indicating an increase in δ ferrite with increased heat input levels for 316L SS bead on plate weld.

The effect of gas flow rate can be analyzed through sample S01 to S04, which increased from S01 to S04. From the interaction plots in Figures 5.6 and 5.7, it can be seen that UTS showed downward variation for the highest gas flow rate (19 l/min) caused due to excessive turbulence at higher gas flow rates. As any monotonous trend was not

seen so conclusive results cannot be deduced but 10 l/min gas flow rate at 2.5 mm/sec weld speed showed maximum strength of 535 MPa (UTS) and 273 MPa (YS).

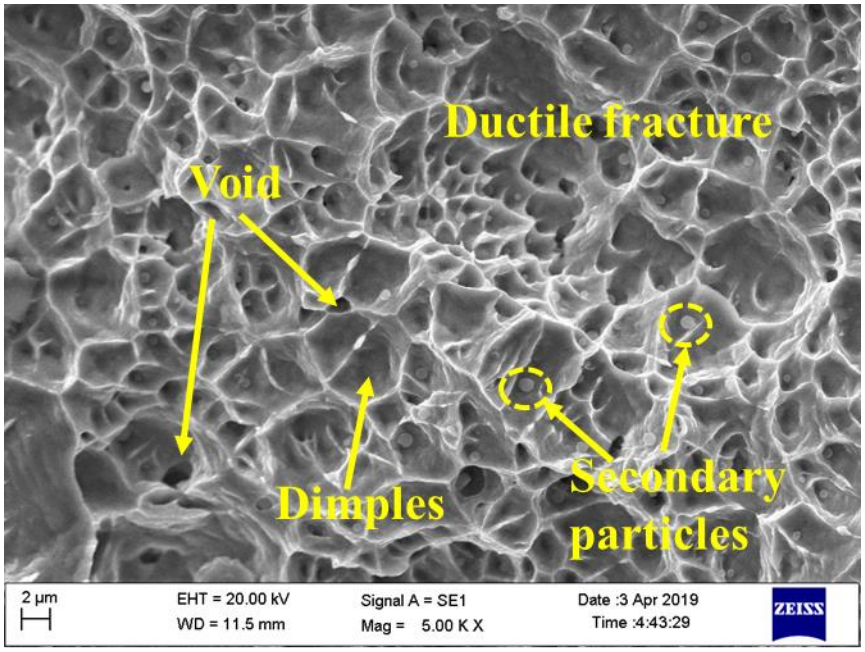

Figure 5.31: SEM image of a fractured tensile specimen of 316L SS base material

Fractography of base material showed the ductile mode of fracture characterized by bright plastic flow lines around the dimples along with micro-voids and circular secondary particles, as shown in Figure 5.31. As mentioned during the microstructure section, increasing HI and current levels led to microstructural changes in the HAZ and shown from the fractography of tensile samples. Most of the tensile samples fractured from the transition zone or HAZ. The SEM micrographs of fractured surfaces during tensile test are presented in Figure 5.32. In all samples, a cellular region was found characteristic of the fracture surface with many equiaxed dimples of varying size and shape along with voids and micro-voids. Visible surface cracks were also not observed, indicating a ductile mode of fracture. Solidification voids can be observed from the surface along with void-dominated fractures. For all the fractured samples mode of failure was ductile in nature, having dimples in variable sizes.

Figure 5.32 shows the fractograph depicting the effect of current on fracture mode of tensile specimens. Various features in SEM images of tensile fractography for variable current can also be seen. It was observed that the specimens welded at 145 A current level showed deep dimples and higher strengths.

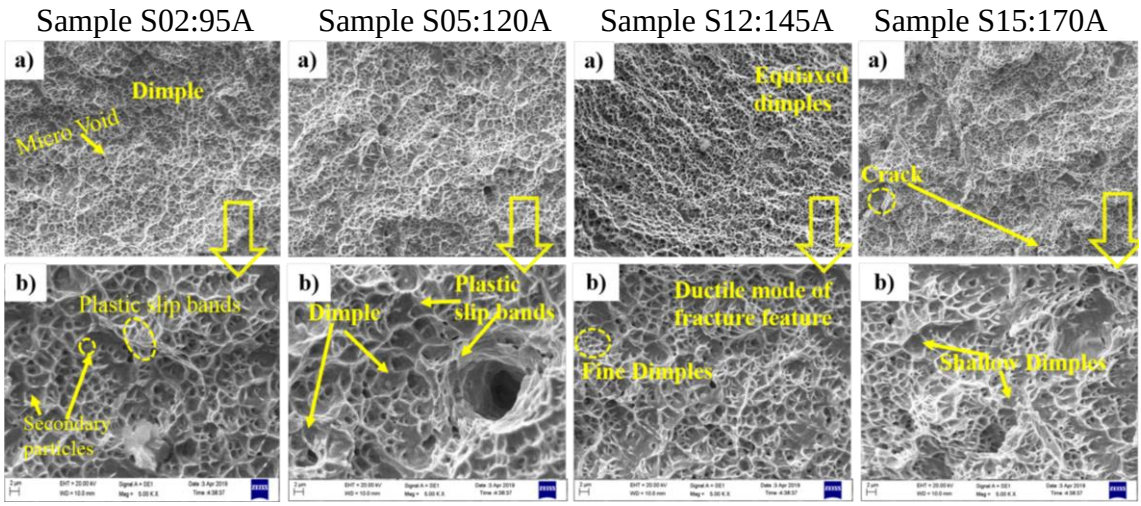

Figure 5.32: Effect of current on SEM micrograph of fractured tensile specimen

Sample S09 and S12 contains uniformly distributed deep and fine dimples without any micro-cracks, as shown in Figure 5.32. The presence of fine along with coarse dimples indicates the heterogeneous nature of HAZ microstructure. Fine deep dimples indicate the high resistance offered by the weld joint before fracture. It is noticed from SEM images that sample S02 (low HI-5.43 kJ/cm) consist of fine dimples and voids. In the case of sample S12 (medium HI- 8.77 kJ/cm), a large number of very fine and deep dimples are observed, and surface cracks are also invisible. This is in line with the DOE results and the reason for its highest tensile strength. An increase in the δ-ferrite content leads to an increase in strength. In the case of sample S15 (HI- 12.45 kJ/cm), large and shallow dimples were observed, along with a few crack boundaries. Similar patterns were observed for variation in weld speed depending upon the heat input levels. No considerable change in fractographic images were found for variation in gas flow rate.

Summary

The experimentation and analysis were carried out using DOE, and the results were successfully verified through the macrostructure, microstructural features, and mechanical behaviour for maximum strength. Heat affected zone of joints were also analyzed for their contribution. The characteristics of the fusion zone are typical coarse columnar grains structure because of the prevailing thermal conditions during weld metal solidification. Heat affected zone contained the soft zone, which is the result of grain coarsening effect for higher heat input parameters, particularly in CGHAZ, resulting in the reduction of strength levels. For welded joints at different current, gas flow rate and weld speed values, optimum parameters for both welded materials were found by Taguchi analysis and were verified. Current levels was the most dominating parameter, followed by weld speed and gas flow rate affecting the strength properties and contributed to major microstructural changes. It was found that the hardness of the CGHAZ zone was degraded significantly due to the lower cooling rate during the welding process favouring grain growth in heat affected zone.

The next section will summarize the results obtained for both A572 gr. 50 and 316L SS joints and the findings of the present investigation, together with concluding remarks and scope for future work.